

Modeling of Wheel-Soil Interaction for Small Ground Vehicles Operating on Granular Soil

by

William Clarke Smith

A dissertation submitted in partial fulfillment
of the requirements for the degree of
Doctor of Philosophy
(Mechanical Engineering)
in The University of Michigan
2014

Doctoral Committee:

Professor Huei Peng, Chair
Matthew P. Castanier, US Army TARDEC
Professor Roman D. Hryciw
Professor Noel C. Perkins
Sally A. Shoop, US Army CRREL

© William Clarke Smith

2014

ACKNOWLEDGEMENTS

I would like to express my gratitude to my advisor Professor Huei Peng. His guidance helped me transition from an undergraduate student into an independent researcher. I am grateful for his light touch which helped me to identify and develop a research direction.

The research freedom I enjoyed would not have been possible without the Science, Mathematics & Research for Transformation (SMART) Scholarship I received from the Department of Defense. Without the support of the scholarship, I may not have been able to take the time necessary to follow my interests and investigate the discrete element method.

The summer internships spent at my SMART Scholarship sponsoring facility, the US Army Tank Automotive Research, Development, and Engineering Center (TARDEC) were also crucial to my success. In particular, I would like to thank Dr. Matt Castanier, Andrew Dunn, Dr. Jeremy Mange, Daniel Melanz, Dr. Jayakumar Paramsothy, Mike Pozolo, and Denise Rizzo for their support and encouragement.

I am also grateful to my labmates, especially Dr. Changsun Ahn, Tian-You Guo, Byung-Joo Kim, Dr. Youngki Kim, Dr. Chiao-Ting Li, Ziheng Pan, Xiaowu Zhang, and Ding Zhao. I am grateful for their help and assistance with research, and for their friendship.

I would like to thank my family for inspiring me to pursue a Ph.D. and for their encouragement through the process. My deepest thanks go to my wife, who took a chance when coming to Michigan and has been by my side ever since.

TABLE OF CONTENTS

ACKNOWLEDGEMENTS	ii
LIST OF FIGURES	vi
LIST OF TABLES	x
LIST OF APPENDICES	xi
ABSTRACT	xii
CHAPTER 1 Introduction.....	1
1.1 Motivation.....	1
1.2 Background.....	3
1.2.1 Terramechanics Modeling	3
1.2.2 Rough Surface Locomotion	8
1.3 Research Objective and Scope.....	9
1.4 Contributions.....	11
1.5 Outline of the Dissertation	13
CHAPTER 2 Fast Computation Semi-Empirical Terramechanics Models.....	14
2.1 Bekker Modeling Review	14
2.2 Bekker Method Computation Limitations	20
2.3 Lookup Table Method.....	20
2.4 Quadratic Approximation Method.....	25
2.4.1 Modeling of Lugged Wheels	26
2.4.2 Quadratic Stress Approximation.....	28
2.4.3 Performance Evaluation and Comparison	29
2.5 Conclusions.....	33
CHAPTER 3 Surface Roughness Modeling	34
3.1 Discrete Element Method	34
3.2 Simulation Preparation.....	37
3.2.1 Soil Packing	38
3.2.2 Wheel Building	40
3.3 DEM Validation.....	42

3.3.1 Smooth Soil Validation.....	43
3.3.2 Wheel-Digging Validation.....	45
3.3.3 Conclusions.....	47
3.4 Rough Terrain Simulations	47
3.4.1 Sinkage.....	50
3.4.2 Drawbar Pull	51
3.4.3 Driving Torque.....	52
3.5 Conclusions.....	54
CHAPTER 4 DEM Tuning and Evaluation.....	55
4.1 Terramechanics Methods	55
4.1.1 Bekker Method.....	55
4.1.2 Dynamic Bekker Method.....	56
4.1.3 Discrete Element Method	57
4.2 Soil Testing	61
4.2.1 Experimental Tests.....	62
4.2.2 Bekker Parameter Identification	62
4.2.3 Discrete Element Method Tests	64
4.2.3.1 Direct Shear Test.....	66
4.2.3.2 Pressure-Sinkage Test.....	68
4.3 Wheel Testing	70
4.3.1 Experimental Tests.....	70
4.3.2 Simulation Settings	72
4.3.2.1 Bekker Method.....	72
4.3.2.2 Dynamic Bekker Method.....	72
4.3.2.3 Discrete Element Method	74
4.3.3 Simulation Results	75
4.3.4 Bekker Tuned using DEM	78
4.4 Conclusions.....	80
CHAPTER 5 Surrogate DEM.....	82
5.1 Literature and Inspiration.....	83
5.2 Surrogate DEM Overview	84
5.2.1 Constant-Velocity Motion Simulations	86
5.2.2 Soil Velocity Table Creation	89
5.2.3 Wheel Force Table Creation	93

5.2.4 Table Implementation	96
5.3 Simulation Specifications	99
5.3.1 DEM.....	99
5.3.2 S-DEM	100
5.4 S-DEM Validation	100
5.4.1 Smooth Soil Validation.....	101
5.4.2 Rough Terrain Validation	105
5.5 Conclusions.....	109
5.6 Future Work	111
CHAPTER 6 Conclusions and Future Work	112
6.1 Conclusions.....	112
6.2 Future Work	113
APPENDICES	115
BIBLIOGRAPHY	121

LIST OF FIGURES

Figure 2.1 Wheel-soil contact geometry (cylindrical surface, positive wheel slip) [81]..	15
Figure 2.2 Bevameter schematic [8] (originally printed in [10]).....	16
Figure 2.3 Normal and shear stress distributions along the wheel-soil interface [81].....	16
Figure 2.4 Shear stress as a function of shear displacement for three soil types.....	18
Figure 2.5 Distribution of normal and shear stresses along the wheel-soil contact area [81].....	20
Figure 2.6 Response to repetitive normal load on a mineral terrain [8]	21
Figure 2.7 Flow chart for building wheel lookup tables [87]	22
Figure 2.8 Example wheel lookup tables: entry contact angle [87].....	23
Figure 2.9 Example wheel lookup tables: thrust force [87].....	24
Figure 2.10 Example wheel lookup tables: resistance force [87]	24
Figure 2.11 Example wheel lookup table: unloading sinkage [87]	24
Figure 2.12 ORRDT screenshot performing vehicle design and velocity optimization [87]	25
Figure 2.13 Stresses for a lugged wheel traveling on sandy loam, calculated using the original non-linear model, linear approximations, and quadratic approximations [77] ...	26
Figure 2.14 Wheel with lugs on soft soil [77]	27
Figure 2.15 Approximation errors at varying slip angles and slip ratios for a smooth wheel on sandy loam soil [77]	31
Figure 2.16 Approximation errors for smooth (S) and lugged (L) wheels using linear (1) and quadratic (2) approximation methods [77].....	32
Figure 3.1 DEM contact model for particle-particle force/torque interactions [99] (after [100]).....	36
Figure 3.2 Example soil block after packing	38
Figure 3.3 Wheel types used in simulation: (a) Ding, (b) MER [99]	41
Figure 3.4 Smooth soil simulation at 0.275 slip (soil color shading indicates elevation) [99]	43
Figure 3.5 Time series drawbar pull, sinkage, and driving torque data for smooth soil validation at two slip values (-0.025, 0.375) [99]	44

Figure 3.6 Average drawbar pull, sinkage, and driving torque values from smooth soil simulation and experiment [99] (experimental values from [88])	45
Figure 3.7 Wheel digging DEM simulation shown at initialization (a) and after 10.5 seconds (b and c) where soil color indicates elevation [99]	46
Figure 3.8 Time series torque and sinkage data from wheel digging simulation and experiment [99] (experimental values from [103]).....	47
Figure 3.9 Rough soil simulation with amplitude 13 mm, frequency 48 cycles/m, and 0.3 slip (soil color shading indicates elevation) [99]	48
Figure 3.10 Time series drawbar pull, sinkage, and driving torque data for rough terrain with frequency 32 cycles/m and 0.05 slip [99].....	49
Figure 3.11 Low frequency (16 cycles/m) rough soil compaction with varying terrain amplitudes (6.5, 13, 19.5 mm) [99]	50
Figure 3.12 High frequency (64 cycles/m) rough soil compaction with varying terrain amplitudes (6.5, 13, 19.5 mm) [99]	50
Figure 3.13 Drawbar pull values as a function of surface frequency and amplitude. (a) shows the impact of surface profile on the distribution of drawbar pull values. (b) shows the percent difference between rough and flat drawbar pull average values, where values for flat terrain equaled -11.02, 8.56, 20.84 for slip ratios 0.05, 0.30, 0.55, respectively [99].....	52
Figure 3.14 Driving torque values as a function of surface frequency and amplitude. (a) shows the impact of surface profile on the distribution of driving torque values. (b) shows the percent difference between rough and flat driving torque average values, where values for flat terrain equaled -1.17, 3.45, 5.17 for slip ratios 0.05, 0.30, 0.55, respectively [99].....	53
Figure 4.1 Diagram of the dynamic Bekker model. The close-up region A shows how the wheel contacts the soil nodes. [106]	57
Figure 4.2 DEM contact model for particle-particle force/torque interactions (after [100]) [106].....	58
Figure 4.3 Bekker parameter fit for direct shear and pressure-sinkage tests. [106]	63
Figure 4.4 DEM simulation of direct-shear test at normal load 17830 Pa (soil shading indicates radius). [106].....	67
Figure 4.5 DEM direct shear average results with standard deviation bars. [106].....	67
Figure 4.6 DEM simulation of pressure-sinkage test (soil shading indicates radius). [106]	69
Figure 4.7 DEM pressure sinkage average results with standard deviation bars. [106] ...	69
Figure 4.8 Diagram of MIT wheel test bed. [106]	71
Figure 4.9 Dynamic Bekker convergence analysis for simulation time step. Simulation time is the cpu time per one second of simulation. [106]	73
Figure 4.10 Dynamic Bekker convergence analysis for number of nodes (node spacing). Simulation time is the cpu time per one second of simulation. [106].....	73

Figure 4.11 A rendering of the dynamic Bekker model. [106].....	74
Figure 4.12 DEM wheel simulation at 50% slip (soil shading indicates elevation). [106]	75
Figure 4.13 Simulated drawbar pull at steady-state compared to experimental sinkage, with experimental standard deviation bars. [106]	76
Figure 4.14 Simulated driving torque and sinkage at steady-state compared to experimental sinkage, with experimental standard deviation bars. [106].....	76
Figure 4.15 Drawbar pull and driving torque time series comparisons of experiment and dynamic terramechanics models. Time shown is a 4 second window randomly selected during steady-state operation. [106]	78
Figure 4.16 Bekker fit of DEM drawbar pull. [106].....	79
Figure 4.17 Bekker fit of DEM driving torque and sinkage. [106]	80
Figure 5.1 Outline of the Surrogate DEM procedure. (a) constant-velocity motion DEM simulations used to build the S-DEM tables. (b) post-processing the DEM simulations to build the wheel and soil tables. (c) implementation of the tables to run a S-DEM simulation. (d) DEM locomotion simulation used to for validation.....	85
Figure 5.2 Initial wheel positioning for the constant-velocity motion DEM simulations. Initial positions for simulations with positive and negative vertical velocity are shown.	86
Figure 5.3 Illustration of a constant-velocity motion DEM simulation. The camera angle highlights the quasi-2d nature of the simulation.....	88
Figure 5.4 Example constant-velocity simulations with negative (top) and positive (bottom) wheel vertical velocity.....	89
Figure 5.5 Outline of velocity mapping method. (a) constant-velocity motion DEM simulation. (b) output from DEM consists of time-averaged particle states. Particles are colored based on velocity magnitude. (c) conversion from particles to grids. (d) table velocity values (S_{Vx} , S_{Vz}) are created by determining the input values ($W\omega$, W_{Vx} , W_{Vz} , Δx , Δz , <i>profile</i>) for each table dimension.....	90
Figure 5.6 Sectioning of the soil table into regions to account for the discontinuity created by the wheel.....	92
Figure 5.7 Outline of force mapping method. (a) constant-velocity motion DEM simulation. (b) output from DEM consists of time-averaged particle states. Particles are colored based on wheel-soil force magnitude. (c) conversion from particle force values to angle-based grid pressure values. (d) table force values (S_{Fx} , S_{Fz}) are created by determining the input values ($W\omega$, W_{Vx} , W_{Vz} , θ , <i>profile or height</i>) for each table dimension.....	94
Figure 5.8 Screenshot of S-DEM with implementation details. (a) S-DEM simulation of wheel locomotion. (b) magnification shows inputs to wheel force and soil velocity tables.....	97
Figure 5.9 Flowchart of S-DEM computation procedure.....	98
Figure 5.10 Time series plots of flat terrain wheel performance at -50% and 50% slip ratio.....	103

Figure 5.11 Mean and standard deviation results for flat terrain simulations.	104
Figure 5.12 Time series plots of rough terrain wheel performance at -50% and 50% slip ratio.	106
Figure 5.13 Illustration of sinkage and soil dynamics errors for S-DEM.....	107
Figure 5.14 Simulation screenshots of rough terrain wheel locomotion for DEM (above) and S-DEM (below).	107
Figure 5.15 Mean and standard deviation results for rough terrain simulations.	108

LIST OF TABLES

Table 2.1 Soil parameter values for loose air-dried sand [8].....	23
Table 2.2 Soil parameter values for select soils [37]	29
Table 2.3 Parameters for smooth wheel S and lugged wheel L.....	30
Table 2.4 Additional parameters used for linear/quadratic comparison	30
Table 3.1 DEM simulation and reference soil properties [99].....	39
Table 3.2 DEM particle parameters [99]	40
Table 3.3 Wheel properties [99]	41
Table 3.4 Smooth soil simulation settings [99]	44
Table 3.5 Wheel-digging simulation settings [99].....	46
Table 3.6 Rough profile simulation settings [99]	49
Table 4.1 Bekker parameter values from direct-shear and pressure-sinkage curve fitting.	64
Table 4.2 DEM soil parameters and simulation settings.	65
Table 4.3 DEM direct shear test settings and parameters.....	66
Table 4.4 DEM pressure-sinkage test settings and parameters.....	68
Table 4.5 Experimental wheel test properties.....	71
Table 4.6 Additional Bekker parameter values used for wheel simulations.....	72
Table 4.7 DEM wheel test settings and parameters.....	75
Table 4.8 Bekker parameter values determined by fitting to DEM results.	79
Table 5.1 Constant-velocity DEM simulation settings	87
Table 5.2 Relative position boundaries of the four soil table regions	92
Table 5.3 DEM soil parameters	100
Table 5.4 Validation simulation parameters	101
Table 5.5 Steady-state computation times	105
Table 5.6 Steady-state computation comparison	105
Table 5.7 Rough terrain computation times.....	109
Table 5.8 Rough terrain computation comparison.....	109

LIST OF APPENDICES

APPENDIX A Bekker Method Notation.....	116
APPENDIX B Discrete Element Method Notation	119

ABSTRACT

Modeling of Wheel-Soil Interaction for Small Ground Vehicles Operating on Granular
Soil
by
William Smith

Chair: Huei Peng

Unmanned ground vehicles continue to increase in importance for many industries, from planetary exploration to military defense. These vehicles require significantly fewer resources compared to manned vehicles while reducing risks to human life. Terramechanics can aid in the design and operation of small vehicles to help ensure they do not become immobilized due to limited traction or energy depletion. In this dissertation methods to improve terramechanics modeling for vehicle design and control of small unmanned ground vehicles (SUGVs) on granular soil are studied. Various techniques are developed to improve the computational speed and modeling capability for two terramechanics methods. In addition, a new terramechanics method is developed that incorporates both computational efficiency and modeling capability.

First, two techniques for improving the computation performance of the semi-empirical Bekker terramechanics method are developed. The first technique stores Bekker calculations offline in lookup tables. The second technique approximates the stress distributions along the wheel-soil interface. These techniques drastically improve computation speed but do not address its empirical nature or assumption of steady-state operation.

Next, the discrete element method (DEM) is modified and tuned to match soil test data, evaluated against the Bekker method, and used to determine the influence of rough terrain on SUGV performance. A velocity-dependent rolling resistance term is developed

that reduced DEM simulation error for soil tests. DEM simulation shows that surface roughness can potentially have a significant impact on SUGV performance. DEM has many advantages compared to the Bekker method, including better locomotion prediction, however large computation costs limit its applicability for design and control.

Finally, a surrogate DEM model (S-DEM) is developed to maintain the simulation accuracy and capabilities of DEM with reduced computation costs. This marks one of the first surrogate models developed for DEM, and the first known model developed for terramechanics. S-DEM stores wheel-soil interaction forces and soil velocities extracted from DEM simulations. S-DEM reproduces drawbar pull and driving torque for wheel locomotion on flat and rough terrain, though wheel sinkage error can be significant. Computational costs are reduced by three orders of magnitude, bringing the benefits of DEM modeling to vehicle design and control.

CHAPTER 1

Introduction

1.1 Motivation

In the middle of the twentieth century researchers began developing the field of terramechanics, the study of the interaction between running gear and terrain, which led designers beyond empirical design methods and brought about greater insight and advances to off-road vehicle capabilities. Much of the research focused on large, heavy military vehicles used off-road in the wars of the twentieth century. The rise of small unmanned ground vehicles (SUGVs), with their increased autonomy, reduced size, and reduced mass, requires new examination of the interaction between vehicle and terrain and the techniques used to model this interaction.

Small unmanned ground vehicles play an important role in many industries, from planetary exploration to military defense. The NASA rovers Spirit and Opportunity have provided useful information about Mars for years, while requiring significantly fewer resources compared to a manned mission. The United States military has used thousands of teleoperated SUGVs, reducing the risk to human life while performing important tasks such as explosive disposal. The usefulness of SUGVs will only increase as advances continue to be made in fields such as computer vision and artificial intelligence.

Whether a SUGV is used to explore foreign planets or to assist a soldier, the vehicle must not fail. Terramechanics modeling used during the design process can help prevent failures resulting from limited mobility, whether as a result of immobilization while traversing difficult terrain or from energy depletion. When the NASA rover Spirit was traversing weak Martian soil, large sinkage developed leading to immobilization. SUGVs cannot afford to become immobilized; there may not be a human nearby to provide assistance. Meeting range requirements is particularly difficult for SUGVs due to the use of batteries for their main power source, which have significantly lower power

and energy densities compared to petroleum fuels [1]. In response to the success of SUGVs they are being asked to function longer and perform more tasks, further straining their power resources [2]. Recent research has questioned whether traditional terramechanics methods developed for large, heavy vehicle can accurately predict SUGV performance [3] [4]. Furthermore, soils are generally weaker in the near-surface and traction for lighter/smaller vehicles is more dependent on the soil behavior to a smaller depth. In addition, soil surface roughness may have a significantly greater impact on SUGV performance compared to heavy military vehicles as a result of their scale, being one to three orders of magnitude smaller on average. Even recently the military is developing methods to represent the performance of these vehicles in Army models and simulations which were developed for larger manned vehicles [5]. It is important to use the most accurate terramechanics modeling methods available during the design process to ensure operational requirements are met.

After the vehicle's mobility has been optimized, higher level control, navigation, and localization functionality can be developed to maximize its capabilities and efficiency during operation. High fidelity simulation that includes sensor models can be used to evaluate the control systems, such as path planning and navigation [6]. The design stage should include as much modeling fidelity as possible to best gauge performance, however computation speed is crucial for online control systems. High level control, such as traction control and navigation, can be further improved by incorporating terramechanics modeling. Path planning, for instance, can be improved by estimating the energy required for each possible course. Online implementation requires terramechanics modeling methods with fast computation speeds and minimal computation resource requirements. Nevertheless, computation accuracy is still important to reduce the likelihood of immobilization. The development of terramechanics methods which have high fidelity and low computation costs is a significant challenge.

1.2 Background

Off-road locomotion performance is heavily dependent upon the interaction between running gear and soil. This interaction is largely responsible for the vehicle's energy efficiency and mobility. While the percentage of power used by locomotion can vary based on many factors such as vehicle type and mission objectives, vehicle-terrain interaction can easily be the largest consumer. The amount of energy consumed during locomotion is a function of the thrust and resistance forces produced at the interface. If the vehicle cannot produce enough thrust to overcome the resistance then the vehicle may become immobilized. Unlike road vehicles where thrust is largely a function of wheel state, off-road vehicle performance must also consider the soil state. The field of terramechanics studies the interaction between machine and terrain, whether the machine is a vehicle or working machinery, such as earthmoving equipment. Terramechanics allows engineers to improve off-road vehicle performance through the use of scientific methods, not intuition or trial-and-error.

1.2.1 Terramechanics Modeling

Early improvements in wheeled travel came largely through experimentation, including the use of paved roads beginning in the ancient Roman Empire. Even as late as World War I the development and advancement of tracked vehicles occurred not through an understanding of soil mechanics, but through increased empirical knowledge resulting from repeated failure. Designers learned through costly failures in France to increase vehicle track width by 35%, rather than through knowledge of soil bearing capacity [7]. Improvements to wheeled locomotion continued to be based largely on empirical knowledge gained through trial and error until Terzaghi introduced the principles of soil mechanics in 1920 [7]. After World War I researchers began to look scientifically at the problem of wheel/track-soil interaction, considering important phenomena such as movement resistance and sinkage [7]. Still, improvements to off-road vehicles were largely the result of transference of technology and engineering from other fields, including passenger vehicles, rather than through an improved understanding of wheel-soil interaction mechanics. The field of terramechanics began to emerge as a result of the interest in land locomotion mechanics generated by the pioneering work of Dr. M.G.

Bekker [8]. His books *Theory of Land Locomotion* [7], *Off-the-Road Locomotion* [9], and *Introduction to Terrain-Vehicle Systems* [10] published in 1950, 1960, and 1969, respectively, are still frequently cited.

Many techniques for analyzing wheel-terrain interaction have been developed and improved upon. Even Dr. Bekker in his first 1956 text used multiple modeling techniques to describe the interaction. Techniques today include purely empirical methods, purely theoretical methods, purely numerical methods, and combinations of each of these. No method is ideal for all circumstances, and research continues on each method.

Empirical methods are perhaps the oldest type of terramechanics model. Empirical models are developed by first gathering experimental test data from a vehicle or single wheel for specific operating conditions. Correlations between the measured results and the vehicle, wheel, and operating conditions are then developed. Empirical methods can predict performance, but often cannot explain the physical phenomena behind the terramechanics. One of the best known empirical methods for predicting and evaluating wheeled vehicle performance was developed in the 1960s by the US Army Corps of Engineers Waterways Experiment Station (WES), which formed the basis for the NATO Reference Mobility Model (NRMM) [8]. Empirical models require extensive testing in order to develop accurate correlations. As an example, the performance of a tractor during plowing was measured in 14 different fields to develop empirical equations for tractor performance[11]. The impact of multiple military vehicle passes on terrain disturbance was evaluated experimentally to determine empirical model coefficients, as another example [12]. The empirical Pacejka “magic formula” developed for road wheel has even been applied for off-road farm tractor force prediction [13]. Empirical models can be useful for accurate, rapid evaluation of the performance of wheels (or wheeled vehicles) for the specific operating conditions used during model development. The specificity of empirical models is perhaps both its biggest strength and biggest weakness. By limiting the model’s scope, empirical methods can be highly accurate. However, such a model cannot be safely extrapolated outside of the conditions upon which it was based. The simplicity of empirical models results in short computation requirements, which can be useful for both vehicle design and online control. However, the limited scope of

empirical models limits their role in prediction of wheel performance under new operating conditions. Finally, the time and cost of performing the experimental testing required for all wheel/soil/operating condition combinations can be prohibitively expensive and time consuming.

At the other end of the spectrum are purely theoretical methods for terramechanics modeling. The following is a discussion of highly idealized elastic-plastic models, although more advanced nonlinear models exist. For loads which do not cause failure, classical theory of elasticity can be applied. As the stress on the soil increases, the strain increases linearly. Once the stress is released, the soil returns to its original state. The stress within the soil for a certain type of loading (e.g. circular loading for wheels or uniform strip loading for tracks [7]) can be calculated by solving partial differential equations with known boundary conditions. However, sometimes loads are large enough to cause soil failure. When this happens, the linear relationship between stress and strain breaks down, and a rapid increase in strain can occur. Under these conditions, plasticity theory must be applied. The most widely used failure criterion is Mohr-Coulomb, which relates the maximum shear stress of a material to the normal stress on the surface and the material's cohesion and internal shearing resistance [8]. Forces can be calculated by integrating the normal and shear stresses over a defined contact area, such as the interface between a wheel and soil. Given the complexity of vehicle-terrain interaction, many simplifications and assumptions are necessary to solve for reaction forces using purely theoretical methods [14].

In order to overcome the deficiencies of theoretical methods, researchers began combining theoretical and experimental work. One such work, pioneered by M.B. Bekker, is described as “semi-empirical” and will be referred to as the Bekker method, to differentiate it from other semi-empirical methods. Although uncommon, other semi-empirical methods have been developed, including one developed by using system identification techniques to infer mathematical models for wheel-soil interaction from experimental data [15]. The Bekker method incorporates some elements of the theoretical method, such as the Mohr-Coulomb criterion for shear stress, along with relationships derived empirically through experimentation. In the case of wheel-soil interaction the Bekker method describes the distribution of normal and shear stress along

the wheel-soil interface, dependent on wheel properties (e.g. wheel radius) and state (e.g. slip ratio). The specifics of this method will be described in more depth in the next chapter. The Bekker method has become the industry standard due to its relative ease of computation and its ability to fit experimental data through tuning.

The Bekker method was used in the 1960s during the development of the lunar rover wheels to motivate the development of a flexible wheel which could maximize the wheel-soil contact area, however wheel design was largely experimentally-based due to limitations in the available terramechanics modeling methods and the limitations in computation performance [16] [17]. Over time the Bekker method has been modified and expanded to add additional modeling features, such as the ability to model wheel lugs [18] [19] [20] [21], flexible wheels [22] [23] [24] [25], multipass effects [23] [24] [25], rate effects [26], and rough terrain with lateral motion [27] [28] [19] [23] [21] [29] [24]. Many of these modifications either ignored fundamental assumptions of the underlying method, or require even more empirical coefficients which may be difficult to experimentally determine. Terramechanics simulation plays a much greater role in the design of more recent vehicles, including the use of the Bekker method to design a future Mars rover [30] and a SUGV [31]. Additional design tools have been developed using the Bekker method [32] [33] due in part to its relatively fast computation speed, which is crucial when optimizing design parameters. Nevertheless researchers have investigated ways to further increase computation speed by linearization of stress distributions, primarily for the purpose of online control [34] [35] [36] [37]. This technique was used to create a traction control algorithm which resulted in reduced power consumption and greater mobility [38]. Autonomous navigation operations, such as terrain classification and path following [39] [40] [41] [42] [43], can be improved by incorporating predicted mobility.

Empirical and semi-empirical methods, like the Bekker method, are limited in their application due to their reliance on experimental data and their modeling simplifications and assumptions. The Bekker method contains parameter coefficients which can only be determined through wheel locomotion experiments, and generally assumes steady-state operation. It is undesirable to need to perform new experimental wheel tests in order to develop an empirical model or to determine empirical parameter

coefficients. Experimental facilities require significant resources, including lab space, soil preparation, personnel, and maintenance [44]. In addition, test repeatability can be difficult given the influence of parameters such as moisture content and initialization stress. Recent experimental studies have examined the effect of lug spacing [45], tread pattern [46], pneumatic tire inflation pressure [47], and grouser length [18], to name a few. While experimental tests are invaluable for simulation validation and design evaluation, simulations should be performed when possible.

Numerical methods, such as the Finite Element Method (FEM) and the Discrete Element Method (DEM), have been used for terramechanics modeling since the 1970s and continue to increase in popularity as computing resources improve [8]. Large-scale dynamic effects are the result of many small-scale interactions, whether modeled as a continuous medium in the case of FEM, or as many individual particles in the case of DEM. Numerical methods are capable of modeling the complex interactions that can occur during soil interaction, including the soil dynamics of an irregular wheel traversing rough terrain, without the need to impose restrictive constraints or assumptions. Traction predictions based on 3-dimensional surfaces have been shown to be more accurate compared to 2-dimensional predictions [48]. FEM has been used to model rigid and flexible wheel-soil interaction for longitudinal and lateral slip [49] [50] [51] [52] [53] [54]. Newer FEM techniques like the Coupled Eulerian-Lagrangian method are even capable of modeling large deformations [55] including those caused by grousers [56]. As SUGVs often travel on granular terrain, such as sand or lunar regolith, the ability to model individual particles and capture particle motion using DEM is a unique advantage. DEM has been used to model wheel digging/excavation [57] [58], wheel locomotion [59], and bulldozer blade soil interaction [60]. The capability for simulating additional tool-terrain interaction, such as an auger or a foot, has also been demonstrated [61]. The simulation capabilities of numerical methods allow more realistic simulation and analysis of wheel-terrain interaction which can be used for the benefit of vehicle design and control. As an example, 2D DEM simulations, after experimental wheel locomotion validation, were performed to examine the influence of wheel normal load, grouser length, number of grousers, and gravitational force on wheel performance [62] [63].

Contrary to the previous example, numerical methods have not reached widespread popularity due to their high computation costs. A performance analysis of FEM using the arbitrary Lagrangian-Eulerian formulation showed that a system of 4,000 elements would require combined cpu performance of 80 GFLOPS, while a system of 256,000 elements would require combined cpu performance of 20,398 GFLOPS [64]. While computation capability continues to increase exponentially, current processor performance is roughly 20 GFLOPS per core. Simulating wheel-terrain interaction over a meaningful distance with reasonable element resolution using FEM remains highly computationally intensive. Computation performance is typically even worse for DEM. Some researchers have resorted to modeling the bottom layer of soil using FEM, with the top layer of soil modeled using DEM [65] [66] [67]. This technique attempts to retain the granular soil modeling capability of DEM but with reduced computation cost. Numerical methods are impractical for use in vehicle control given the current available computation resources.

1.2.2 Rough Surface Locomotion

SUGVs pose a new challenge to the terramechanics field given their small size. As a matter of scale, surface profiles which are considered “smooth” for large, heavy vehicles may become “rough” for small robots. Rough terrain can cause vibrations through the vehicle-soil interface. Both the amplitude and the frequency of these vibrations have been shown to influence the normal and shear forces developed at the interface [68] [69] [70] [71]. As a vehicle travels over rough soil not only is the terrain profile modified by the interaction, the vibrations generated by the interaction can change the physical properties of the soil itself [70] [71].

Previous studies on the impact of surface roughness have typically used a mass-spring-damper approach to vehicle and soil modeling. The influence of suspension parameters on vertical acceleration during rough surface locomotion was studied using a numerical quarter-vehicle model using Bekker-type pressure/sinkage relationships [72]. The impact of vibration frequency on soil compaction was studied using linear and non-linear rheology-based mass-spring damper models [73]. While these methods may be able to determine some statistical measure of the effect of roughness on vehicle-terrain

interaction over time, they cannot be relied upon to accurately model the locomotion of a vehicle over rough terrain.

A two-dimensional Finite Element Method study of a vehicle operating on an uneven terrain showed that dynamic wheel loads, resulting from vehicle pitch moments and vertical oscillation, and ground deformation are interdependent [50]. The interaction between vehicle and terrain is fundamentally three dimensional and dynamic. A three-dimensional application of this method could potentially help vehicle designers, however the computation requirement would likely exclude its application in online control.

Bekker type equations have been used to model three dimensional full vehicle dynamics simulations of off-road locomotion [74] [75] [21] [76] [77]. Several of these studies also included experimental validation when operating on flat terrain [77] [21]. More ambitious studies modified the Bekker method further to simulate three-dimensional vehicle motion over rough terrains [24] [19] [27] [78]. A physics-based three-dimensional simulator was created where the soil subsurface stress distribution was modeled primarily using Boussinesq's equations for stress in a semi-infinite, homogeneous, isotropic, elastic medium subject to a vertical point load [79]. The primary weakness of these models is they rely upon equations that were developed for static or steady-state conditions.

1.3 Research Objective and Scope

The focus of this dissertation is the development of terramechanics methods for SUGV design and control on granular terrain. During vehicle design the modeling fidelity is critical for accurate mobility prediction, however during vehicle control the computation speed is critical in order to perform mobility calculations online as frequently as necessary. Current terramechanics models require a tradeoff between fidelity and efficiency. In general, empirical and semi-empirical methods are relatively efficient but limited due to their underlying assumptions while numerical methods have great modeling capabilities but are less proven and less efficient. Ultimately, a single terramechanics model is desired that can provide a high level of fidelity and computation speed.

The Bekker method, while relatively efficient, has several drawbacks which limit its use in online real-time control applications. Inputs to the method include wheel sinkage and slip, while outputs include wheel forces and torques. Only through iteration can the correct sinkage value be found for a given normal load. Numerical integration must be performed each iteration, and the calculations must be performed for each wheel. These factors contribute to a computation cost that can be significant. When used online for vehicle navigation, many calculations must be performed to predict vehicle mobility during path selection. In addition, the vehicle must perform other calculations beyond terramechanics, such as terrain classification. This dissertation presents two techniques which aim to significantly reduce computation cost, providing greater opportunity for the use of terramechanics during vehicle operation.

Ensuring the mobility of SUGVs during the design phase is crucial to their successful mission operation. Given the relatively small size and mass of SUGVs compared to traditional military vehicles for which much of terramechanics methods were developed, additional design factors such as surface roughness should be investigated. The assumptions and limitations of the Bekker method make it a poor choice for such an analysis. The discrete element method provides modeling capabilities beyond those of the Bekker method, such as the ability to model soil dynamics, which make it a better choice. In this dissertation DEM was used to evaluate the potential impacts of surface roughness on SUGV performance, and help determine whether surface roughness should be included during the SUGV design phase.

While DEM has great potential to improve terramechanics modeling fidelity, it is necessary to compare its computational accuracy with the more common Bekker method. While the Bekker method is frequently tuned to match experimental wheel test results, the real benefit of terramechanics is the ability to predict performance. Both DEM and Bekker parameters were tuned according to soil tests and flat terrain wheel locomotion simulation results were compared with experimental data. During DEM tuning, a modification was made to the rolling resistance term to improve simulation accuracy. This comparison uses steady-state performance over flat terrain, the optimal test case for the Bekker method. Performance comparisons outside the original assumptions of the

Bekker method, such as locomotion on rough terrain, are expected to be more favorable for DEM.

Although techniques were developed to improve the computation speed of the Bekker method and to improve the fidelity of DEM, the ultimate goal is to obtain computation efficiency and modeling fidelity within one model. DEM has already shown significant modeling capabilities for wheel-terrain interaction of granular soils and its modeling fidelity is likely to increase as new modeling techniques are developed. Current techniques to reduce computation cost include reducing Young's modulus values, increasing particle size, or performing 2D simulations. These techniques reduce model accuracy and capability, and do not produce significant computation gains to be competitive with semi-empirical methods. This dissertation proposes a surrogate model to significantly reduce computation cost while retaining many of the desirable features of DEM, including the modeling of soil dynamics.

1.4 Contributions

This research aims to improve terramechanics modeling for small wheeled vehicles operating in granular soil for the use in vehicle design and control. Given the importance that wheel-terrain interaction has on mobility and efficiency, terramechanics models must be accurate. If the wheel-terrain interaction is poorly modeled then the vehicle may operate at a lower efficiency or simply become immobilized. During vehicle design these calculations must be performed numerous times, while during operation the vehicle controller must perform the calculations quickly. The proposed improvements to terramechanics modeling address both the computation speed and the model accuracy required for design and control. The main contributions of this dissertation are as follows:

- Increase computation speed for Bekker-type terramechanics calculations

Two methods were developed to improve computation speed, a lookup table method and a quadratic approximation method. The lookup table method performs all computations offline, requiring interpolation of a few tables during online use. The quadratic approximation method results in a closed form solution with minimal error.

- Quantify the effects of rough terrain on SUGV locomotion

Discrete element method simulations were performed for a representative SUGV wheel operating on rough terrain with a sinusoidal profile. The average drawbar pull decreased while driving torque increased, which shows that mobility and efficiency are reduced for SUGVs operating in rough granular terrains.

- Directly compare prediction performance of DEM and Bekker methods

In order to determine whether the increased computation cost of DEM produces better results compared to the Bekker method, both methods were tuned to match soil tests and used to predict steady-state wheel locomotion performance. Simulation results were compared with experimental results, which showed DEM to more accurately represent performance trends while producing lower error. While the Bekker method can easily be tuned to match wheel performance results, DEM was shown to better predict wheel performance.

- Develop an improved rolling resistance model for DEM using spherical particles

During DEM parameter tuning it was discovered that a modification was necessary to match both pressure-sinkage and direct shear experimental results simultaneously. DEM simulations of pile formation in the literature showed that particle rolling resistance depended on the relative motion between particles [80]. Modifying the rolling resistance model to include a velocity dependent term allowed for spherical particle DEM to be tuned to fit both test types.

- Develop a simulation technique to reproduce the capabilities of DEM with increased computation speed

While the discrete element method has many advantages compared to the Bekker method, including the ability to model rough terrain, its computation time limits its usefulness. A surrogate DEM model was developed that reproduces DEM interaction behavior but at a significantly reduced cost. The surrogate model was validated on flat and rough terrain, reproducing drawbar pull and driving torque well. Further development is required to improve wheel sinkage accuracy. This marks one of the first surrogate models developed for DEM, and the first known model developed for terramechanics.

1.5 Outline of the Dissertation

The remainder of this dissertation organized as follows. Chapter 2 reviews the Bekker method and presents two methods for increasing the computation speed of traditional Bekker method calculations. Chapter 3 presents the work on modeling of rough terrain using the discrete element method, and its impacts on wheel-terrain mobility and efficiency. Chapter 4 presents the parameter tuning of the discrete element and Bekker methods, and wheel locomotion prediction performance. Chapter 5 presents the development and evaluation of the surrogate discrete element model. Finally, Chapter 6 presents the conclusions of the dissertation and recommendations for future work.

CHAPTER 2

Fast Computation Semi-Empirical Terramechanics Models

The Bekker model is the most commonly used method for performing terramechanics calculations; it can be very accurate while also computationally efficient compared to numerical methods. Even with its comparative speed advantage, there are occasions in which the Bekker method is too slow to compute. These occasions can occur in both vehicle design and vehicle control. In both cases many terramechanics calculations must be performed quickly, especially in the case of online vehicle control. In response to this need two methods for increasing computation speed of the Bekker method, a lookup table method and a quadratic approximation method, were developed. First a detailed review of the Bekker method is given, followed by descriptions of the two new methods.

2.1 Bekker Modeling Review

Bekker terramechanics modeling methods, named after the pioneering work of M.B. Bekker, define the force interaction between wheel and soil as a function of wheel and soil states. The Bekker method simplifies wheel-soil interaction by modeling the wheel as a rigid cylinder traveling on smooth, flat soil. The geometry of the wheel and soil during locomotion is depicted in Fig. 2.1. In the figure, the wheel is moving at steady-state in the horizontal plane (constant linear velocities v_x and v_y) and rotating about the y -axis with angular velocity ω . The Bekker method assumes that the wheel is significantly more rigid than the soil such that the wheel does not deform, but rather sinks into the soil. In the figure h_f defines how much the wheel initially compacts the soil in the z -axis, while h_r defines how much the soil recovers in height following the wheel. The entry contact angle θ_f and the exit contact angle θ_r along the wheel surface are

functions of the soil compaction and recovery, determined from the geometry shown in Fig. 2.1:

$$\begin{aligned}\theta_f &= \cos^{-1}(1-h_f/r) \\ \theta_r &= -\cos^{-1}(1-h_r/r)\end{aligned}\quad (2.1)$$

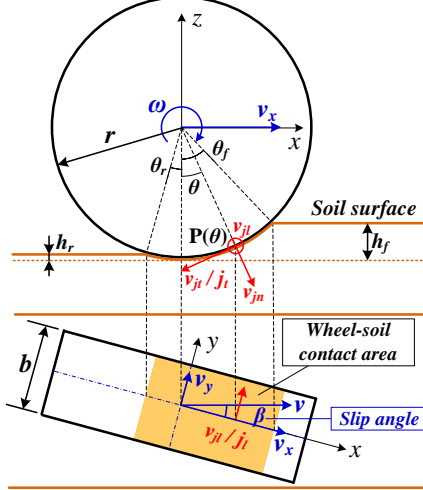


Figure 2.1 Wheel-soil contact geometry (cylindrical surface, positive wheel slip) [81]

As in the case of on-road driving, the wheel cannot produce thrust unless the wheel angular velocity is greater than the vehicle angular velocity (the quotient v_x and wheel radius r). This phenomenon is referred to as the wheel slip ratio, s , defined by:

$$s = \begin{cases} (r\omega - v_x)/(r\omega) & (\text{if } |r\omega| > |v_x|: \text{driving}) \\ (r\omega - v_x)/v_x & (\text{if } |r\omega| < |v_x|: \text{braking}) \end{cases} \quad (2.2)$$

Circumstances such as vehicle turning can result in lateral velocity along the y -axis. Wheel slip angle β , defines the ratio between longitudinal and lateral velocity:

$$\beta = \tan^{-1}(v_y/v_x) \quad (2.3)$$

As the wheel travels, normal and shear stresses develop along the wheel-soil interface (from θ_f to θ_r). The bevameter technique, developed by Bekker, can be used to characterize soil types and measure terrain properties used for soil stress models. The bevameter technique consists of two parts: one is a set of plate penetration tests to characterize the normal stress-displacement relationship, the second is a set of shear tests to characterize the shear stress-displacement relationship. A schematic of the characteristics of a bevameter is provided in Fig 2.2. The bevameter technique can

perform tests in-situ using loads which are characteristic of vehicle operation, providing an advantage compared to traditional methods such as a triaxial compression test. Unfortunately the soil parameters determined by the bevameter technique can depend on the plate size, normal load, and penetration/shear rate during testing.

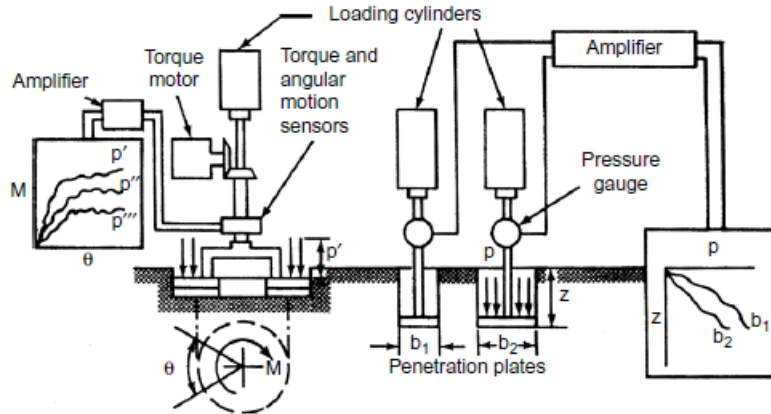


Figure 2.2 Bevameter schematic [8] (originally printed in [10])

The Bekker method determines the forces acting on the wheel through integration of the normal and shear stress along the wheel-soil interface. Normal, tangential, and lateral stresses are distributed along the wheel interface as shown in Fig 2.3. Through experimental testing, along with the bevameter technique, researchers developed functions to describe the stress distribution along the interface.

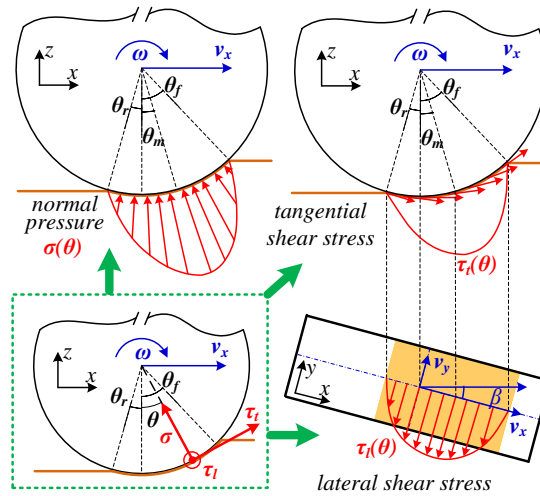


Figure 2.3 Normal and shear stress distributions along the wheel-soil interface [81]

Wong and Reece developed a formula for describing the normal pressure along the wheel-soil interface using the results of plate penetration tests [82]:

$$\sigma(\theta) = (k_c/b + k_\phi) z(\theta)^n$$

$$\text{where } z(\theta) = \begin{cases} r(\cos \theta - \cos \theta_f) & \theta_m \leq \theta \leq \theta_f \\ r(\cos \theta_e - \cos \theta_f) & \theta_r \leq \theta \leq \theta_m \end{cases} \quad (2.4)$$

where b is the wheel width, and k_c , k_ϕ , and n are constant soil properties corresponding to cohesive modulus, frictional modulus, and sinkage exponent. The soil properties can be determined through the bevameter technique. In the front contact region $z(\theta)$ corresponds to the soil sinkage along the wheel-soil interface. For points along the wheel-soil interface where the angle is less than the point of maximum normal stress θ_m , an equivalent front region contact angle θ_e is used. These variables, and an alternate formulation for the rear contact angle, can be defined as:

$$\begin{aligned} \theta_e &= \theta_f - (\theta - \theta_r)(\theta_f - \theta_m)/(\theta_m - \theta_r) \\ \theta_m &= (a_0 + a_1 \cdot s)\theta_f \\ \theta_r &= (b_0 + b_1 \cdot s)\theta_f \end{aligned} \quad (2.5)$$

where the parameters $a_{0,1}$ and $b_{0,1}$ are soil dependent constants.

Functions for describing the shear stress along the interface are slightly more complex. First, the tangential shear rate v_{jt} , the lateral shear rate v_{jl} , and the compression speed v_{jn} at point $P(\theta)$ can be derived from Fig. 2.1:

$$\begin{aligned} v_{jt}(\theta) &= r\omega - v_x \cos \theta \\ v_{jl}(\theta) &= v_y \\ v_{jn}(\theta) &= v_x \sin \theta \end{aligned} \quad (2.6)$$

The corresponding soil shear deformation in the tangential and lateral directions (j_t and j_l , respectively) can be determined by integrating the shear rates using a quasi-static approach:

$$\begin{aligned} j_i(\theta) &= \int_{\theta}^{\theta_f} v_{ji}(\theta) \frac{1}{\omega} d\theta & i = t, l \\ j_t(\theta) &= r[(\theta_f - \theta) - (1-s)(\sin \theta_f - \sin \theta)] \\ j_l &= r(1-s)(\theta_f - \theta) \tan \beta \end{aligned} \quad (2.7)$$

The magnitude of the overall shear deformation is defined as:

$$j(\theta) = \sqrt{j_t(\theta)^2 + j_l(\theta)^2} \quad (2.8)$$

It should be noted that the shear deformation formulas are shown only for the case of positive slip ratios. The case corresponding to negative slip can be derived in a similar manner.

Unlike normal stress, the shear stress distribution along the interface depends greatly on the soil type. Bevameter experiments have shown that different soils have varying shear stress-shear displacement curves, with example curves for three soil types shown in Fig. 2.4.

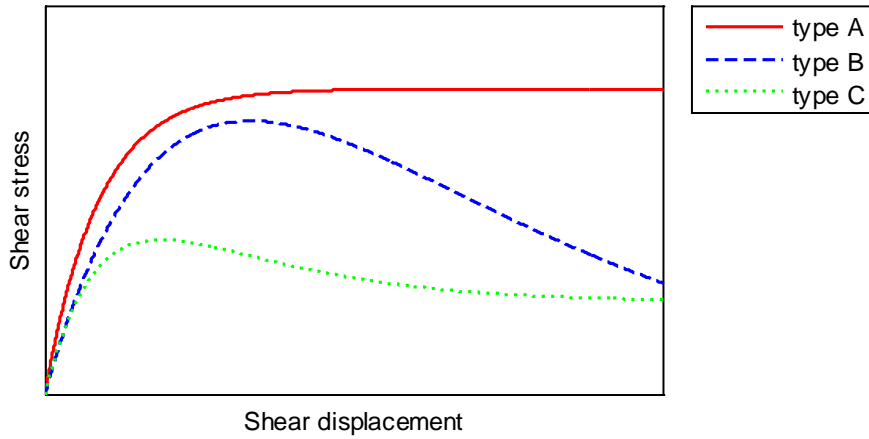


Figure 2.4 Shear stress as a function of shear displacement for three soil types

The magnitude of the overall shear stress along the wheel-soil interface can be described using one of the following formulas, depending on the soil type:

$$\tau(\theta) = \begin{cases} \tau_{max} \cdot \tau_{base,1} & \text{type A} \\ \tau_{max} \cdot \tau_{base,2} \cdot (j/K_w) & \text{type B} \\ \tau_{max} \cdot \tau_{base,1} \cdot K_r [1/(K_r(1-1/e)-1)] & \text{type C} \end{cases}$$

where :

$$\tau_{max} = c + \sigma(\theta) \cdot \tan \phi \quad (2.9)$$

$$\tau_{base,1} = 1 - \exp(-j/K)$$

$$\tau_{base,2} = \exp(1 - j/K_w)$$

where K is the shear deformation parameter(a measure of the magnitude of the shear displacement required for the development of the maximum shear stress), K_r is the ratio of residual shear stress to maximum shear stress, and K_w equals the shear displacement at peak shear stress. The maximum shear stress τ_{max} is described using the Mohr-Coulomb failure criterion, where c and ϕ are the soil cohesion and the soil internal angle of friction,

respectively. The soil properties can be determined through the bevameter technique. The function for type A “plastic” soils, a modified version of Bekker’s equations [8], was proposed by Janosi and Hanamoto [83]. Examples of type A soils include certain types of sand, saturated clay, and fresh snow. Wong proposed the function for type B soils [84], which include internal shearing of muskeg mat. Wong also proposed a modified version of Oida’s equation [8] to describe type C soils [85], which include snow-covered terrains and certain types of loam.

Use of the Bekker method for lateral forces is a more recent development, and so the method for determining the tangential and lateral shear stress is not well established. Here an isotropic shear stress model is presented. The direction of the shear stress at any point on the wheel-soil interface is always opposite the shearing velocity at that point, unlike the anisotropic shear stress approach given in ref. [21]. The isotropic shear stress assumption is analogous to track-soil interaction modeling during steering [86]. Using the isotropic model, the tangential and lateral shear stresses are given by:

$$\tau_i(\theta) = \tau(\theta) \cdot v_{ji}(\theta) / \sqrt{v_{jt}(\theta)^2 + v_{jl}(\theta)^2} \quad (i = t, l) \quad (2.10)$$

The functions for normal and shear stress shown above create stress distributions along the wheel-soil interface, as shown in Fig. 2.5. The forces and torques exerted on the wheel can be determined by integrating the stress distributions. Assuming a cylindrical surface, the forces and torques can be formulated as:

$$\begin{aligned} F_x &= rb \int_{\theta_r}^{\theta_f} (-\sigma(\theta) \sin \theta + \tau_t(\theta) \cos \theta) d\theta \\ F_y &= -rb \int_{\theta_r}^{\theta_f} \tau_l(\theta) d\theta \\ F_z &= rb \int_{\theta_r}^{\theta_f} (\sigma(\theta) \cos \theta + \tau_t(\theta) \sin \theta) d\theta \\ M_x &= -r^2 b \int_{\theta_r}^{\theta_f} \tau_l(\theta) \cos \theta d\theta \\ M_y &= -r^2 b \int_{\theta_r}^{\theta_f} \tau_t(\theta) d\theta \\ M_z &= -r^2 b \int_{\theta_r}^{\theta_f} \tau_l(\theta) \sin \theta d\theta \end{aligned} \quad (2.11)$$

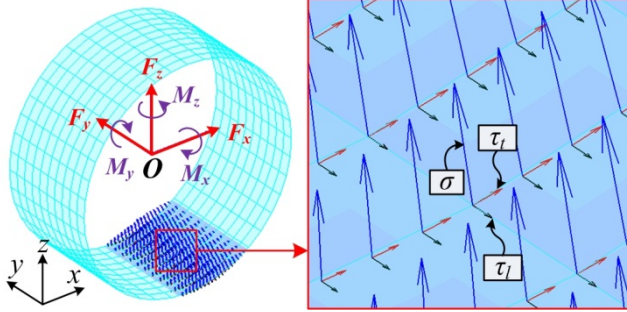


Figure 2.5 Distribution of normal and shear stresses along the wheel-soil contact area [81]

2.2 Bekker Method Computation Limitations

The Bekker method described in Section 2.1 has two major shortcoming which limit its usefulness for vehicle design and control; the integrals for force and torque are not solvable analytically, and the equations are backward-looking (follow the reverse of the physical cause-effect relationship). The typical method used for determining wheel forces is to iterate on the wheel contact angle. For a given front contact angle θ_f , the Bekker equations are solved over a range of possible wheel slip ratio values. If the difference between the calculated and desired normal load is below a given threshold then the process ends, otherwise a new front contact angle is chosen and the process repeats. This method can require several iterations for convergence, and each function evaluation requires several numerical integrations. Two methods were developed to help improve computational efficiency when calculating Bekker equations. The first method uses lookup-tables to improve online efficiency. The second method makes an approximation about the shape of the stress distributions along the wheel-soil interface, which results in a closed-form solution.

2.3 Lookup Table Method

In both vehicle design and vehicle control solving recursively for wheel forces using the Bekker model can require too much time and waste computation resources. For a specific wheel these computations can be performed offline for all reasonable operating conditions, and stored using lookup tables. The improved computation speed can result

in real time computation of vehicle performance over a future terrain profile, which benefits both vehicle designers and vehicle control systems.

Before describing the method by which the lookup tables are created and used, the Bekker method described in Section 2.1 is modified to include the impact of repetitive loading on the soil normal stress relationship. When considering vehicles with wheels in a tandem configuration (one wheel directly in front of another), the terrain does not completely recover after the front wheel compacts the ground. When the rear wheel traverses the same region the ground will behave differently. Figure 2.6 shows how repetitive normal loading can influence the relationship between soil pressure and wheel沉降 for a mineral terrain (e.g. sand, sandy loam, clayey loam, and loam) [8].

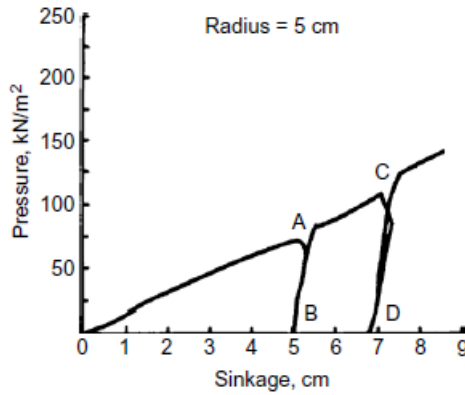


Figure 2.6 Response to repetitive normal load on a mineral terrain [8]

When the wheel first contacts the soil, pressure and sinkage build until the wheel leaves the soil at unloading point A. The soil does not fully “recover” to zero sinkage before a new load is applied at reloading point B. The relationship between pressure and sinkage has been altered compared to undisturbed soil, with a different slope and sinkage at zero pressure. Once the pressure reaches the initial unloading point A, the soil follows the original “virgin” pressure-sinkage relationship. This process is repeated with points C and D. The normal load during unloading and reloading is given by:

$$\sigma_{(un/re)loading}(\theta) = \left(k_c/b + k_\phi \right) z_u^n - \left(k_o + A_u \cdot z_u \right) (z_u - z(\theta)) \quad (2.12)$$

where k_o and A_u are soil constants and z_u is the sinkage at unloading.

Another modification made to the Bekker method accounts for the changes in soil dynamics which occur during braking. When braking, the location of the maximum normal stress along the wheel-soil interface may be different than during acceleration.

Wong [8] accounted for this change by altering the equation for maximum normal stress θ_m during negative slip:

$$\theta_m = \cos^{-1} \left(\frac{1+s}{\sqrt{1+\tan^2\left(\frac{\pi}{4}-\frac{\phi}{2}\right)}} \right) + \tan^{-1} \left(-\tan\left(\frac{\pi}{4}-\frac{\phi}{2}\right), 1 \right) \quad s < 0 \quad (2.13)$$

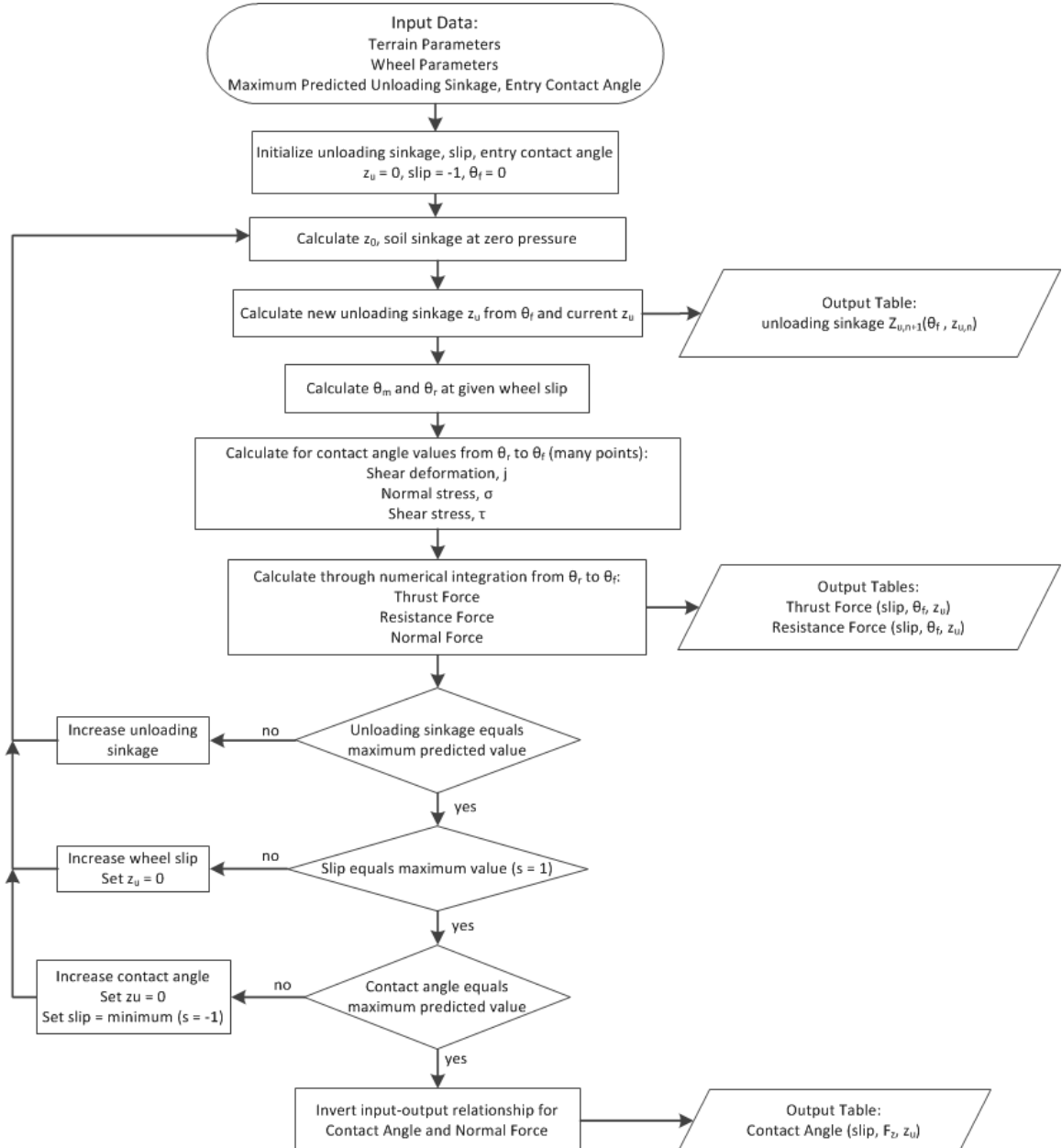


Figure 2.7 Flow chart for building wheel lookup tables [87]

In order to build the wheel lookup tables, the modified Bekker equations must be solved for all possible circumstances. New tables must be generated for all combinations of wheel parameters (e.g. wheel radius) and terrain types (e.g. dry sand). The maximum entry contact angle θ_f , relating to the maximum wheel sinkage, must be limited to a realistic value. Figure 2.7 charts the procedure for building wheel lookup tables, and shows the resulting output tables. The procedure ensures that tables are built which cover the entire range of possible slip ratios, entry contact angles, and unloading sinkage values.

Example lookup tables are given in Figures 2.8 to 2.11 for a smooth wheel with radius 0.1m, width 0.1m, operating on loose air dried sand. Bekker terrain properties for loose air dried sand [8] are given in Table 2.1.

Table 2.1 Soil parameter values for loose air-dried sand [8]

Parameter [unit]	c [kPa]	ϕ [rad]	n [-]	K [m]	k_c [kN/m $^{n+1}$]	k_ϕ [kN/m $^{n+2}$]
Value	0	0.478	0.91	0.005	-0.66	754.13

Parameter [unit]	a_0 [-]	a_1 [-]	b_0 [-]	b_1 [-]	k_o [N/m 3]	A_u [N/m 4]
Value	0.18	0.32	0	0	-0.66	$503 \cdot 10^6$

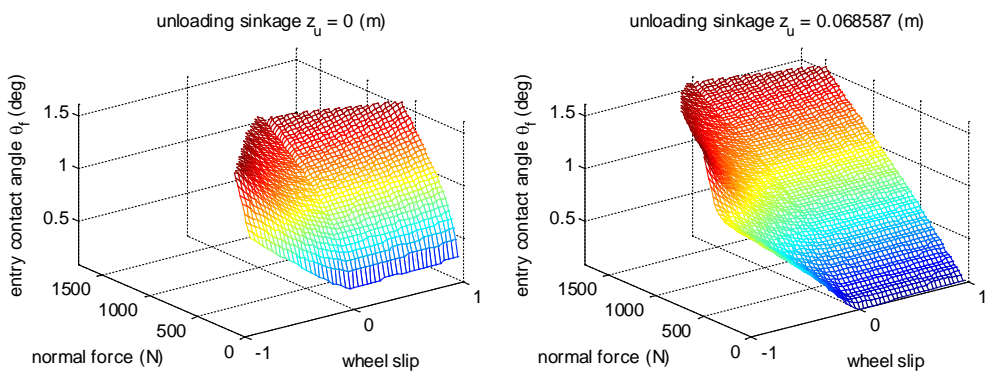


Figure 2.8 Example wheel lookup tables: entry contact angle [87]

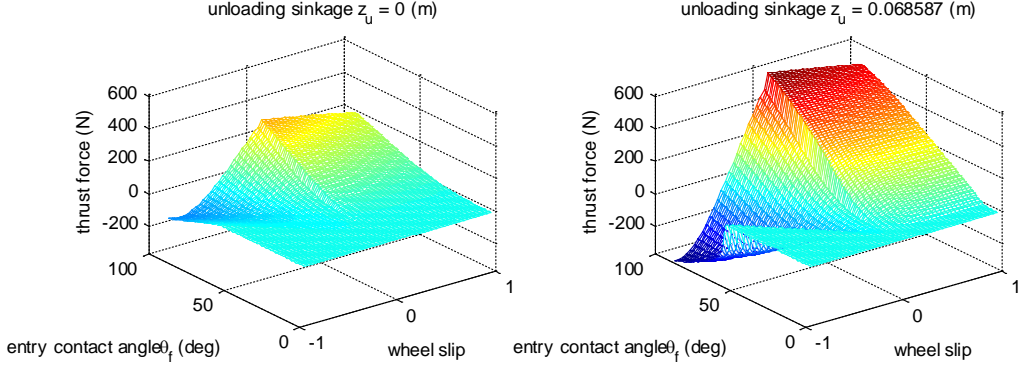


Figure 2.9 Example wheel lookup tables: thrust force [87]

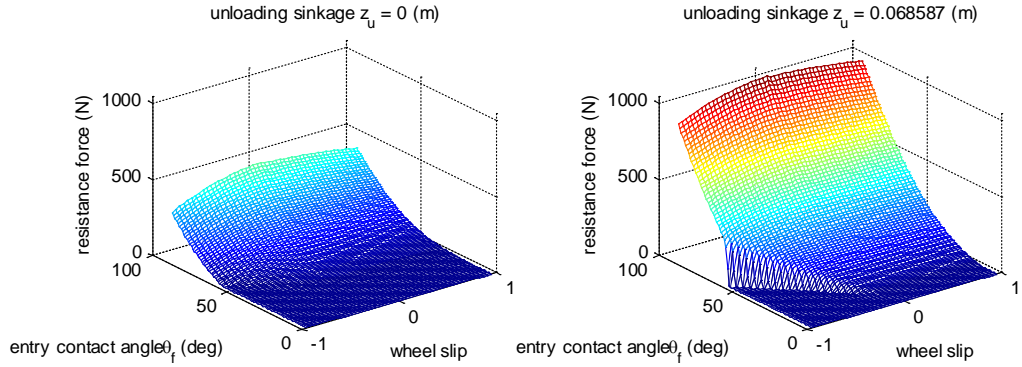


Figure 2.10 Example wheel lookup tables: resistance force [87]

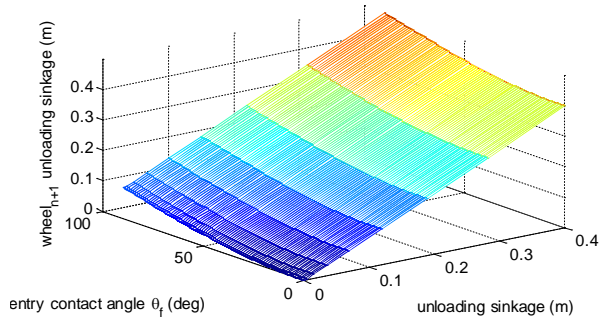


Figure 2.11 Example wheel lookup table: unloading sinkage [87]

A graphical design tool was developed for small off-road SUGVs which used the lookup table method to reduce terramechanics computation time [87]. The design tool, termed the Off-Road Robot Design Tool (ORRDT) consists of three stages. The first stage examines system feasibility based on total system mass. The second stage allows the user to examine a performance measure, such as energy required, as a function of two vehicle parameters. The third stage compares vehicle performance of a range of vehicle configurations for a predetermined mission profile. This stage also performs iterated

vehicle design optimization and velocity profile optimization. A screenshot of ORRDT performing design and velocity optimization is shown in Figure 2.12. As implemented in Matlab, interpolation using the lookup table method resulted in a two orders of magnitude reduction in computation time compared to Bekker method calculations performed in C.

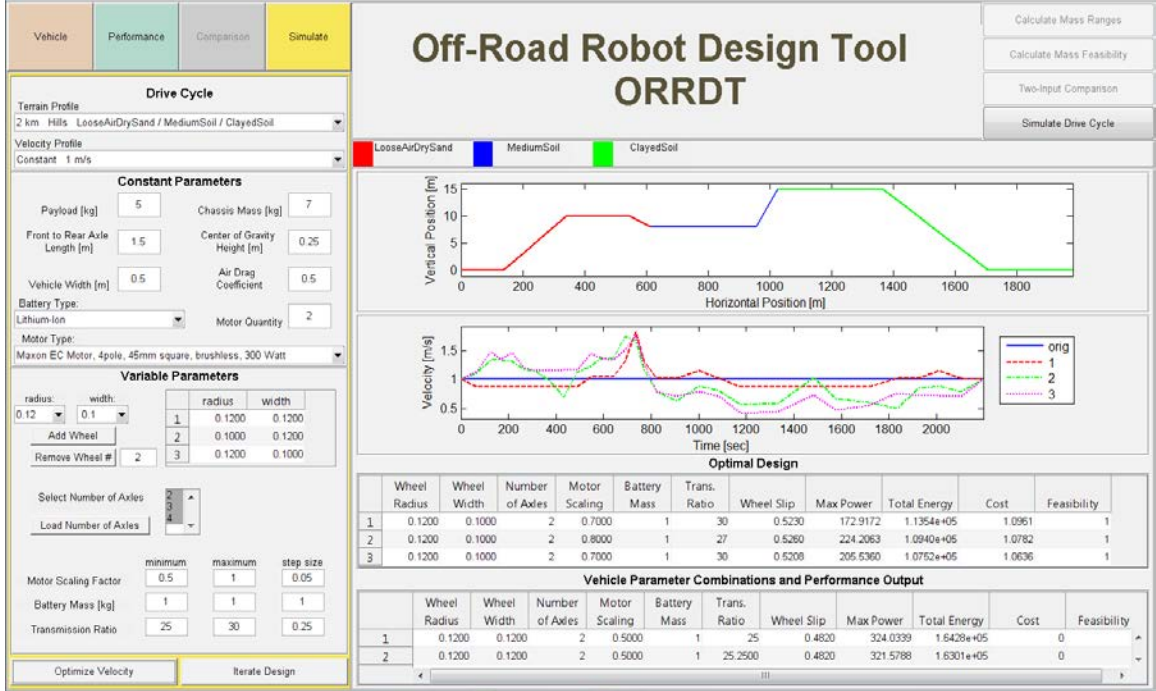


Figure 2.12 ORRDT screenshot performing vehicle design and velocity optimization [87]

2.4 Quadratic Approximation Method

The lookup-table method can drastically improve online computation time, but it has several limitations. Perhaps the most important is that it does not reduce the time required for the Bekker calculations themselves. Worse, the calculations must be made offline for the entire search space. The principle time consumer in the Bekker equations is the integration of normal and shear stress along the wheel-soil interface, required to calculate force and torque. The complexity of the stress distribution equations prevents a closed-form solution. Iagnemma showed that a linearization of the stress distribution equations results in a closed-form solution [37], however errors could be large at times and model accuracy could not be guaranteed. Stress distributions can be especially nonlinear for soils with low sinkage exponents, as shown in Fig 2.13. A closed-form

solution with significantly reduced error using quadratic approximation of the stress distributions along the wheel-soil interface was developed in collaboration with Zhenzhong Jia, and is described below. It should be noted that the method of modeling lugged wheels was the work of Zhenzhong Jia, and is presented here since it was used when evaluating the quadratic approximation method. In addition, while the idea to use quadratic equations to approximate the stress distributions originated from the author, the majority of the work shown below was performed by Zhenzhong Jia.

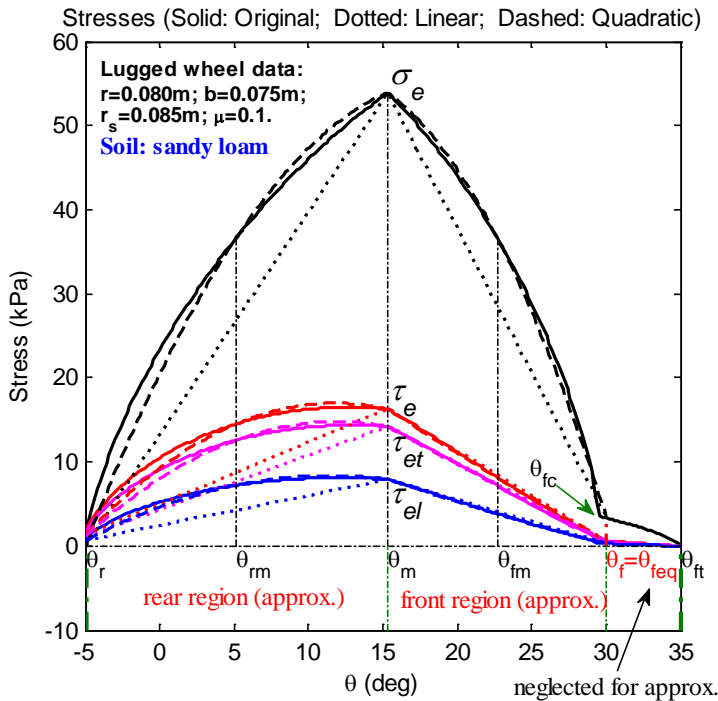


Figure 2.13 Stresses for a lugged wheel traveling on sandy loam, calculated using the original non-linear model, linear approximations, and quadratic approximations [77]

2.4.1 Modeling of Lugged Wheels

The following describes a modification made to the Bekker model used by the quadratic approximation method. In off-road applications, the domain in which terramechanics modeling is most important, wheels are often installed with grousers to improve traction performance. The influence on wheeled performance of grousers, or lugs, has been observed in many field experiments [88] [89]. Figure 2.14 shows a typical lugged wheel where r is the radius of the concave region (wheel radius not including the

grouser), h_g is the lug height, and μ is the area ratio of the grouser tip and the concave region.

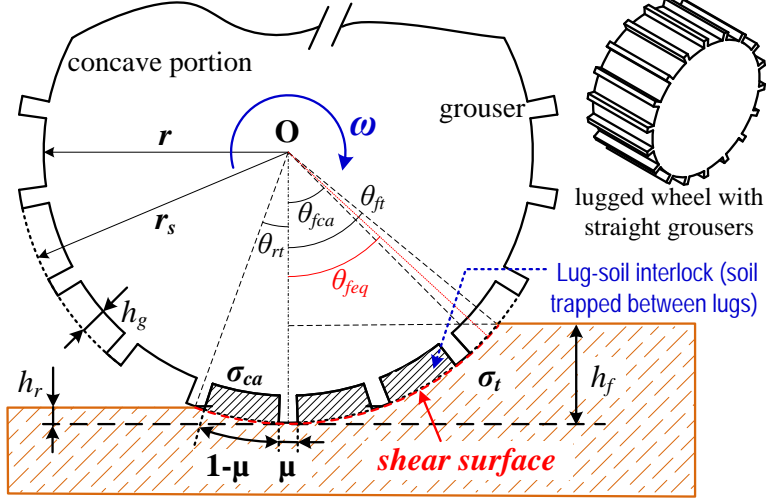


Figure 2.14 Wheel with lugs on soft soil [77]

The addition of grousers can change the location of the entry contact angle, which is important for integrating stress along the wheel-soil interface. If r_s is the radius of the wheel including the lug height, then the entry contact angles of the grouser tip and the concave portion, θ_{ft} and θ_{fca} , can be determined geometrically:

$$\begin{aligned}\theta_{ft} &= \cos^{-1}\left(\frac{(1-h_f)}{r_s}\right) = \cos^{-1}\left(\frac{(1-h_f)}{r+h_g}\right) \\ \theta_{fca} &= \begin{cases} \cos^{-1}\left(\frac{(r_s-h_f)}{r}\right) & h_f > h_g \\ 0 & \text{otherwise} \end{cases}\end{aligned}\quad (2.14)$$

We assume that the normal stress along the wheel-soil interface is the average of the normal stresses at the lug tip portion and the concave portion [81]. We denote this average as the equivalent normal stress σ_e , which can be determined as:

$$\sigma_e(\theta) = \begin{cases} \mu\sigma_t(\theta) + (1-\mu)\sigma_{ca}(\theta) & \theta_r \leq \theta \leq \theta_{fca} \\ \mu\sigma_t(\theta) & \theta_{fca} \leq \theta \leq \theta_{ft} \end{cases}\quad (2.15)$$

where σ_t and σ_{ca} are the lug tip portion and concave portion normal stresses, respectively.

The magnitude, tangential, and lateral component of the equivalent shear stress are equivalent to those given by Equations (2.9) and (2.10), replacing normal and shear stresses σ and τ with equivalent normal and shear stresses σ_e and τ_e . An equivalent entry contact angle θ_{feq} is introduced to simplify the derivations of the wheel-soil interaction model:

$$\theta_{f\text{eq}} = \theta_f = \mu\theta_{ft} + (1 - \mu)\theta_{fca} \quad (2.16)$$

Finally, we assume the effective exit angle of the lug tip portion equals that of the concave portion and can be calculated using Equation (2.1) or Equation (2.5).

2.4.2 Quadratic Stress Approximation

Wheel force, given by Equation (2.11), relies on the distribution of normal and tangential stress along the wheel-soil interface. The use of a quadratic approximation of the stresses along the interface allows for the creation of a closed-form analytical solution of the wheel forces and torque, previously prevented by the complexity of Bekker equations for stress. The stresses along the interface are defined using two quadratic equations, one for the front region of contact and one for the rear, as seen in Fig. 2.13. It is necessary to define the stress using two equations to reduce error since the stress is much greater at θ_m . The quadratic form of the stresses can be derived as:

$$\begin{aligned} \tilde{p}(\theta) &= a_i^p \theta^2 + b_i^p \theta + c_i^p \quad ('\theta_i \leq \theta \leq " \theta_i) \\ \text{with } \begin{bmatrix} a_i^p \\ b_i^p \\ c_i^p \end{bmatrix} &= \begin{bmatrix} \theta_m^2 & \theta_m & 1 \\ \theta_{im}^2 & \theta_{im} & 1 \\ \theta_i^2 & \theta_i & 1 \end{bmatrix}^{-1} \begin{bmatrix} p_m \\ p_{im} \\ p_i \end{bmatrix} \quad (2.17) \\ \left(\begin{array}{lll} i = f, r & p = \sigma_e, \tau_e, \tau_{et}, \tau_{el} \\ ' \theta_r = \theta_r & " \theta_r = ' \theta_f = \theta_m & " \theta_f = \theta_f \end{array} \right) \end{aligned}$$

where the subscript i indicates the front or rear region, while the superscript p indicates the stress type. The front medium angle θ_{fm} and the rear medium angle θ_{rm} are midway between the front (or rear) contact angles (θ_f and θ_r) and θ_m as shown in Figure 2.13. Substituting the quadratic approximation stresses into Equation (2.11) creates closed-form expressions for force and torque:

$$\tilde{F}_x = r_s b \sum_{i=f,r} \left[\begin{array}{l} \left(a_i^{\tau_{et}} (\theta^2 - 2) - 2a_i^{\sigma_e} \theta + b_i^{\tau_{et}} \theta - b_i^{\sigma_e} + c_i^{\tau_{et}} \right) \sin \theta + \\ \left(a_i^{\sigma_e} (\theta^2 - 2) + 2a_i^{\tau_{et}} \theta + b_i^{\sigma_e} \theta + b_i^{\tau_{et}} + c_i^{\sigma_e} \right) \cos \theta \end{array} \right]_{\theta=\theta_i}^{\theta=\theta_i}$$

$$\tilde{F}_y = -r_s b \sum_{i=f,r} \left[a_i^{\tau_{et}} \theta^3 / 3 + b_i^{\tau_{et}} \theta^2 / 2 + c_i^{\tau_{et}} \theta \right]_{\theta=\theta_i}^{\theta=\theta_i} \quad (2.18)$$

$$\tilde{F}_z = r_s b \sum_{i=f,r} \left[\begin{array}{l} \left(a_i^{\sigma_e} (\theta^2 - 2) + 2a_i^{\tau_{et}} \theta + b_i^{\sigma_e} \theta + b_i^{\tau_{et}} + c_i^{\sigma_e} \right) \sin \theta + \\ \left(-a_i^{\tau_{et}} (\theta^2 - 2) + 2a_i^{\sigma_e} \theta - b_i^{\tau_{et}} \theta + b_i^{\sigma_e} - c_i^{\tau_{et}} \right) \cos \theta \end{array} \right]_{\theta=\theta_i}^{\theta=\theta_i}$$

$$\tilde{M}_x = -r_s^2 b \sum_{i=f,r} \left[\begin{array}{l} \left(a_i^{\tau_{el}} (\theta^2 - 2) + b_i^{\tau_{el}} \theta + c_i^{\tau_{el}} \right) \sin \theta + \\ \left(2a_i^{\tau_{el}} \theta + b_i^{\tau_{el}} \right) \cos \theta \end{array} \right]_{\theta=\theta_i}^{\theta=\theta_i}$$

$$\tilde{M}_y = -r_s^2 b \sum_{i=f,r} \left[a_i^{\tau_{et}} \theta^3 / 3 + b_i^{\tau_{et}} \theta^2 / 2 + c_i^{\tau_{et}} \theta \right]_{\theta=\theta_i}^{\theta=\theta_i} \quad (2.19)$$

$$\tilde{M}_z = -r_s^2 b \sum_{i=f,r} \left[\begin{array}{l} \left(2a_i^{\tau_{el}} \theta + b_i^{\tau_{el}} \right) \sin \theta + \\ \left(-a_i^{\tau_{el}} (\theta^2 - 2) - b_i^{\tau_{el}} \theta - c_i^{\tau_{el}} \right) \cos \theta \end{array} \right]_{\theta=\theta_i}^{\theta=\theta_i}$$

2.4.3 Performance Evaluation and Comparison

Simulations were performed in order to evaluate the accuracy of the quadratic approximation method. Soil, wheel, and additional parameters used in the simulations are provided in Table 2.2, Table 2.3, and Table 2.4 respectively.

Table 2.2 Soil parameter values for select soils [37]

Parameter [unit]	c [kPa]	ϕ [rad]	n [-]	K [m]	k_c [kN/m ⁿ⁺¹]	k_ϕ [kN/m ⁿ⁺²]
Dry Sand	1.0	0.52	1.1	0.025	0.9	1,523.4
Sandy Loam	1.7	0.51	0.7	0.025	5.3	1,515.0
Clayey Soil	4.14	0.23	0.5	0.01	13.2	692.2

Table 2.3 Parameters for smooth wheel S and lugged wheel L

Parameter [unit]	b [m]	r [m]	h_g [m]	r_s [m]	μ [-]
Smooth wheel S	0.075	0.080	0.0	0.080	0.0
Lugged wheel L	0.075	0.080	0.005	0.085	0.1

Table 2.4 Additional parameters used for linear/quadratic comparison

Parameter [unit]	s [-]	β [$^{\circ}$]	θ_f [$^{\circ}$]	θ_m [$^{\circ}$]	θ_r [$^{\circ}$]
Lugged wheel L	[0.1, 0.8]	[0, 36]	[20, 50]	$\theta_f/2$	0

In addition to the quadratic approximation method, a linear approximation method similar to reference [37] mentioned previously is provided for comparison. The normal and shear stress distributions along the wheel-soil interface, shown previously in Fig 2.13, can be expressed as:

$$\hat{p}(\theta) = \begin{cases} \frac{\theta_f - \theta}{\theta_f - \theta_m} p_m = \frac{-p_m}{\theta_f - \theta_m} \theta + \frac{\theta_f p_m}{\theta_f - \theta_m} & (\theta_m \leq \theta \leq \theta_f) \\ \frac{\theta - \theta_r}{\theta_m - \theta_r} p_m + p_r = \frac{p_m}{\theta_m - \theta_r} \theta - \frac{\theta_r p_m}{\theta_m - \theta_r} + p_r & (\theta_r \leq \theta \leq \theta_m) \end{cases} \quad (2.20)$$

$(p = \sigma_e, \tau_e, \tau_{et}, \tau_{el})$

Figure 2.15 shows the errors of the linear and quadratic approximation methods compared to the original nonlinear Bekker model for entry contact angle θ_f equal to 30° , with various slip ratios and slip angles. The figure shows that the quadratic approximation method produces very small errors, less than about 2%. By comparison the quadratic approximation method errors are an order of magnitude smaller than those for the linear method. The variability in the error is also much smaller for the quadratic method.

Error($T_x=F_x/F_z$): $e_1=1.51\pm 0.30\%$; $e_2=0.11\pm 0.04\%$ Error($T_y=F_y/F_z$): $e_1=0.60\pm 0.51\%$; $e_2=0.04\pm 0.03\%$

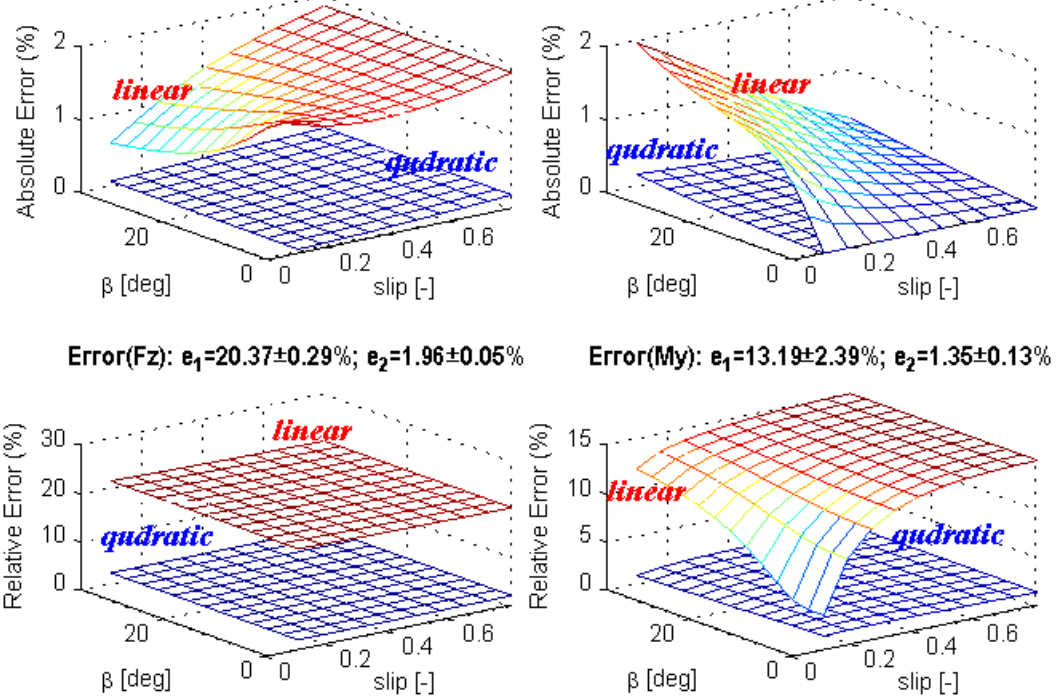


Figure 2.15 Approximation errors at varying slip angles and slip ratios for a smooth wheel on sandy loam soil [77]

The mean value and standard deviation of the errors (shown in Figure 2.15) were evaluated over a range of entry contact angles and soil types. These linear and quadratic approximation errors, calculated for both smooth and lugged wheels, are shown in Figure 2.16. The mean values of the approximation errors are given in the subplots. The notations “S1” and “S2” represent the linear and quadratic approximations of the stresses for the smooth wheel S, respectively. The notations “L1” and “L2” represent those of the lugged wheel L. Again we see that modeling error is lower by an order of magnitude when using the quadratic approximation method by comparison to the linear method.

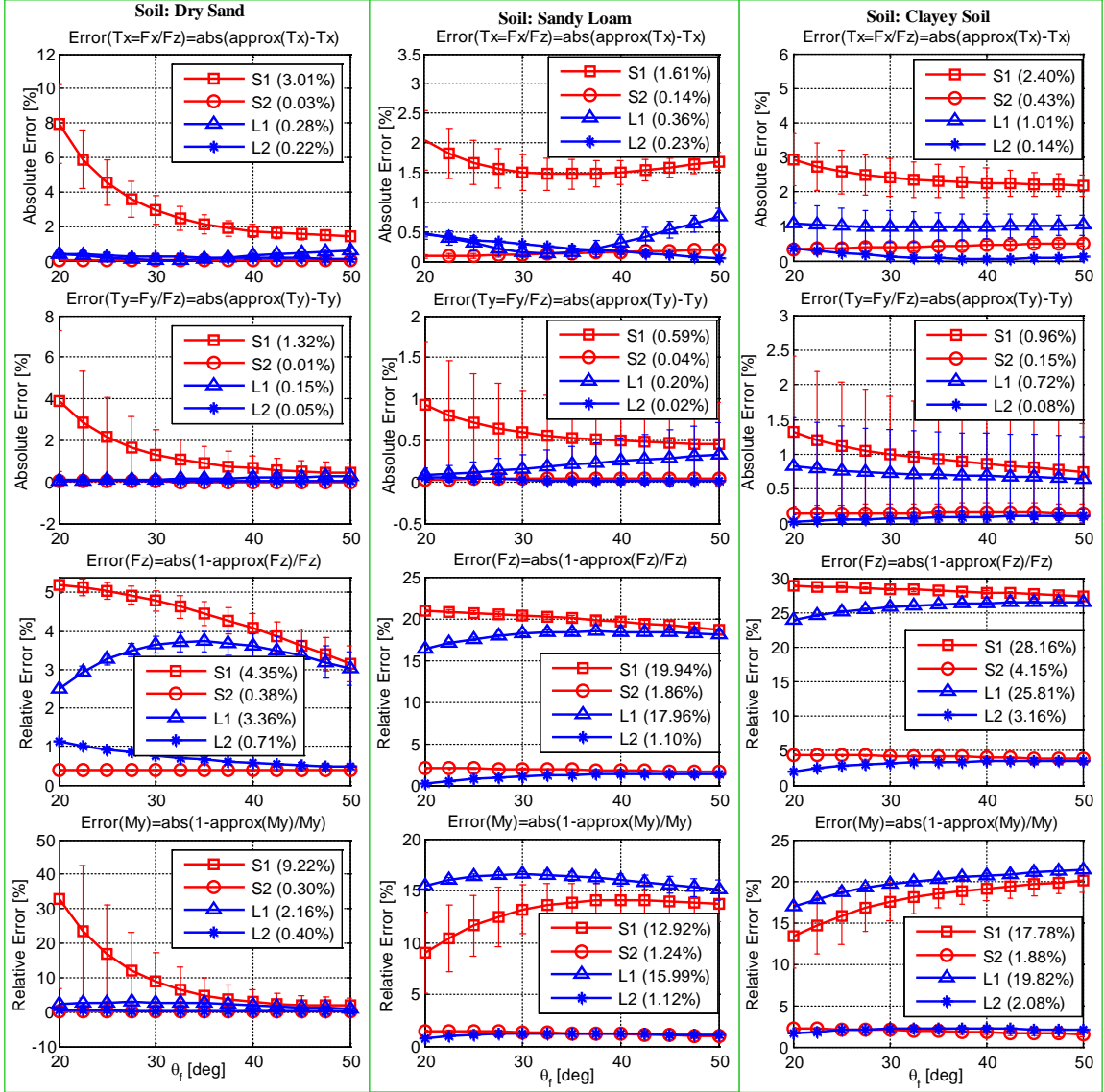


Figure 2.16 Approximation errors for smooth (S) and lugged (L) wheels using linear (1) and quadratic (2) approximation methods [77]

The quadratic approximation method has been shown to have small error compared with the original nonlinear Bekker method. When both the quadratic and the nonlinear methods were written in *ANSI C* and compiled as a *MEX* file (used in *Matlab*) the quadratic method typically required 77 μ s to solve, while the original nonlinear method required 43 ms (both computations performed on a 1.6 GHz laptop computer) [81].

2.5 Conclusions

Two methods to reduce the computation cost of Bekker method calculations were developed: the lookup table method and the quadratic approximation method. The lookup table method performs Bekker calculations offline, which are stored in lookup tables that can be interpolated as needed. The method reduces computation costs by two orders of magnitude, has a consistent computation cost by not requiring iteration, and can handle modifications to the Bekker method such as multi-pass effects. The lookup table method is poorly suited for online control applications due to the memory requirements imposed by the lookup tables, and due to the fixed nature of the lookup tables which are built for a specific set of soil parameters. The quadratic approximation method approximates the normal and shear stress distributions using a set of quadratic equations, resulting in a closed-form analytical solution. This method exhibits consistently low error with a reduction in computation costs of three orders of magnitude. The quadratic approximation method is well suited to online control applications. These methods address the computation limitations of the Bekker method and are beneficial for SUGV design and control, however they do not address the fundamental limitations of the Bekker method described in Section 1.2.1.

CHAPTER 3

Surface Roughness Modeling

One of the major differences between on-road and off-road locomotion is the level of roughness of the terrain. Roads are generally smooth, which helps reduce passenger discomfort, tire wear, and road surface wear. Unfortunately we cannot control the surface quality during off-road locomotion. Research evidence showing the influence that rough terrain can have on vehicle performance was presented in Section 1.2.2, however the effect of roughness on SUGV performance has not been scientifically studied. The drawbacks of purely theoretical and Bekker type simulation methods was detailed in Section 1.2.1, such as their limited ability to model a complex tread pattern, which make these methods poorly suited to study roughness effects. Finite element methods generally have difficulty handling large displacements, such as those which occur during large wheel slip. SUGVs frequently traverse granular soil, such as sand, which DEM is particularly well suited to model. In the following chapter the discrete element method is explained in greater detail, and 3D DEM simulations of a SUGV wheel traversing rough terrain are performed to determine whether surface roughness should be considered during SUGV design. In addition, DEM is validated by performing steady-state wheel locomotion simulations and dynamic wheel-digging simulations, and comparing to experimental test results from the literature.

3.1 Discrete Element Method

The discrete element method (DEM) was initially developed in the late 1970s to provide an alternative to continuum methods for modeling granular (particulate) materials [8]. DEM represents materials, such as soil, as a collection of individual particles which generate forces and torques upon contact with other elements. The motion of each element is determined by integrating its body forces at each simulation time step. This

method inherently has advantages when simulating sand, a granular material. Recently, researchers have used the discrete element method to model the interaction between a rover wheel and a dry granular soil (e.g. sand) in two dimensions [59] [90] [91] [62] [63] [92]. Simulations were validated by comparing with experimental time series data [59], wheel sinkage data [90], and locomotion performance at varying slope [62] [63]. Using DEM, researchers can perform studies which are difficult to conduct experimentally, such as examining the influence of gravitation force on motion resistance [92]. Wheel locomotion studies are typically performed in two dimensions in order to reduce the significant computation costs of DEM, which are largely a result of two factors: a large number of particles and a short time step. Many small particles are required to model a material; collision detection must be performed on each particle to determine the resulting interaction forces. Particle overlap must also be small relative to the size of each particle, requiring a short time step. Many decisions regarding DEM modeling are made in an effort to limit simulation time and computation resources.

The particle shape used in DEM simulations has been shown to influence the accuracy of the simulation results. Most soils are composed of irregularly shaped grains which are better represented in DEM by complex particle shapes rather than strictly spherical particles [93]. The advantage of spherical particles is they require significantly less computation time; collision detection and force directions are the simplest of any three dimensional shape. Spherical particles are unable to interlock, while free to rotate in place without disturbing other soil particles. Rolling resistance is typically incorporated to limit particle rotations and improve simulation accuracy.

The following is a description of the discrete element modeling methods later used for wheel-soil interaction simulations. All particles were modeled as spheres using the software LIGGGHTS, a version of the software LAMMPS developed at the Sandia National Laboratories [94]. The coordinate frame used in all simulations is given by the z -axis in the vertical direction, x -axis in the direction of longitudinal motion, and the y -axis aligned with the wheel axis of rotation.

The total forces acting between two particles and between one particle and a wall consist of the sum of two three-dimensional vector forces: Hertzian style friction forces $\mathbf{F}_{\text{Hertz}}$ [95] [96] [97] and cohesive forces $\mathbf{F}_{\text{cohesion}}$ [98]. These force interaction

relationships, as well as the torque relationship mentioned later, are shown in Figure 3.1. The Hertzian contact force-displacement relationship varies non-linearly with contact area, and is the sum of normal and tangential forces. Forces normal to the contact plane (along the unit vector between particles) are described by

$$F_{Hertz,n} = \sqrt{\delta \frac{R_i R_j}{R_i + R_j}} (k_n \delta n_{ij} - m_{eff} \gamma_n v_n) \quad (3.1)$$

where δ is the overlap length of the two particles, $R_{i,j}$ is the radius of each particle, k_n is the normal elastic spring constant, n_{ij} is the unit vector connecting the centers of each particle, γ_n is the normal viscoelastic damping constant, and v_n is the normal component of the relative velocity of the two particles. The variable m_{eff} is the effective mass of two particles of mass $M_{i,j}$ given by

$$m_{eff} = \frac{M_i M_j}{M_i + M_j} \quad (3.2)$$

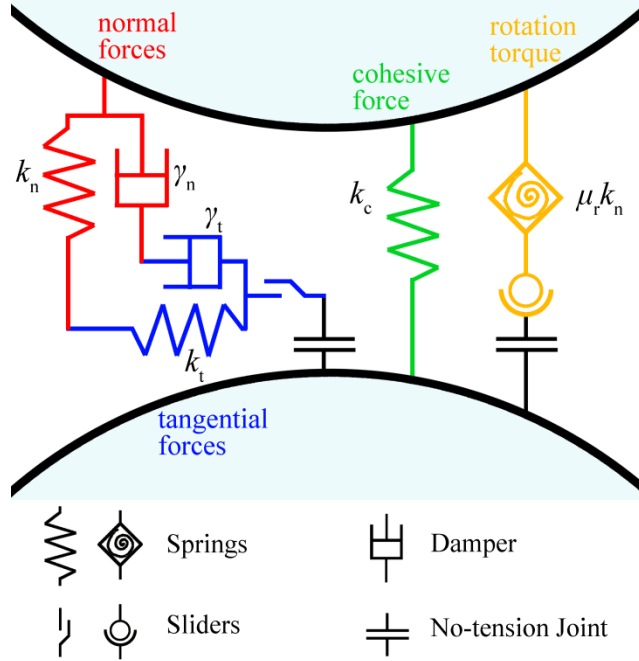


Figure 3.1 DEM contact model for particle-particle force/torque interactions [99] (after [100])

Forces tangential to the contact plane are described by

$$F_{Hertz,t} = \sqrt{\delta \frac{R_i R_j}{R_i + R_j}} (k_t \Delta s_t + m_{eff} \gamma_t v_t) \quad (3.3)$$

where k_t is the tangential elastic spring constant, Δs_t is the tangential displacement vector between the two particles for their entire contact duration, γ_t is the tangential viscoelastic

damping constant, and v_t is the tangential component of the relative velocity of the two particles. An upper limit exists for tangential forces through the Coulomb criterion given by

$$\text{if } |\mathbf{F}_t| > \mu_c |\mathbf{F}_n| \text{ then } |\mathbf{F}_t| = \mu_c |\mathbf{F}_n| \quad (3.4)$$

where μ_c is the static yield coefficient.

A simplified Johnson-Kendall-Roberts model was used to provide cohesive forces between particles. While two particles are in contact an additional normal forces acts to maintain particle contact, given by

$$\mathbf{F}_{\text{cohesion}} = -k_c A \mathbf{n}_{ij}$$

$$\text{where } A = -\frac{\pi}{4} \frac{(d_{ij} - R_i - R_j) \cdot (d_{ij} + R_i - R_j) \cdot (d_{ij} - R_i + R_j) \cdot (d_{ij} + R_i + R_j)}{d_{ij}^2} \quad (3.5)$$

where k_c is the cohesion energy density (units J/m³), A is the contact area of the two particles, and d_{ij} is the distance between the center of the two particles.

The particles used in this study are all spherical with finite mass. Particles are able to rotate given an applied torque, either as a result of the previously mentioned forces or as a result of rolling friction. Using a constant directional torque model [101] a torque contribution $\mathbf{T}_{\text{rolling}}$ can result from the relative angular velocity between two particles, given by

$$\mathbf{T}_{\text{rolling}} = \text{proj}_{t_{ij}} \left(\mu_r k_n \frac{R_i R_j}{R_i + R_j} \frac{\omega_i - \omega_j}{|\omega_i - \omega_j|} \right) \quad (3.6)$$

where $\text{proj}_{t_{ij}}$ is the projection into the shear plane, μ_r is the rolling resistance coefficient, and $\omega_{i,j}$ is the angular velocity of each particle.

3.2 Simulation Preparation

Before a simulation can be performed it must first be prepared. The software used to perform DEM simulations does not have commands to easily prepare a wheel-soil interaction simulation. Everything in the simulation must be prepared by the user, from the simulation space to the initial location of each individual particle. Even the creation of a wheel had to be specially coded. Two of the more elaborate preparation steps, the soil packing and wheel generation, are described below.

3.2.1 Soil Packing

The soil consists of many particles, each with its own size, position, velocity, and orientation. Before a wheel-soil interaction simulation can be performed, each soil particle must first be arranged and initialized. The arrangement of soil particles, or soil packing, has been shown to have a significant impact on macroscopic soil behavior [102]. The soil packing procedure used in this study was to pour soil particles under Earth gravity, which is perhaps the most common technique used in DEM simulations [58]. Particles were first poured into a rectangular prism with 25 mm sides, until the depth of the packing was slightly larger than desired. The height of the prism was determined by the desired packing depth, and periodic horizontal boundaries were used. In real experiments the soil will undergo some compaction, which influences particle placement and internal stress held through cohesion. Measured soil parameters have been shown to be effected by the compaction state and the mode of compaction [27]. After the soil particles had initially settled, a constant vertical pressure was applied to compress the packing. After the particles had once again settled, the pressure was removed and the packing was allowed to relax. An example soil block is shown in Figure 3.2.

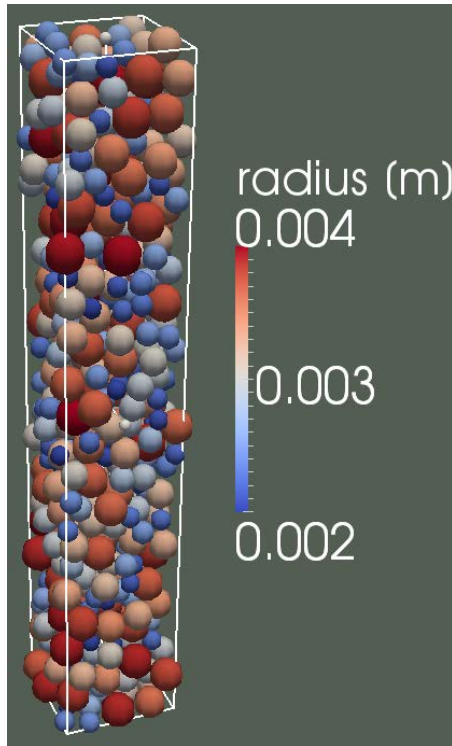


Figure 3.2 Example soil block after packing

The 25 x 25 mm soil block was repeated as necessary to create the desired horizontal simulation dimensions. By using periodic boundaries, the particles along one of the x - z boundaries perfectly align with the particles along the other x - z boundary. The same is true for the y - z boundaries. The technique of repeating a periodic block of particles to create a larger sample has been used before [58] [93]. The advantage of using this technique is a significant reduction in the amount of time required to build the soil bed for a simulation compared to building the entire soil bed through particle deposition. The surface profile of the soil was created by removing particles above the desired profile height. Additionally, a constant soil depth was maintained by removing particles below a set distance from the desired soil profile. The particles at the bottom of the soil bed and at the edges of the simulation in the x and y directions were frozen in place to act as simulation walls.

Table 3.1 DEM simulation and reference soil properties [99]

Parameter [unit]	Value	Reference
particle diameter [mm]	4 - 8	0.01 - 1.8 [103]
particle density [kg/m^3]	2,300	2,600 [58]
bulk density [kg/m^3]	1,613	1,605 - 1,660 [103] [62]
shear modulus, G [GPa]	0.024	30.0 [58]
Poisson ratio, ν [-]	0.3	0.3 [58]
cohesion [Pa]	5,000	500 - 5,000 [104] [62]
friction angle [deg]	36.9	36.5 - 37.7 [103]
compaction pressure (Pa)	5,000	-

The soil properties used in this study were chosen to model both soil types used in experimental studies performed earlier by Harbin Institute of Technology [88] and by Cornell University [103]. While both studies used a lunar soil simulant; the Harbin study used dry sand while the Cornell study used lunar regolith simulant JSC-1A. The soil properties used for this study, as well as reference values, are listed in Table 3.1. Particle size was increased greatly to reduce the number of particles required for each simulation and to increase the simulation time step. Smaller particles require smaller time steps to prevent large particle overlap. Similarly the shear modulus was reduced to allow for a

greater simulation time step, as time step is proportional to the square root of the reciprocal of the shear modulus. This practice has been shown to be reasonable for wheel-digging DEM simulations where the shear modulus used equaled 0.024 GPa [58].

Values for the DEM parameters used in Equations (3.1) through (3.6) are listed in Table 3.2. Normal and tangential stiffness values were chosen using Hertzian equations relating stiffness to shear modulus G and Poisson ratio ν : $k_n = 4G/(3(1-\nu))$, $k_t = 4G/(2-\nu)$ [95]. Damping ratios were determined through trial-and-error methods. The static yield coefficient μ_c equals the tangent of the soil friction angle [62]. The rolling resistance coefficient μ_r was tuned to limit error between experiments and simulation results. It was also assumed that no cohesion would occur between the smooth metal wheel and the soil, thus the wheel-soil k_c value equals zero.

Table 3.2 DEM particle parameters [99]

Parameter [unit]	Soil-Soil	Wheel-Soil
k_n [N/m ²]	45,710,000	45,710,000
k_t [N/m ²]	56,470,000	56,470,000
γ_n [1/m-s]	0.3	0.3
γ_t [1/m-s]	0.3	0.3
μ_c [-]	0.75	0.1
μ_r [-]	0.9	0.9
k_c [J/m ³]	5,000	0.0

3.2.2 Wheel Building

Two wheels were modeled to simulate the experiments performed by Harbin Institute of Technology and by Cornell University, labeled the Ding and MER wheels, respectively. The parameters chosen for the Ding wheel, labeled for the first author in the referred paper, and for the MER wheel, used by NASA's Mars Exploration Rovers, are provided in Table 3.3 and visualized in Figure 3.3. Some of the parameters used for the MER wheel, such as the length of the grousers, were estimated from the figures provided in the literature [58] [93] [103].

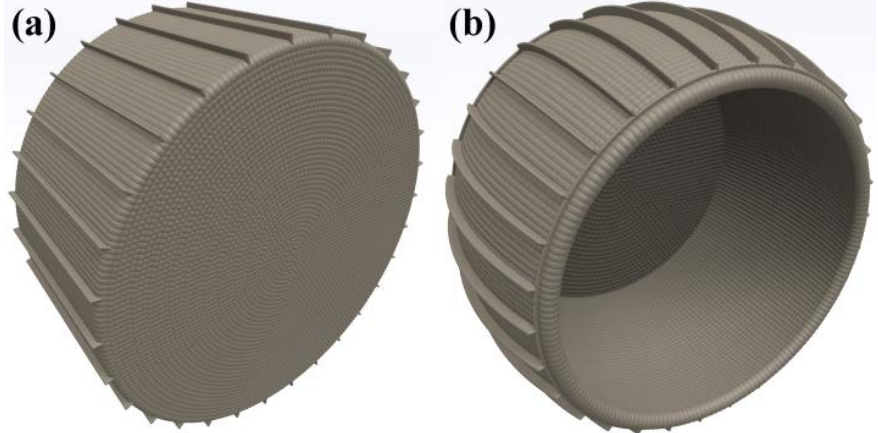


Figure 3.3 Wheel types used in simulation: (a) Ding, (b) MER [99]

Table 3.3 Wheel properties [99]

Parameter [unit]	Ding	MER
radius [m]	0.157	0.125
width [m]	0.165	0.16
particle diameter [m]	0.01	0.01
grouser particle diameter [m]	0.002	0.002
tread type	flat	concave
tread radius [m]	-	0.219
number of grousers [-]	30	30
grouser height [m]	0.005	0.00555
grouser width [m]	0.002	0.0021
number of wheel sides closed [-]	two	one
sidewall height [m]	0.0	0.0025
number of particles [-]	92,055	93,557

As mentioned before, the simulation program does not provide functions for the creation of a wheel. A program was written in *Matlab* to generate a file containing the location, size, and type of each particle comprising the wheel with specified dimensions. Each wheel consists of many spherical particles that overlap to better approximate a smooth surface. The typical distance between particles was 75% of the smaller particle's radius. The wheel particles were grouped together so that they act as a single rigid body

with no force interaction between wheel particles. In all simulations three degrees of freedom were removed so that the wheel could not move laterally or rotate out of the x - z plane. In wheel-digging simulations the wheel was also not allowed to move longitudinally.

3.3 DEM Validation

Validation is an important component of any simulation study. While all experiments studying wheel-soil interaction have challenges, rough soil testing poses additional hurdles. Usually soil is reconditioned and leveled between tests to maintain repeatability. This process becomes more difficult when a non-flat profile is modeled. Also, one of the more important factors influencing performance in rough terrain is vehicle speed. As the vehicle speed increases, the length of the test bed must also increase to allow enough time for the wheel to reach the desired longitudinal and angular velocity.

While a direct comparison to experimental data for rough soil locomotion has not yet been possible, two validation cases were considered. In the first case, steady-state values for wheel drawbar pull, sinkage, and driving torque at constant longitudinal velocity were compared over a range of wheel slip ratios. In the second case, transient values for wheel torque and sinkage were compared for a wheel-digging test.

For all simulations wheel sinkage Δz is defined by

$$\Delta z = z_{\text{profile}}(x) - (z_{\text{wheel_ctr}} - r) \quad (3.7)$$

where $z_{\text{profile}}(x)$ is the original soil profile as a function of x position of the wheel center, $z_{\text{wheel_ctr}}$ is the position of the wheel center in the z -axis, and r is the wheel radius (not including grousers). Wheel slip ratio s is given by

$$s = \frac{r\omega_y - v_x}{r\omega_y} \quad (3.8)$$

where ω_y is the angular velocity of the wheel in the y -axis and v_x is the longitudinal velocity of the wheel in the x -axis. The desired angular velocity was maintained by applying a torque to the wheel proportional to the error between desired and actual angular velocity. Except in the case of the wheel-digging simulation, longitudinal

velocity was maintained by applying a force along the x -axis proportional to the error between desired and actual longitudinal velocity. A large proportional gain was used which produced negligible angular and longitudinal error.

3.3.1 Smooth Soil Validation

The most common wheel performance test involves controlling wheel slip while traversing flat, level soil. This scenario was simulated for a small, SUGV size rigid wheel operating on a dry sand lunar simulant soil and compared to the experimental results by Harbin Institute of Technology [88]. Simulation settings are listed in Table 3.4. For each simulation the wheel was placed atop one end of a 300 x 750 x 150 mm (W x L x D) soil bed, and the system allowed to rest for 0.5 seconds. For the next 0.5 seconds the wheel slip ratio was increased linearly to the desired value by applying a force and torque to the wheel. The desired slip ratio was then maintained for an additional 15 seconds until the simulation appeared to reach steady-state, visualized in Figure 3.4. The mass density of the wheel particles was chosen to provide a constant normal load of 80 N. Since all simulations were performed under Earth gravity, the wheel had a mass of 8.155 kg to adjust for vehicle load.

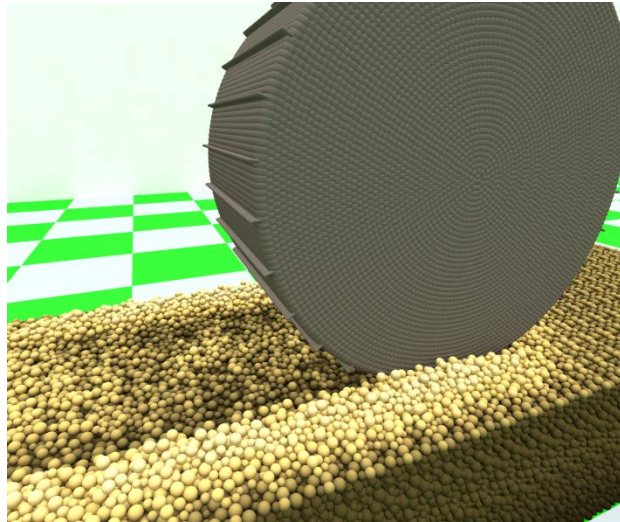


Figure 3.4 Smooth soil simulation at 0.275 slip (soil color shading indicates elevation) [99]

Drawbar pull, sinkage, and driving torque time-series data for two slip ratios are shown in Figure 3.5. Data from the last few seconds of simulation were averaged for

each slip ratio and compared to experimental data, shown in Figure 3.6. The data shows reasonable agreement between simulation and experiment, especially for higher slip ratios. Simulated sinkage values were higher at low slip ratios, while drawbar pull values were lower in comparison to experimental values. The data shows qualitative agreement to validate the DEM simulation during steady-state simulations.

Table 3.4 Smooth soil simulation settings [99]

Parameter [unit]	Value
time step [sec]	3×10^{-5}
soil width [mm]	300
soil length [mm]	750
soil depth [mm]	150
number of soil particles [-]	171,287
wheel type	Ding
wheel mass [kg]	8.155
wheel slip ratio [-]	-0.025:0.1:0.575
wheel longitudinal velocity [m/s]	0.01

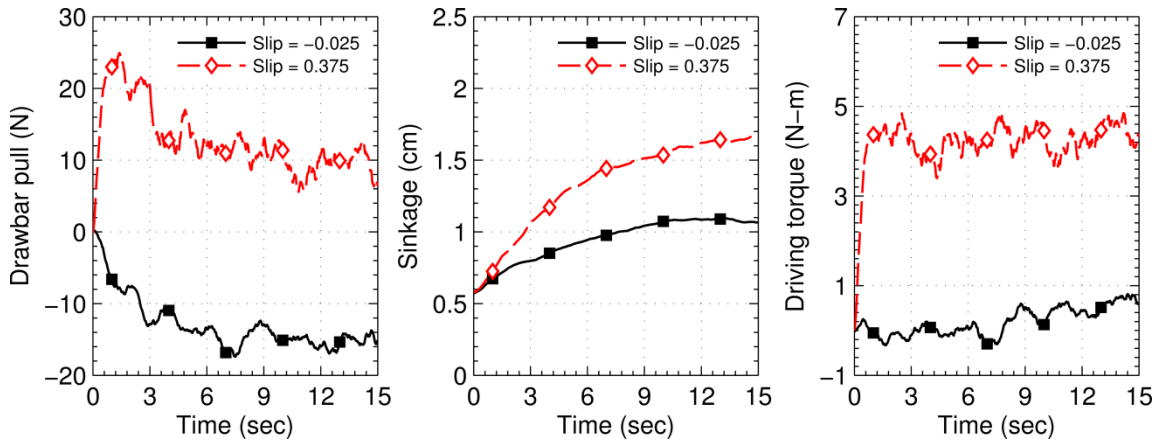


Figure 3.5 Time series drawbar pull, sinkage, and driving torque data for smooth soil validation at two slip values (-0.025, 0.375) [99]

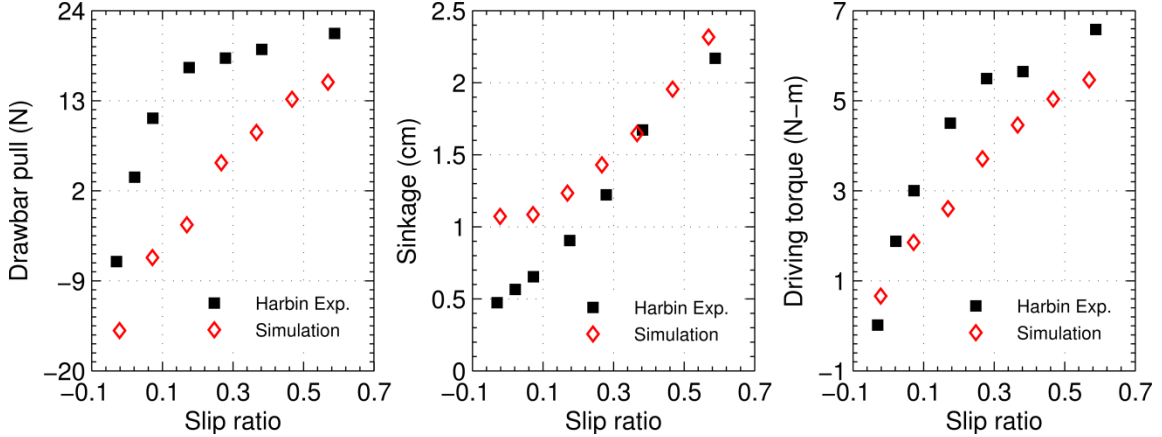


Figure 3.6 Average drawbar pull, sinkage, and driving torque values from smooth soil simulation and experiment [99] (experimental values from [88])

3.3.2 Wheel-Digging Validation

NASA used the Mars Exploration Rovers Spirit and Opportunity to perform several experiments involving digging one of its wheels into the soil in order to investigate the physical properties of Martian regolith. Cornell University conducted a similar trench-digging experiment with a MER wheel using lunar regolith simulant JSC-1A [103]. Another group simulated this experiment using 3-D DEM as a means for evaluating the use of ellipsoids and poly-ellipsoids in comparison to spherical particles [58] [93]. For this study the MER wheel was placed atop the center of a 300 x 600 x 150 mm (W x L x D) soil bed and allowed to rest for 0.5 seconds. For the next 0.5 seconds torque was applied to the wheel to increase the angular velocity linearly from 0 to 0.3 radians per second. The wheel was then rotated at 0.3 rad/s for the next ten seconds. The simulation at initialization and after 10.5 seconds is shown in Figure 3.7. During the simulation four degrees of freedom of the wheel were removed, permitting only vertical motion and angular rotation along its y-axis. In the Cornell experiment the wheel was connected to a pivoting arm 1.5 m in length to replicate the actual Mars Rover kinematics. This difference in setup is insignificant given the relatively small sinkage experienced by the wheel. The combined mass of the MER wheel and pivoting arm was 11 kg. As before, the density of the wheel particles was altered to produce the desired normal load. The simulation settings are summarized in Table 3.5.

Table 3.5 Wheel-digging simulation settings [99]

Parameter [unit]	Value
time step [sec]	3×10^{-5}
soil width [mm]	300
soil length [mm]	600
soil depth [mm]	150
number of soil particles [-]	137,027
wheel type	MER
wheel mass [kg]	11.0
wheel angular velocity [rad/s]	0.3
wheel longitudinal velocity [m/s]	0.0

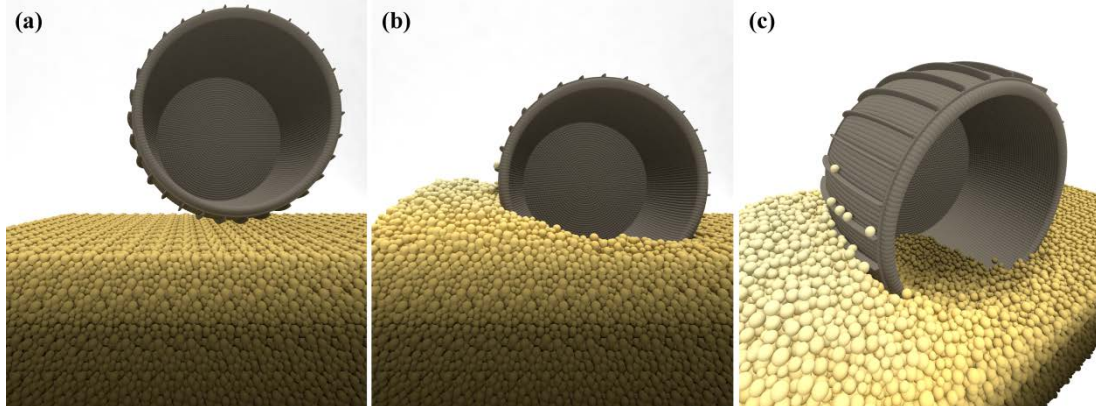


Figure 3.7 Wheel digging DEM simulation shown at initialization (a) and after 10.5 seconds (b and c) where soil color indicates elevation [99]

Results from the wheel-digging simulation are shown in Figure 3.8. As the wheel rotates clockwise soil particles are pulled to the rear of the wheel, largely as a result of the grousers. As the wheel sinks further into the soil, the driving torque necessary to maintain the desired angular velocity also increases. The simulation results show good qualitative agreement with the experimental data, especially concerning the wheel sinkage. Driving torque remains consistently lower by about 2.5 N-m throughout the simulation. The torque and sinkage results mirror the results from prior DEM

simulations of the same wheel-digging test found in the literature which used more complex ellipsoid and polyellipsoid particle shapes [58] [93]. The results from this simulation provide confidence that the DEM simulation setup is able to capture the dynamics for a transient wheel-digging experiment with reasonable quantitative and qualitative accuracy.

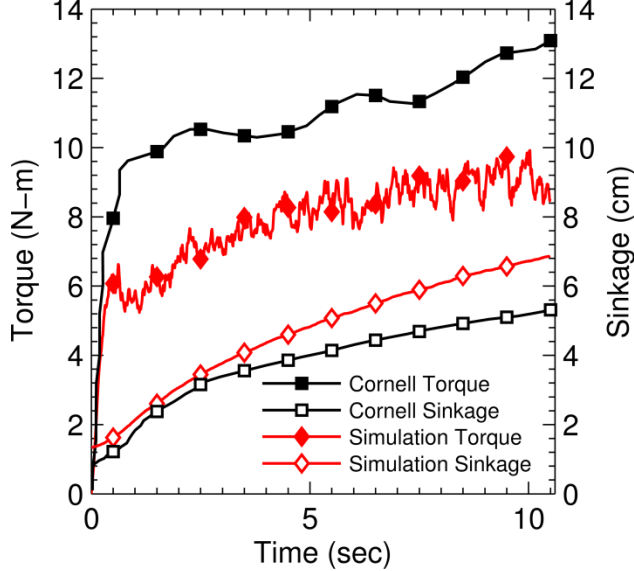


Figure 3.8 Time series torque and sinkage data from wheel digging simulation and experiment [99] (experimental values from [103])

3.3.3 Conclusions

The DEM simulation results for smooth soil wheel locomotion and for transient wheel-digging match the experimental trends, however the quantitative error was not consistently low. DEM parameter tuning using wheel simulations is problematic due to large number of data points and the significant computation costs of each simulation. The issue of DEM accuracy is addressed through parameter tuning to match soil test results and through modification of the rolling resistance term in Chapter 4.

3.4 Rough Terrain Simulations

To investigate the performance impact of traversing rough soil, 20 sinusoidal soil profiles were generated with varying amplitude and frequency. A two-dimensional sinusoidal profile was chosen to simplify the analysis of the effect of soil profile

properties on wheel performance. In addition the sinusoidal shape also allows the profile to be fully represented by a short distance, as opposed to generating the profile using a spectral density function. Limiting the simulation distance is important given the DEM computation limitations. Amplitude was varied from 6.5 to 19.5 mm, or from 5% to 15% of the maximum wheel radius including grousers. The sinusoidal frequency was varied from 16 to 64 cycles-m⁻¹ so that the profile period varied from 75% to 300% of the maximum wheel radius including grousers. Longitudinal velocity was regulated at 0.1 m/s, which is higher than many planetary rovers though less than those used on Earth. While the influence of rough terrain is expected to increase with velocity, a higher velocity was impractical given the simulation size that would be required. Flat soil was used as an experimental control to evaluate the overall impact of rough soil. Simulations were performed for 20 seconds to ensure that several soil profile periods would be traversed for all frequencies. A summary of all of the simulation settings is given in Table 3.6. A simulation with amplitude 13 mm, frequency 48 cycles/m, and 0.3 slip is visualized in Figure 3.9. The wheel is moving from left to right, compacting and displacing soil to produce a new profile behind the wheel.

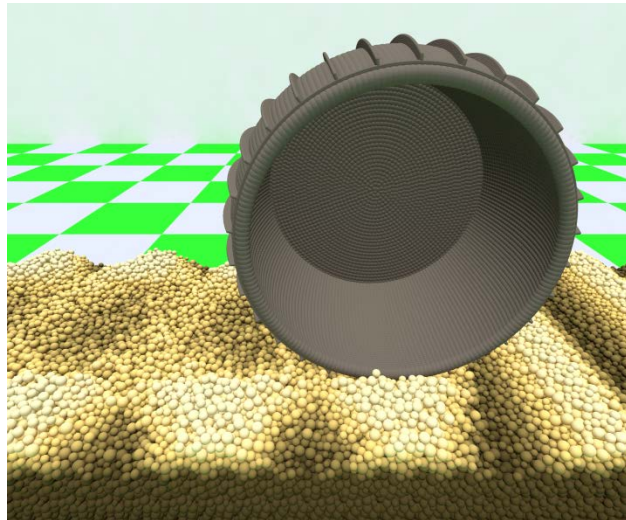


Figure 3.9 Rough soil simulation with amplitude 13 mm, frequency 48 cycles/m, and 0.3 slip (soil color shading indicates elevation) [99]

Table 3.6 Rough profile simulation settings [99]

Parameter [unit]	Value
time step [sec]	3×10^{-5}
soil width [mm]	300
soil length [mm]	2,500
soil depth [mm]	150
number of soil particles [-]	~545,000
wheel type	MER
wheel mass [kg]	8.155
wheel slip ratio [-]	0.05, 0.3, 0.55
wheel longitudinal velocity [m/s]	0.1
profile amplitude [mm]	6.5, 9.75, 13, 16.25, 19.5
profile frequency [cycles/m]	16.1, 32.2, 48.3, 64.4

Example time series data over one period of travel is shown in Figure 3.10. The data shown was filtered using a spline-type interpolation to improve data clarity. The sinusoidal profile of the rough terrain creates oscillations in the drawbar pull, sinkage, and driving torque at the wheel. The wheel can experience significant fluctuations in each of these values when traversing rough terrain.

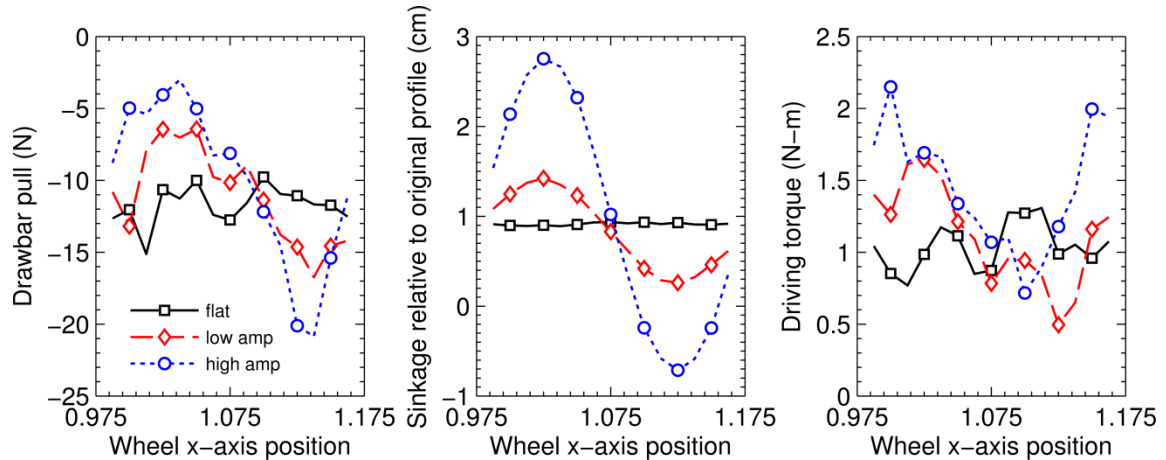


Figure 3.10 Time series drawbar pull, sinkage, and driving torque data for rough terrain with frequency 32 cycles/m and 0.05 slip [99]

3.4.1 Sinkage

One of the notable features in Figure 3.10 is that the wheel sinkage can become negative for rough terrain with high frequency oscillation. This results from the way sinkage was calculated (comparing wheel bottom position to the original soil profile) and as a result of the geometry of the rough soil profile. The solid green lines and dashed magenta lines in Figure 3.11 and Figure 3.12 display the original terrain profile and the wheel path over the terrain assuming zero soil compaction, respectively. As the frequency of the profile oscillation increases the wheel becomes less able to follow the original path. At 75% of the oscillation period in Figure 3.12 the wheel location is above the original profile, which leads to a negative sinkage value.

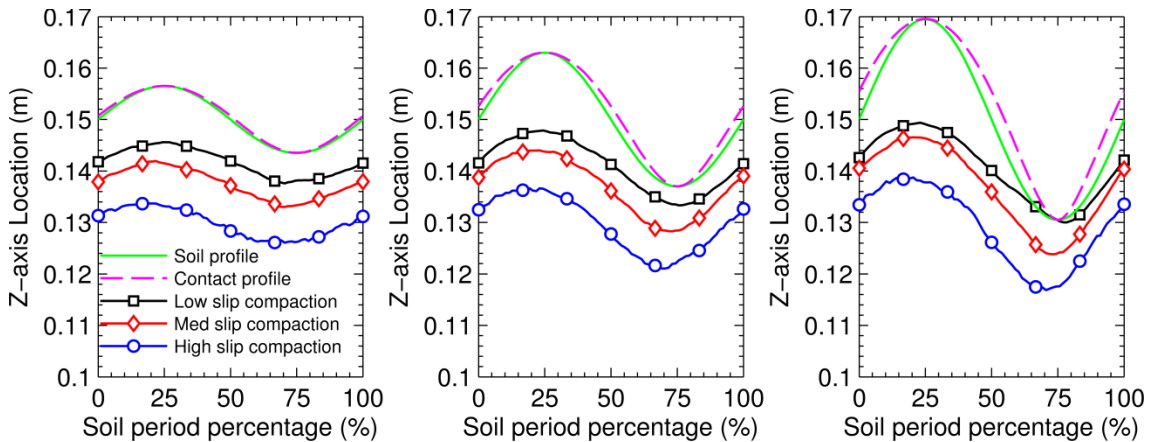


Figure 3.11 Low frequency (16 cycles/m) rough soil compaction with varying terrain amplitudes (6.5, 13, 19.5 mm) [99]

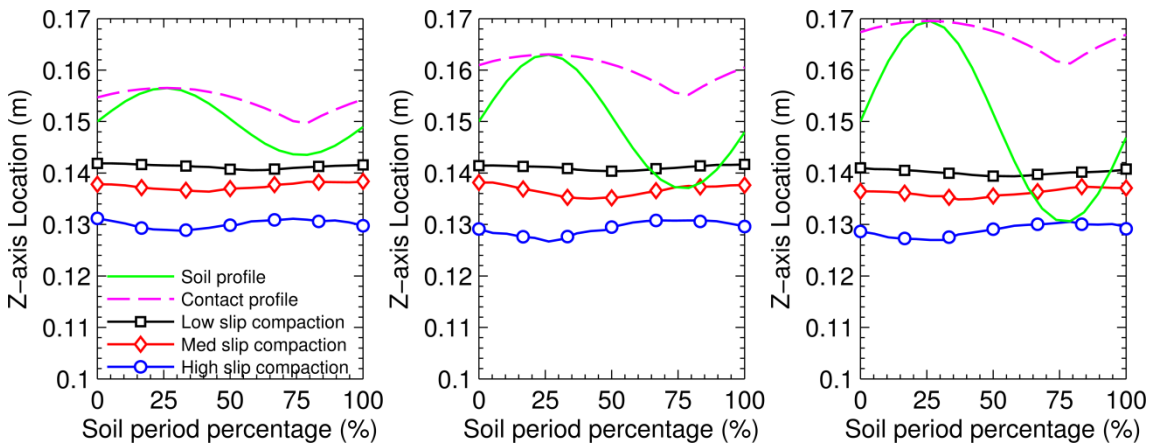


Figure 3.12 High frequency (64 cycles/m) rough soil compaction with varying terrain amplitudes (6.5, 13, 19.5 mm) [99]

In low frequency roughness the wheel moves up and down with the profile, as shown by the square, diamond, and circle marked lines in Figure 3.11. However, as the frequency increases the wheel begins to travel almost horizontally as though on flat ground, regardless of profile amplitude. While this is in part a result of the geometry of the terrain, again highlighted by the dashed magenta line, it is also a result of the constant longitudinal velocity constraint applied during the simulations. Instead of climbing over the soil, the wheel bulldozes through. The soil at the crest of one hill is often pushed into the next trough or toward the sides of the wheel, helping to level the terrain. As the frequency of oscillation increases the troughs become smaller, leading to a flatter ground.

3.4.2 Drawbar Pull

During each simulation a longitudinal force was applied to the wheel to maintain its velocity at 0.1 m/s. At low slip a positive force was applied since the wheel did not produce enough traction, while a negative force was applied at high slip to prevent positive acceleration. On flat terrain the variation of this force was significantly smaller than on rough terrain, as shown in part (a) of Figure 3.13. Drawbar pull ranges decreased as the frequency increased. This is not surprising since the wheel followed a flatter path as frequency increased. Variation increased greatly with profile amplitude; however the difference became small at 64 cycles/m. Drawbar pull variation can have a significant impact on vehicle performance. Negative drawbar pull values mean the wheel was not providing enough force to maintain its velocity. This condition greatly increases the chance that the wheel will become immobilized. Variations in tractive force can also create pitch moments for a vehicle, which may lead to vibration and increased normal loads.

Rough terrain causes not only drawbar pull variation during simulation, but also changes in average values compared to flat terrain. Average values were calculated over at least two complete profile periods so that data was not bias towards one region of the profile period. Part (b) of Figure 3.13 displays the percent difference between flat and rough terrain simulations, where blue corresponds to positive changes and red corresponds to negative changes. Drawbar pull was increased as much as 15% at 0.05 slip ratio (32 cycles/m, 19.5 mm), and decreased as much as -15% at 0.30 slip ratio (16

cycles/m, 16.25 mm) compared to flat soil. Average drawbar pull values can be useful when predicting wheel performance under a certain set of operating conditions, however the large variations shown in part (a) of Figure 3.13 must also be taken into account. A positive average drawbar pull value may not necessarily indicate that the wheel can navigate rough terrain without becoming immobilized.

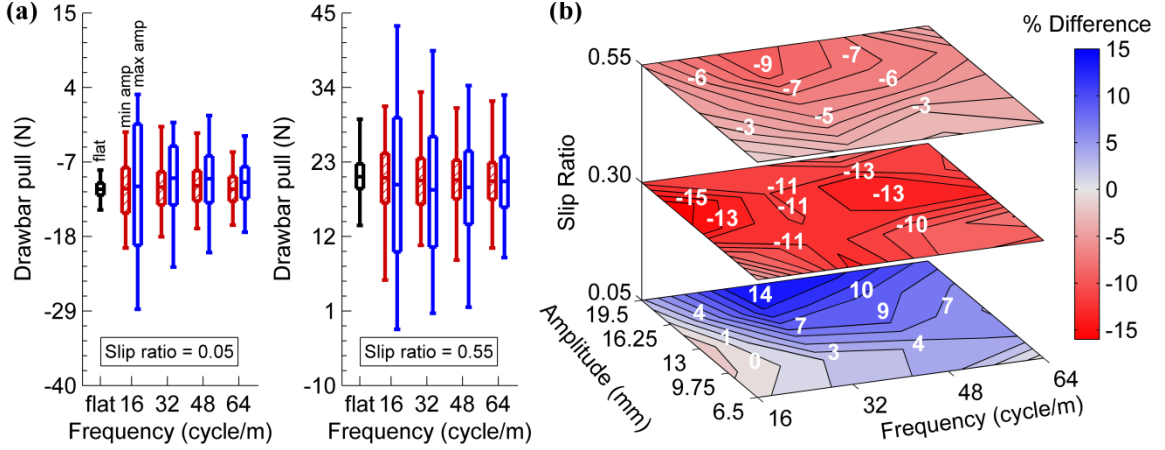


Figure 3.13 Drawbar pull values as a function of surface frequency and amplitude. (a) shows the impact of surface profile on the distribution of drawbar pull values. (b) shows the percent difference between rough and flat drawbar pull average values, where values for flat terrain equaled -11.02, 8.56, 20.84 for slip ratios 0.05, 0.30, 0.55, respectively [99]

3.4.3 Driving Torque

During each simulation a torque was applied to the wheel to maintain the angular velocity necessary for the given slip rate. At a low slip ratio the variation in driving torque was significantly larger when traversing rough terrain compared to flat, as shown in part (a) of Figure 3.14. The size of the distribution decreased as the frequency increased, and higher amplitude resulted in larger distributions. Both of these trends mirror those seen in the drawbar pull results. Like drawbar pull, variations in driving torque can have a significant impact on vehicle performance. Peak values for torque may strain the vehicle's powertrain system, or may simply be unobtainable. The powertrain may be forced to operate at decreased efficiency for components such as an electric motor, especially if they were designed around average torque values. While wheel velocity was tightly regulated during the simulations conducted for this study, vehicles in the field would most likely not be able to regulate slip as well. The vehicle may

experience large fluctuations in tractive force and wheel slip, which can have a dramatic impact on the vehicle's dynamics, efficiency, and mobility.

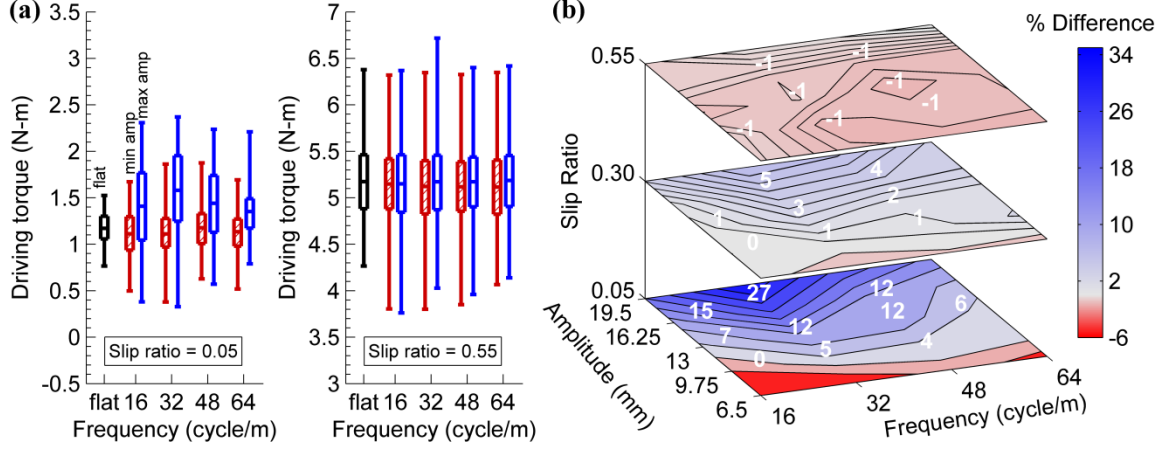


Figure 3.14 Driving torque values as a function of surface frequency and amplitude. (a) shows the impact of surface profile on the distribution of driving torque values. (b) shows the percent difference between rough and flat driving torque average values, where values for flat terrain equaled -1.17, 3.45, 5.17 for slip ratios 0.05, 0.30, 0.55, respectively [99]

Interestingly, driving torque distributions are essentially independent of roughness when operating at a high slip ratio, as shown in part (a) of Figure 3.14. When the wheel rotates at a high slip rate the lugs transport more soil particles along the circumference. This process appears to not be greatly influenced by the soil profile, and dominates the torque requirements at high slip.

Even with the significant driving torque fluctuation that can occur during a simulation, average values can be important when determining power and energy requirements over long distances. Part (b) of Figure 3.14 displays the percent difference between flat and rough terrain simulations, where blue corresponds to positive changes and red to negative changes. Driving torque was increased as much as 35% at 0.05 slip ratio (32 cycles/m, 19.5 mm), and decreased as much as 5% at 0.05 slip ratio (16 cycles/m, 6.5 mm). Average differences tended to decrease as the amplitude decreased and the slip ratio increased. In general, operating on rough terrain will require more power and energy from the vehicle's powertrain.

3.5 Conclusions

Numerical simulations using the discrete element method were conducted to evaluate the performance and mobility impacts of rough lunar terrain for a MER type wheel. Before rough terrain simulations were conducted the discrete element method was validated through comparison with two experimental tests. The first test measured drawbar pull, sinkage, and driving torque while traversing flat, level terrain at constant slip. The second test measured wheel torque and sinkage during wheel-digging. Validation of both the steady-state and dynamic simulations showed reasonable quantitative accuracy with good qualitative correlation.

The impact of rough terrain was evaluated for 20 sinusoidal soil profiles with varying frequency and amplitude. Results showed that the low longitudinal velocity combined with a fairly soft soil led to greater soil displacement over rough terrain, but did not show significant vibration. Nevertheless, wheel mobility and efficiency were decreased compared to flat, level operation. Average values for drawbar pull decreased as much as 15% while increasing as much as 35% for driving torque. More importantly all performance metrics oscillated as a result of the soil profile, producing significantly higher maximum values and lower minimum values.

The impact of rough terrain on single wheel performance was limited by the choice of soil used for the study; the lunar simulant deformed easily during wheel locomotion. At the simulated longitudinal velocity the minimal elevation changes were not enough to induce vibration. Even under the simulated conditions the rough terrain may have a greater effect on a full vehicle with vehicle pitch/roll dynamics. In the future, rough terrain experimental testing should be conducted to verify the simulation findings and to improve rough terrain modeling. Simulations should also be performed using the Bekker method to determine the benefits gained from using DEM.

CHAPTER 4

DEM Tuning and Evaluation

In the previous chapter, DEM simulations were performed to determine if surface roughness should be considered during the design stage for a SUGV. The developed DEM was studied first evaluated by comparing steady-state wheel locomotion simulations and dynamic wheel digging simulations with experimental data from the literature. Two important questions were raised by the results of the previous chapter: can DEM be tuned to improve performance accuracy, and how does DEM compare to the Bekker method. In this chapter both the Bekker method and DEM parameter were tuned to fit experimental direct shear and pressure-sinkage soil tests. Both methods were then used to simulate steady-state wheel locomotion, and evaluations were made based on accuracy and computation efficiency. In addition to the Bekker method and DEM a “dynamic Bekker” method, detailed in Section 4.1.2, is presented. The dynamic Bekker method provides a means for comparing computation costs of the Bekker method and DEM when used to perform multibody dynamics simulations.

4.1 Terramechanics Methods

The three terramechanics methods simulated in this chapter, the Bekker method, dynamic Bekker method, and the discrete element method, are each described in the following sections.

4.1.1 Bekker Method

The limitations and difficulties of purely empirical or theoretical terramechanics methods led researchers to create semi-empirical models. M.G. Bekker, a pioneer in the field during the 1950s and 1960s, created semi-empirical equations for wheel performance which are the basis for most terramechanics models today [7] [9] [10]. The

Bekker method, which encompasses all terramechanics methods derived from Bekker's original equations, is regularly used in its original or modified form. Recent examples include modification for wheel grousers [20] [77] [89] [105], identifying soil properties during vehicle operation [36] [34], and modification of the normal stress equation [26] [25]. The most significant limitations of the Bekker method can be summarized as follows. The method assumes steady-state wheel-terrain interaction, thus it ignores any dynamics. Although the method is based on the understanding of the physical nature of vehicle-terrain interaction, it remains empirical in nature, thus lacking predictive capability. These restrictions limit its applicability for transient operation and complex geometry interactions that can be modeled through multibody vehicle simulations. The details and equations of the Bekker method used in this chapter were previously described in Section 2.1.

4.1.2 Dynamic Bekker Method

The dynamic Bekker method addresses two of the limitations of the Bekker method: the ability to simulate multibody dynamics and complex soil profiles. While several variations of the dynamic Bekker method exist in the literature, the fundamental concept stays the same. The dynamic Bekker method treats the wheel as a free body with inertia, and discretizes the soil so the Bekker stress equations can be applied to each region. Researchers have used variations of the dynamic Bekker method to perform multibody simulations with [24] [28], and without [21] [76] [77] soil discretization. The following is a description of the dynamic Bekker method used in this dissertation. It should be noted that the dynamic Bekker model was developed and implemented by Daniel Melanz, who was a collaborator on a paper [106]

The model is composed of two major elements: a single rigid body representing the wheel and multiple rigid bodies representing the soil, shown in Figure 4.1. The wheel is bilaterally constrained to move at a specified linear and angular velocity to produce a desired slip ratio. The Lagrange multipliers that are produced by the solution of this constrained multibody dynamics problem provide the drawbar pull and driving torque required to propel the wheel. A vertical force is applied at the wheel hub to produce the desired normal load.

The soil is represented by a uniformly spaced set of spheres, or soil nodes, supported by nonlinear springs constrained to move only in the vertical direction. As the soil nodes come into contact with the wheel body, the nodes will be displaced. This displacement, or sinkage, is used to determine the resulting soil normal pressure. The pressure is multiplied by the area that the soil node acts on the wheel, which is the distance between the centers of the adjacent soil nodes multiplied by the wheel width. The normal force acts on the wheel in the plane of wheel-node contact. The normal pressure can be used to calculate the shear force, which is applied in the tangential plane of wheel-node contact.

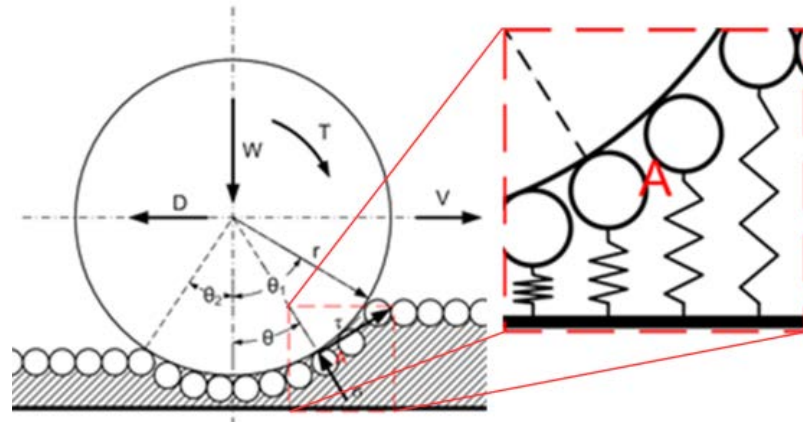


Figure 4.1 Diagram of the dynamic Bekker model. The close-up region A shows how the wheel contacts the soil nodes. [106]

These modifications to the Bekker method allow for full-vehicle multibody dynamic simulations on non-smooth soil profiles, hence the name “dynamic” Bekker method. The tool used to create this model, called Chrono [107], has been built to leverage parallel computing and specializes in simulations involving large amounts of contact and friction. Chrono is both modular and extensible, stemming from the desire to build vertical applications such as this terramechanics module.

4.1.3 Discrete Element Method

The version of the discrete element method used in this chapter has been slightly modified from the version given in the previous chapter. Modifications were made chiefly to the torque model, changing from a constant directional torque model to a

velocity-dependent elastic-plastic spring-dashpot model. Rather than cover all of the differences between the two models, the current model is discussed in detail.

In this study all particles are spherical with normal and tangential Hertzian style friction forces $\mathbf{F}_{\text{Hertz,n/t}}$ and rolling friction moment $\mathbf{T}_{\text{rolling}}$, shown in Figure 4.2. The equations for Herzian forces, including the spring and damping coefficients, are from the literature [98] [95] [96] [97]. Forces normal to the contact plane (along the unit vector between particles) are described by

$$\mathbf{F}_{\text{Hertz,n}} = k_n \delta \mathbf{n}_{ij} - \gamma_n \mathbf{v}_n \quad (3.9)$$

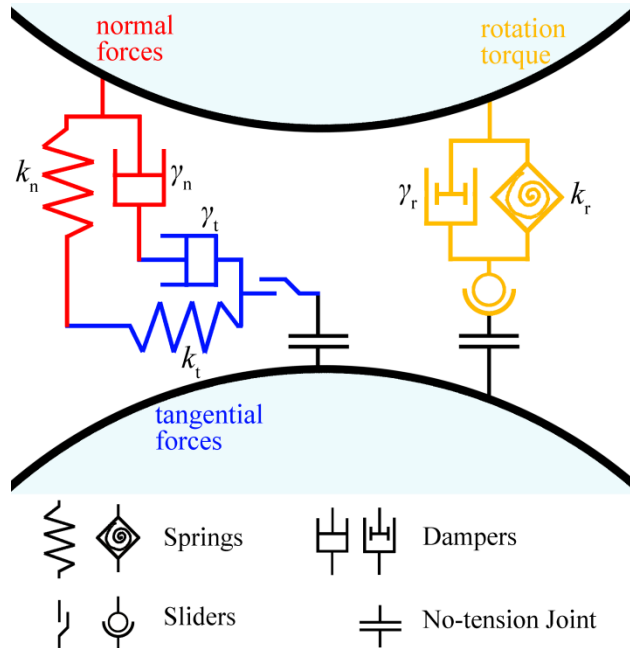


Figure 4.2 DEM contact model for particle-particle force/torque interactions (after [100]) [106]

Here the normal elastic spring coefficient k_n and viscoelastic damping coefficient γ_n are defined by

$$k_n = \frac{4}{3} Y_{\text{eff}} \sqrt{\frac{R_i R_j}{R_i + R_j}} \delta \quad (3.10)$$

$$\gamma_n = -2 \sqrt{\frac{5}{6}} \beta \sqrt{1.5 k_n \frac{M_i M_j}{M_i + M_j}}$$

The effective Young's modulus Y_{eff} and the coefficient β are defined by

$$Y_{\text{eff}} = \frac{Y_i Y_j}{Y_i(1 - \nu_j^2) + Y_j(1 - \nu_i^2)} \quad (3.11)$$

$$\beta = \frac{\ln(e)}{\sqrt{\ln^2(e) + \pi^2}}$$

where $Y_{i/j}$ is the Young's modulus of each particle, $\nu_{i/j}$ is the Poisson ratio of each particle, and e is the coefficient of restitution.

Similarly, forces tangential to the contact plane are described by

$$\mathbf{F}_t = k_t \Delta s_t - \gamma_t \mathbf{v}_t \quad (3.12)$$

Here the tangential elastic spring coefficient k_t and viscoelastic damping coefficient γ_t are defined by

$$k_t = 8G_{\text{eff}} \sqrt{\frac{R_i R_j}{R_i + R_j} \delta} \quad (3.13)$$

$$\gamma_t = -2 \sqrt{\frac{5}{6}} \beta \sqrt{k_t \frac{M_i M_j}{M_i + M_j}}$$

where G_{eff} is the effective shear modulus, defined by

$$G_{\text{eff}} = \frac{0.5 Y_i Y_j}{Y_i(2 + \nu_j)(1 - \nu_j) + Y_j(2 + \nu_i)(1 - \nu_i)} \quad (3.14)$$

An upper limit exists for tangential forces through the Coulomb criterion given by

$$\text{if } |\mathbf{F}_t| > \mu_c |\mathbf{F}_n| \text{ then } |\mathbf{F}_t| = \mu_c |\mathbf{F}_n| \quad (3.15)$$

Real soil grains have considerable angularity, causing them to interlock thereby inhibiting rotation. Many researchers have shown that when only using normal and tangential friction forces, more realistic particle shapes such as ellipsoids, poly-ellipsoids, polyhedrals, and complex shapes formed through the clumping of spheres, can better reproduce soil behavior compared to spheres [108] [109] [58]. The disadvantage of using complex shapes include increased computation time and increased program complexity. Using a rolling resistance term has been shown to provide similar results to complex particle shapes but without a significant penalty in computation speed [110] [80] [111]. All DEM particles used in this dissertation are spherical.

An elastic-plastic spring-dashpot (epsd) rolling resistance model was used in this chapter, which was shown to be a better model compared to constant directional torque

models (that was used in the previous chapter) and compared to viscous models [101]. The rolling resistance model uses a spring and damper, similar to the friction forces. The rolling resistance equations provided below are from the literature [101]. The torque contribution $\mathbf{T}_{\text{rolling}}$ acts against relative angular motion between two contacting bodies, defined by

$$\mathbf{T}_{\text{rolling}} = \min \left(\mathbf{T}_r^k + \mathbf{T}_r^\gamma, \mu_{r,\text{eff}} \frac{R_i R_j}{R_i + R_j} \mathbf{F}_n \right) \quad (3.16)$$

where $\mathbf{T}_r^{k/\gamma}$ are the stiffness/damping torque and $\mu_{r,\text{eff}}$ is the effective rolling resistance coefficient. Torque is limited by the resistance coefficient and normal force similar to tangential friction. Rolling stiffness and damping terms depend on the relative rotation vector $\Delta\theta_r$ and the relative angular velocity vector $\Delta\omega_r$, respectively, given by

$$\begin{aligned} \mathbf{T}_{r,t+\Delta t}^k &= \mathbf{T}_{r,t}^k + \Delta\mathbf{T}_r^k \\ \mathbf{T}_r^\gamma &= \gamma_r \Delta\omega_r \\ \Delta\mathbf{T}_r^k &= -k_r \Delta\theta_r \end{aligned} \quad (3.17)$$

The rolling elastic spring coefficient k_r and the rolling viscoelastic damping coefficient γ_r are defined by

$$\begin{aligned} k_r &= 2.25 k_n \left(\mu_{r,\text{eff}} \frac{R_i R_j}{R_i + R_j} \right)^2 \\ \gamma_r &= 2\sqrt{k_r I_{\text{eff}}} \end{aligned} \quad (3.18)$$

where I_{eff} is the effective moment of inertia of the particles in contact, defined by

$$I_{\text{eff}} = 1.4 \frac{M_i R_i^2 M_j R_j^2}{M_i R_i^2 + M_j R_j^2} \quad (3.19)$$

Recent research on granular soils, particularly soils with angular (less rounded) particles, has found that particle interaction forces are velocity dependent. Soil simulant SSC-2, a silty sand with fine angular grains originally intended as an analogue for Martian regolith, exhibited an increasing drag force when velocity increased from 1 to 50 mm/s [112]. In granular pile formation DEM simulations, the rolling friction coefficient was found to be dependent on the relative motion between particles [80]. In this study the effective rolling resistance coefficient is assumed to be dependent on the square of the relative velocity between particles, defined by

$$\mu_{r, \text{eff}} = \min\left(\mu_r |v_t|^2, 1.0\right) \quad (3.20)$$

where μ_r is the user-specified rolling resistance. This modification to the standard epsd rolling resistance model was necessary to accurately model the slow shear rate for direct-shear tests and the high sinkage rate for pressure-sinkage tests, using the same set of DEM parameters.

The complexity of the discrete element method is responsible for many of the method's advantages and limitations. By modeling the soil using small discrete particles DEM has the capability to analyze the micro and macro-properties of soil, and can easily handle large soil deformation and fault cracks. DEM also does not require empirical equations to handle wheel simulations, and can be expanded without modification to model interaction with other objects, such as an auger or foot [61].

The complexity of DEM limits its applicability. There is a lack of an efficient, robust method to determine the DEM parameter values necessary to produce the desired macro-mechanical properties. While computation power has greatly increased since DEM was first created, it is still necessary to model soils with significantly larger particles than in reality. Finally, DEM requires careful consideration of properties in addition to parameter values, such as particle packing structure and particle shape.

4.2 Soil Testing

Mojave Martian Simulant (MMS) [113] was used in all experiments for this chapter. MMS was characterized by performing direct shear and pressure-sinkage tests. The results from each test were used to determine the parameter values for the three terramechanics methods. The wheel performance prediction accuracy of each method can be evaluated by choosing parameter values to fit the soil tests, rather than tuning parameter values to fit wheel test results. All soil tests were performed by the Laboratory for Manufacturing and Productivity at the Massachusetts Institute of Technology, headed by Professor Karl Iagnemma and Dr. Carmine Senatore.

4.2.1 Experimental Tests

Soil shear properties greatly influence wheel performance, especially through traction generation. Direct shear tests were used to measure the shear strength properties of MMS. The shear box was approximately 60 x 60 x 60 mm (W x L x H) in size. Three normal pressures (2080, 5330, 17830 Pa) were tested for loosely-packed soil with bulk density between 1.55 and 1.6 g/cm³. The lower half of the shear box moved approximately 6.5 mm in 6 minutes, creating a shear rate of 18.0 µm/s. Two tests were performed at each normal load and averaged.

Soil normal properties also greatly influence wheel performance, especially through sinkage generation. Pressure-sinkage tests were performed using a 5 x 15 cm (W x L) in size for loosely-packed soil with bulk density between 1.55 and 1.6 g/cm³. The flat plate penetrated the soil at a rate of 10.0 mm/s to a depth of 2 cm. Fifteen tests were performed and averaged.

4.2.2 Bekker Parameter Identification

The experimental direct-shear results were used to determine the Bekker parameters c , ϕ , and K by numerically minimizing the error given by

$$\arg \min_{c,\phi,K} \sum \left[\tau(j) - (c + \sigma \tan \phi) \left(1 - \exp\left(\frac{-|j|}{K}\right) \right) \right]^2 \quad (3.21)$$

The resulting Bekker shear stress curves are shown in Figure 4.3. Error minimization was performed using the data from all normal loads so that one set of parameters was obtained.

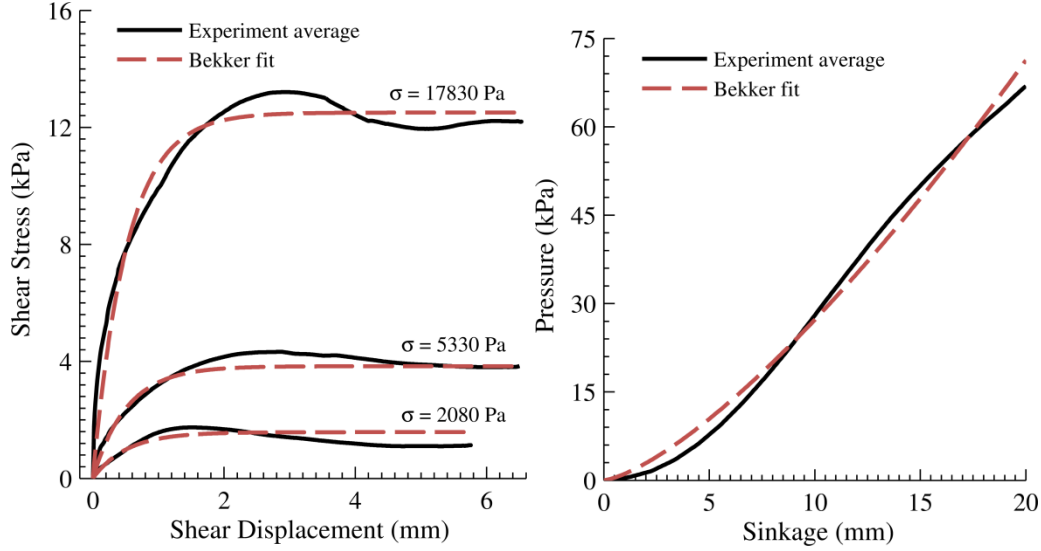


Figure 4.3 Bekker parameter fit for direct shear and pressure-sinkage tests. [106]

The experimental pressure-sinkage results were used to determine the Bekker parameters k and n by numerically minimizing the error given by

$$\arg \min_{k,n} \sum \left[\sigma(z) - k \left(\frac{z}{b_{\text{plate}}} \right)^n \right]^2 \quad (3.22)$$

The resulting Bekker pressure curves are shown in Figure 4.3. The final Bekker parameters for MMS obtained from both soil tests are shown in Table 4.1. These parameters are applicable for both the Bekker and dynamic Bekker methods. It is important to note that the pressure-sinkage parameters are sensitive to the plate size used, the maximum sinkage depth, and the penetration rate [114]. Therefore different Bekker parameter values may be obtained by using a different plate, penetration rate, or maximum sinkage depth. This is a limitation of the Bekker method.

Table 4.1 Bekker parameter values from direct-shear and pressure-sinkage curve fitting.

Parameter [unit]	Value
c [Pa]	139.280
ϕ [rad]	0.606
K [m]	5.151x10 ⁻⁴
k [Pa]	2.541x10 ⁵
n [-]	1.387

4.2.3 Discrete Element Method Tests

The parameter values for the discrete element method cannot be determined through curve fitting, as was done for the Bekker method, because the normal and shear properties cannot be described by the contact equations alone. Instead, DEM direct-shear and pressure-sinkage simulations similar to the real experiment must be performed. DEM parameters can be tuned by evaluating the simulation error.

The temporal increment, or time step, of DEM simulations must be small enough to preserve stability, yet large enough to produce reasonable computation times. The maximum allowable time step is a function of $(M_i/k_n)^{1/2}$ [115] [116] [60], placing a computation penalty on small soil particles and high Young's modulus values. After selecting an initial time step according to the function, simulations were performed at varying time step to ensure stability. In addition to the time step penalty, decreasing particle size results in an increased number of particles per unit volume, further increasing computation time. It was found that a wider range of particle radius values was beneficial to simulation accuracy, while particles too large in size decreased simulation repeatability. After evaluating numerous particle distribution ranges and shape functions, a uniform probability distribution was chosen ranging from 2.5 to 10 mm that provided a good tradeoff in computation cost, repeatability, and accuracy.

Soil particle arrangement, or packing, has a significant impact on macroscopic soil behavior [102]. The procedure used in this chapter was to pour particles under Earth gravity into a 50 x 50 mm (W x L) rectangular prism to a height of 160 mm. After the

particles settled, the soil particle density was modified to produce a bulk density of 1.6 g/cm³, roughly equal to the experimental density value. Simulations with different time steps have slightly different particle density values due to the randomness that occurs with this method. Periodic boundaries in the x and y planes were used to allow the prism to be repeated in the xy -plane, building a larger soil body. This technique was used to create the soil bodies in the pressure-sinkage and wheel locomotion tests.

Significant research has already been performed in the area of DEM parameter selection and validation, using methods such as pressure-sinkage tests [117], confined compression tests [118], direct shear tests [119] [120], angle of repose tests [111] [121] [80], and triaxial compression tests [58] [108] [110] [122]. The techniques and insights from the literature provided a basis for parameter selection in this work, however given the number of DEM parameters, configurations, and settings, thousands of soil test simulations were required to obtain reasonable accuracy. The soil parameters which were found to best reproduce the real soil behavior for both direct shear and pressure-sinkage tests are listed in Table 4.2. Mesh walls, used in direct shear and pressure-sinkage tests, were assumed to be smooth with zero friction and low restitution.

Table 4.2 DEM soil parameters and simulation settings.

Parameter [unit]	Value
particle diameter [mm]	2.5 - 10
particle density [g/cm ³]	3.072 - 3.107
bulk density [g/cm ³]	1.6
Y [Pa]	7.0x10 ⁷
ν [-]	0.35
μ_c [-] (particle, wall)	0.86, 0.0
μ_r [-](particle, wall)	6.75x10 ⁸ , 0.0
e [-](particle, wall)	0.4, 0.06

4.2.3.1 Direct Shear Test

Thousands of DEM direct shear tests were simulated during the process of parameter selection. Tests were conducted by first generating an upper and lower shear box mesh using the real shear box dimensions. Particles were then poured into the shear box to a height of 60 mm, where particle density was chosen based on the previously described particle packing method. The desired normal load was then applied to the soil using a flat plane of tightly packed particles grouped into a rigid body. The particle densities were chosen to produce the desired normal force. The inertia of the body was not an issue due to the low shear rate. After the normal pressure stabilized, the upper box and rigid body were translated at a constant shear rate of 6.6×10^{-4} m/s for a distance of 6.6 mm. Shear stress was calculated by measuring the x -plane force of the upper mesh, and dividing by the original xy -plane area. The simulation test parameters are listed in Table 4.3.

Table 4.3 DEM direct shear test settings and parameters.

Parameter [unit]	Value
shear box dimensions [mm]	60 x 60 x 60 (W x L x H)
normal load [Pa]	2,080 5,330 17,830
shear rate [mm/s]	0.66
shear displacement [mm]	6.6
number of soil particles	~640
time step [sec]	$1.5 - 3.8 \times 10^{-6}$

While the experimental shear rate was considerably slower than the simulated rate, reducing the simulated shear rate had negligible impact on shear stress curves. An example simulation is displayed in Figure 4.4 for a normal load of 17830 Pa. The figure shows the horizontal additions to the upper and lower meshes used to keep the particles within the bin.

Five direct shear tests were performed using the DEM parameter values given in Table 4.2 for time steps ranging from 1.5 to 3.8 μ s. The particle pouring method has an element of randomness, which along with the relatively large particle sizes, contributes to

variation among simulations. Simulation results, including the average and standard deviation shear stress, are shown in Figure 4.5. In the tuning process, Young's modulus was increased to achieve a suitable initial shear stress slope, while the Coulomb and rolling resistance coefficients were lowered to limit residual stress. The simulated residual shear stress is somewhat higher than experimental, however this was a compromise made to produce better pressure-sinkage results. Simulations were run on a single core of an Intel Xeon 5160 (3.0 GHz), at a rate of 40 to 20 cpu minutes per simulation second for time steps 1.5 and 3.8 μ s, respectively.

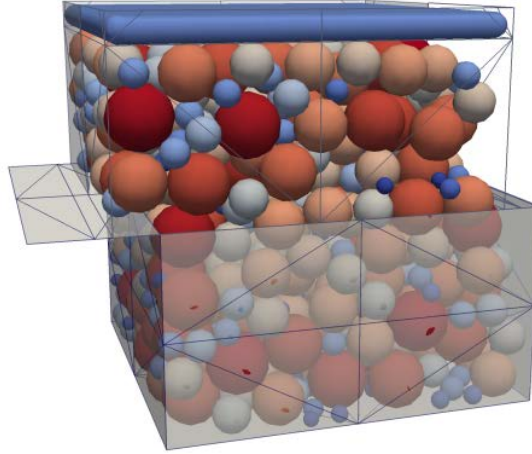


Figure 4.4 DEM simulation of direct-shear test at normal load 17830 Pa (soil shading indicates radius). [106]

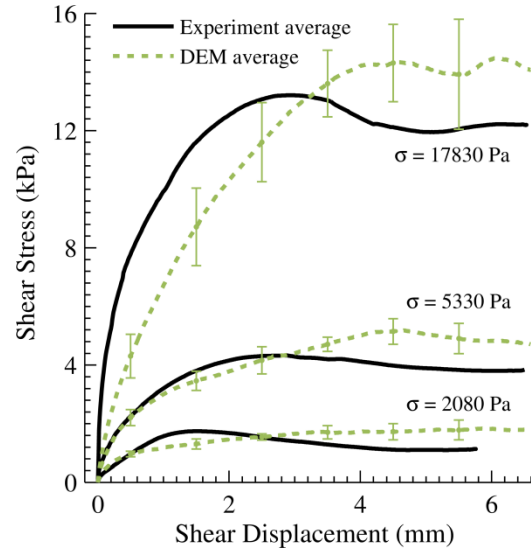


Figure 4.5 DEM direct shear average results with standard deviation bars. [106]

4.2.3.2 Pressure-Sinkage Test

Thousands of pressure-sinkage tests were simulated during the process of parameter selection. Due to the large number of simulations required, it was important to reduce computation time where possible. Reduction in the number of soil particles was accomplished by simulating a soil bin approximately three times the length and width of the pressure plate, while keeping soil depth the same as used in the experiments. Periodic boundaries were used in the *x* and *y* dimensions to help remove wall effects, better representing a larger soil bin. Computation time was also reduced by using the previously generated soil prisms, described in Section 4.2.3, to build the soil body. This step eliminated the need to perform soil packing for a large volume. The pressure plate, generated as a mesh, was moved into the soil at a fixed sinkage rate of 10 mm/s. Normal pressure was determined by dividing the *z*-plane force acting on the mesh plate by the *xy*-area of the plate. The simulation test parameters are listed in Table 4.4, with an example simulation displayed in Figure 4.6.

Table 4.4 DEM pressure-sinkage test settings and parameters.

Parameter [unit]	Value
soil bin dimensions [mm]	150 x 400 x 160 (W x L x H)
plate dimensions [mm]	50 x 130 x 10 (W x L x H)
sinkage rate [mm/s]	10.0
maximum sinkage [mm]	20.0
number of soil particles	~30,000
time step [sec]	1.5 - 3.8x10 ⁻⁶

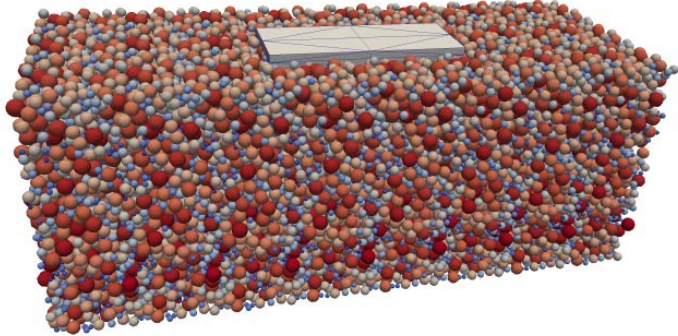


Figure 4.6 DEM simulation of pressure-sinkage test (soil shading indicates radius). [106]

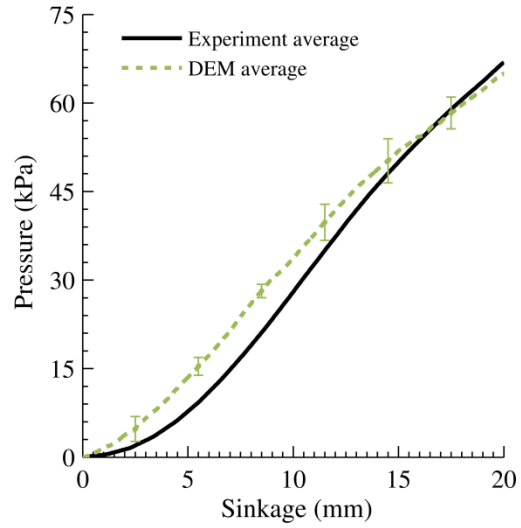


Figure 4.7 DEM pressure sinkage average results with standard deviation bars. [106]

Five pressure-sinkage tests were performed using the DEM parameter values given in Table 4.2 for time steps ranging from 1.5 to 3.8 μs . Variation among simulations is again attributed to the randomness of the pouring method used for particle packing and the relatively large particle sizes. Simulation results, including the average and standard deviation normal pressure, are shown in Figure 4.7. In the tuning process, Young's modulus, Coulomb and rolling resistance coefficients were increased to achieve suitable pressures at high沉降 values. Simulated pressure is slightly higher than experimental for low sinkage values between 2.5 and 12.5 mm, however this was a compromise made to produce better direct shear results. Simulations were run on a single core of an Intel Xeon 5160 (3.0 GHz), at a rate of 6 to 3 cpu hours per simulation second for time steps 1.5 and 3.8 μs , respectively.

4.3 Wheel Testing

Steady-state, constant slip ratio wheel tests are the most common experimental tests for evaluating terramechanics methods. A wheel is placed in the center of a rectangular soil bin, where the soil is flat and smooth. An additional mass or force is applied to the wheel to produce the desired normal load. After the wheel position stabilizes, an x -axis force and a y -axis torque are applied to the wheel to maintain the desired linear and angular velocities, respectively. Common wheel performance outputs from the test include drawbar pull (sum of forces in the x -axis), wheel driving torque, and sinkage. Tests were simulated using the three terramechanics methods and compared to experimental results.

4.3.1 Experimental Tests

Wheel experiments were performed by the Laboratory for Manufacturing and Productivity at the Massachusetts Institute of Technology, headed by Professor Karl Iagnemma and Dr. Carmine Senatore, using their single wheel test bed [123]. The test bed, shown in Figure 4.8, consists of a Lexan soil bin surrounded by an aluminum frame. A carriage slides on two rails, allowing for longitudinal (x -axis) motion of the wheel. The wheel can rotate in the y -axis while connected to a mount which translates in the vertical or z -axis. Longitudinal carriage motion is controlled by a toothed belt, while the wheel is directly driven by a DC motor. A 6-axis force torque transducer is mounted between the wheel mount and the carriage to measure drawbar pull and vertical force. A flange-to-flange reaction torque sensor is used to measure driving torque applied to the wheel. The soil used for the wheel tests was MMS, the same soil as used for direct shear and pressure-sinkage tests.

The wheel used in this study had a width of 160 mm and a radius of 130 mm. The wheel surface did not contain lugs or grousers, but was coated with MMS using glue. This guaranteed enough friction between the wheel and the soil to reduce slippage, thus forcing terrain failure to occur away from the wheel-terrain interface. An additional normal force was applied to the wheel to generate a normal load of 115 N. Experiments were conducted for 9 slip ratios with a constant angular velocity of 17 deg/s. Tests were run for a distance of 0.7 m, or until steady state was reached. The properties of the

experimental wheel tests are detailed in Table 4.5. It should be noted that the method of determining wheel sinkage was by measuring the vertical position of the wheel mount over time. This method is not precise because it does not measure at the wheel-soil interface. If the soil varies in height over the length of the test bed, the sinkage measurement will be directly influenced.

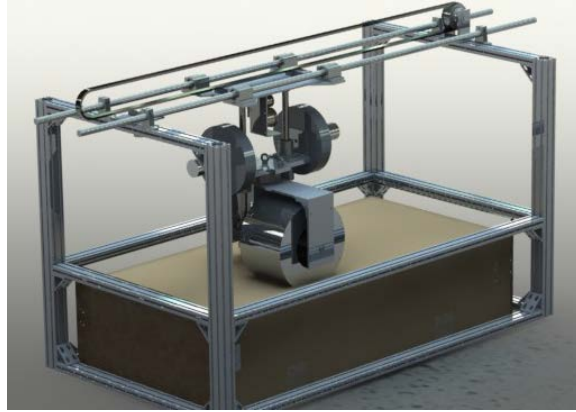


Figure 4.8 Diagram of MIT wheel test bed. [106]

Table 4.5 Experimental wheel test properties.

Parameter [unit]	Value
soil bed dimensions [mm]	600 x 1000 x 160 (W x L x H)
wheel width [mm]	160.0
wheel radius [mm]	130.0
wheel mass [kg]	3.2
normal load [N]	115.0
angular velocity [deg/s]	17.0
slip ratios [-]	-0.7, -0.5, -0.3, -0.1, 0.0, 0.1, 0.3, 0.5, 0.7

4.3.2 Simulation Settings

The following is a description of additional parameters and settings required for wheel simulations of each terramechanics method.

4.3.2.1 Bekker Method

The majority of parameter values for the Bekker method were determined through parameter fitting of the direct shear and pressure-sinkage soil tests, listed in Table 4.1. Some of the parameters, such as a_0 and a_1 from Eq. (2.5) used to determine θ_m , cannot be determined through these soil tests. These parameters can only be determined experimentally through wheel tests. The goal of this chapter is to determine the accuracy of each terramechanics method's prediction, not fit, of wheel performance. Therefore, rather than using the experimental wheel results to determine these parameters, they were assumed using coefficients from the literature [8]. Similarly, the rear contact angle θ_r was assumed equal to zero. These parameters are given in Table 4.6.

Table 4.6 Additional Bekker parameter values used for wheel simulations.

Parameter [unit]	Value
a_0 [-]	0.18
a_1 [-]	0.32
θ_r [rad]	0

The Bekker method is extremely efficient to solve, requiring about 43 ms to solve for a given slip ratio and normal load on a 1.6 GHz laptop computer [81]. It should be noted that unlike the dynamic Bekker and discrete element methods, the Bekker method solves for a steady-state relationship as opposed to a dynamic time series.

4.3.2.2 Dynamic Bekker Method

The dynamic Bekker method used the same Bekker parameters listed in Table 4.1 and Table 4.6. The added capability of the dynamic method also adds complexity to its computation. Since the dynamic method computes a time series, there is a need to select a simulation time step. A convergence analysis was performed by evaluating the steady state wheel sinkage at varying time step values, shown in Figure 4.9. A time step

between 1×10^{-3} and 1×10^{-4} was found to achieve convergence. The figure also displays the computation cost of a reduced time step.

The number of soil nodes, or node spacing, was also evaluated using a similar convergence analysis, shown in Figure 4.10. Steady state wheel sinkage converges for 300 or more nodes, corresponding to a node spacing of 3.3 mm or less. The figure also shows the computation cost of increasing the number of nodes. This cost is a result of an increased number of bodies that must be examined during collision detection.

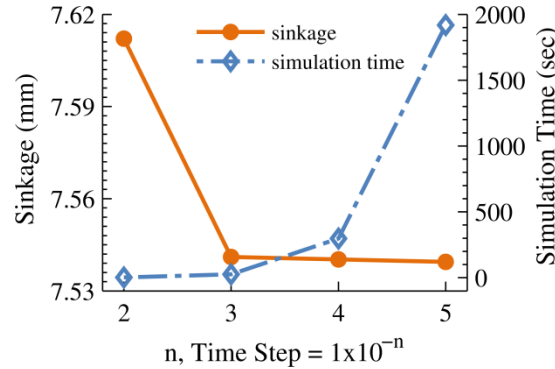


Figure 4.9 Dynamic Bekker convergence analysis for simulation time step. Simulation time is the cpu time per one second of simulation. [106]

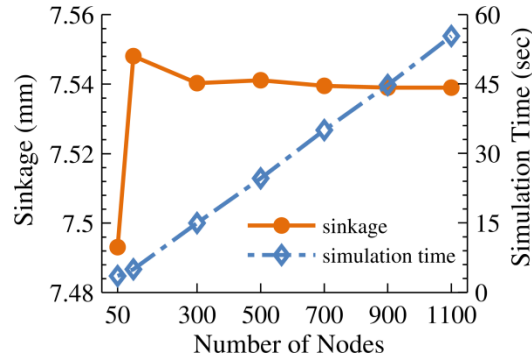


Figure 4.10 Dynamic Bekker convergence analysis for number of nodes (node spacing). Simulation time is the cpu time per one second of simulation. [106]

A rendering of the dynamic Bekker model, implemented in Chrono [107], is shown in Figure 4.11. The computation times given in Figure 4.9 and Figure 4.10 correspond to the cpu seconds per simulation second on a single core of an AMD Opteron 6274 2.2GHz processor.

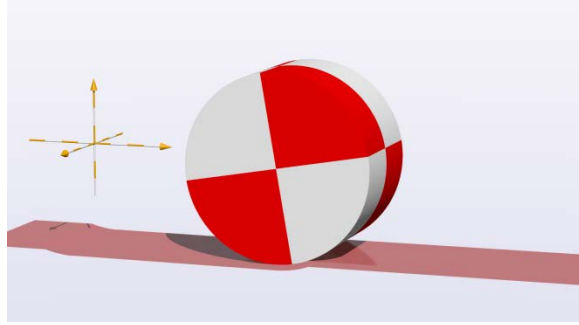


Figure 4.11 A rendering of the dynamic Bekker model. [106]

4.3.2.3 Discrete Element Method

Wheel tests were simulated using the discrete element method using the parameters found by simulating the direct shear and pressure-sinkage soil tests, shown in Table 4.2. The DEM wheel consists of many 1 cm diameter particles that overlap to approximate a smooth surface. The typical distance between particles was 75 % of the particle radius. The wheel particles were grouped together to act as a single rigid body, similar to the flat plate used in direct shear simulations. The wheel was constrained so that it could only translate in the longitudinal and vertical directions and rotate in the y -axis, similar to the experimental conditions. A rendering of a DEM wheel simulation is shown in Figure 4.12 for 50% slip ratio.

The soil bed had approximately the same dimensions as the experimental facility, requiring about 300,000 particles. The soil bed was constrained in the x and y dimensions by fixing the position of soil particles along the border, outside of the soil bed (not pictured in the figure). At the beginning of the simulation, the wheel was placed at one end of the soil bed and given 0.5 seconds to rest. Afterwards a force in the x -direction and a y -axis torque were applied for 1 second to ramp-up the longitudinal and angular velocities to their desired value. The wheel was then simulated for a travel distance of 0.7 m, or until steady state was reached. At high slip ratios the longitudinal velocity is very low, and steady state is reached before 0.7 m.

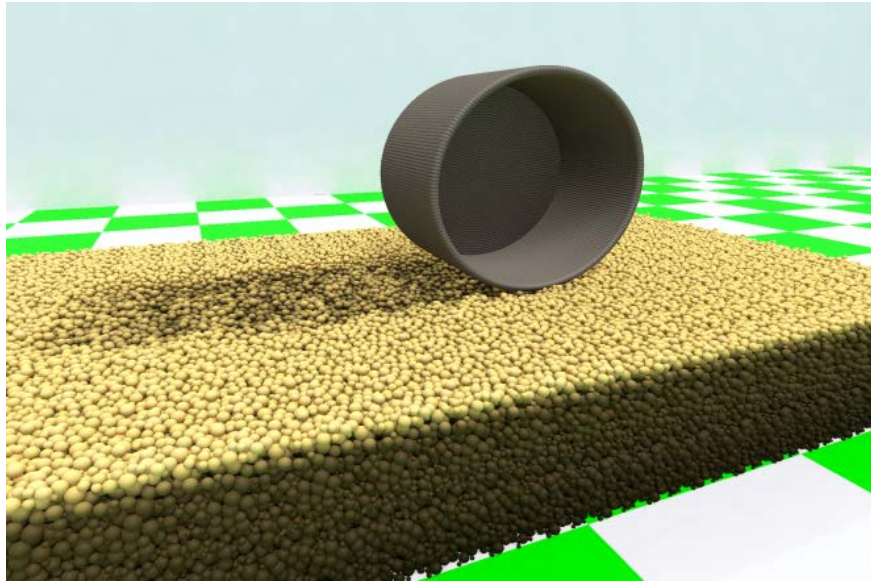


Figure 4.12 DEM wheel simulation at 50% slip (soil shading indicates elevation). [106]

Table 4.7 DEM wheel test settings and parameters.

Parameter [unit]	Value
soil bed dimensions [mm]	600 x 1,000 x 160 (W x L x H)
number of soil particles	~300,000
number of wheel particles	~12,000
time step [sec]	2.2×10^{-6}

Because the experimental wheel was covered with soil, the soil parameters were also used to describe the wheel-soil interaction. Simulations were run on 8 cores, using 4 Intel Xeon 5160 processors, on a single server blade. On average the computation rate was 8.5 hours of computation time per simulation second at a time step of 2.2 μ s. Given the time required to simulate each slip ratio (e.g. 166 hours per 19 second simulation, using 8 cores), only one simulation was performed for each slip ratio.

4.3.3 Simulation Results

Steady-state performance results were calculated by averaging the last several seconds of data, for both simulated and experimental results. Steady state results for drawbar pull, driving torque, and sinkage are compared in Figure 4.13 and Figure 4.14.

Results for drawbar pull and driving torque show similar trends. DEM provides the best fit of the experimental results, both quantitatively and qualitatively. The Bekker method has similar results as DEM for large positive and negative slip ratios, but the error is significantly larger near zero slip. The differences between the dynamic and original Bekker methods, which use essentially the same equations, can be attributed to implementation of the dynamic method and soil discretization.

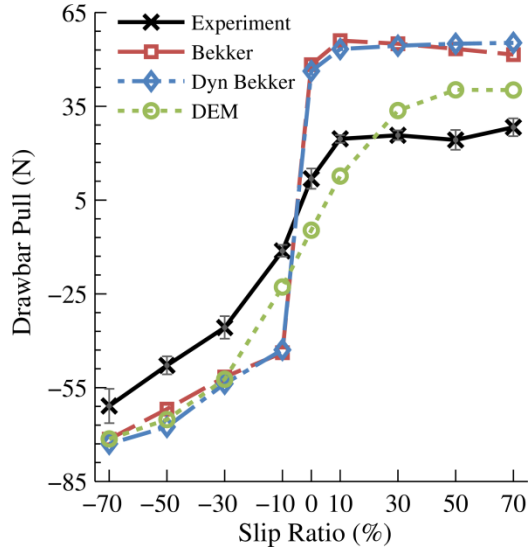


Figure 4.13 Simulated drawbar pull at steady-state compared to experimental sinkage, with experimental standard deviation bars. [106]

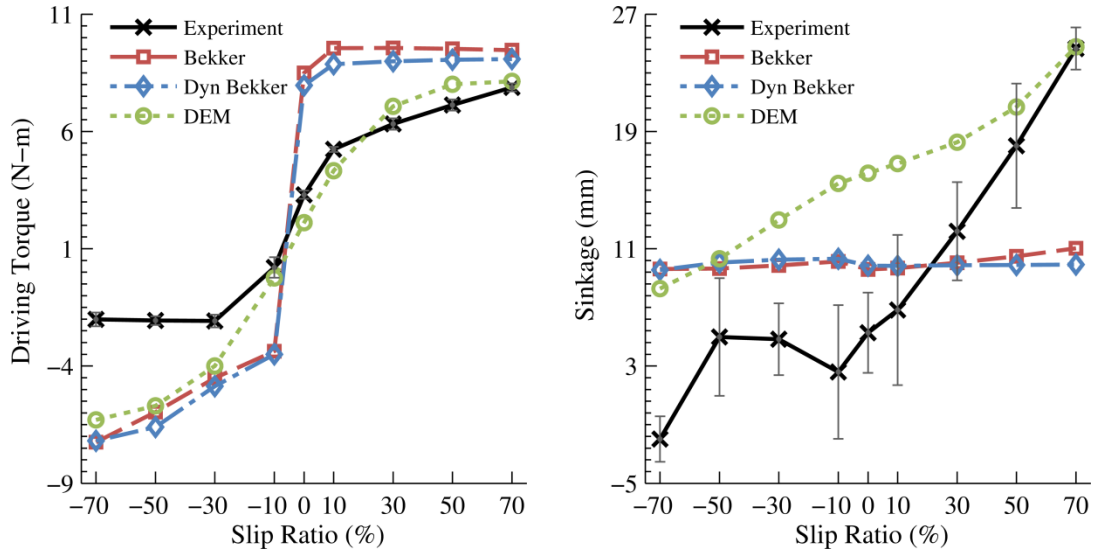


Figure 4.14 Simulated driving torque and sinkage at steady-state compared to experimental sinkage, with experimental standard deviation bars. [106]

When examining the wheel sinkage results it is important to recall the measurement uncertainty inherent in the test rig. Standard deviation bars are shown for experimental results to better illustrate this uncertainty. Given the measurement uncertainty, it is still possible to compare the three terramechanics methods using overall trends. DEM better matches the trend of the experimental results over the range of slip ratios, though the percent error for the Bekker methods can be smaller at certain slip ratios.

When considering the performance of the Bekker model the role of parameters K , a_0 , and a_1 , should be further discussed. The shear deformation parameter K , as measured through Bekker parameter tuning in this chapter, is extremely low when compared to values for similar soils found in the literature [8]. This discrepancy is not due to different intrinsic behavior of the material but it is a consequence on how the shear deformation parameter is calculated [124]. Utilizing Wong's approach for calculating K would yield a larger value, which would improve Bekker model predictions at low slip. Moreover, it should be noted that parameters a_0 and a_1 are taken from the literature and they may not be representative of the wheel-terrain configuration under investigation. Slip-sinkage behavior is sensitive to these parameters and better agreement between experimental data and the Bekker model may be obtained if a_0 and a_1 were available. However, it should be noted that these parameters can only be calculated through wheel experiments and they cannot be derived from soil tests (e.g. bevameter).

The dynamic Bekker method and DEM can be compared using time-series data in addition to steady-state values. Four seconds of drawbar pull and driving torque time-series data are shown in Figure 4.15. The experimental results show low frequency periodicity which reflects the periodic failure pattern within the soil. Other researchers have shown similar behavior for wheel tests on sandy terrain [20] [125] [88] [123]. The dynamic Bekker method models the soil as essentially a nonlinear spring without damping, and as a result oscillates at a high frequency. DEM results have a lower frequency periodicity with higher amplitude compared to experimental data, which may be a result of the relatively large soil particles used.

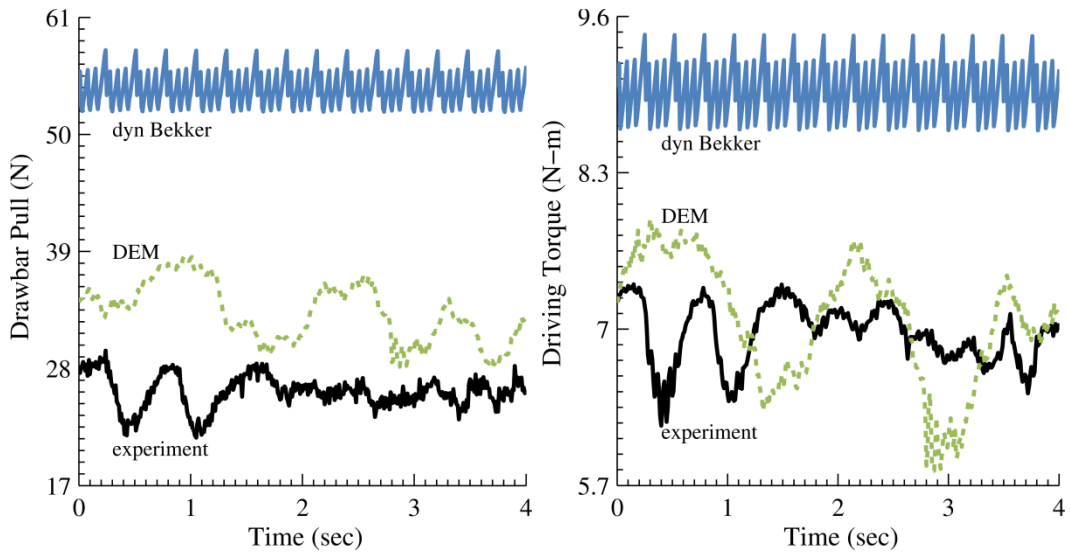


Figure 4.15 Drawbar pull and driving torque time series comparisons of experiment and dynamic terramechanics models. Time shown is a 4 second window randomly selected during steady-state operation. [106]

4.3.4 Bekker Tuned using DEM

Without wheel experimental data, it appears that Bekker methods are likely to produce significant errors, at least for small vehicles, due to their reliance on several empirical parameters. Given the computational limitations of DEM, it is desirable to use the Bekker method when possible. In situations where the capabilities of the Bekker method are sufficient, it may be possible to create a DEM simulation which could be used to tune the Bekker parameters. To better illustrate this point, and show the flexibility of the Bekker method, parameters were determined through combined least squares minimization of DEM drawbar, driving torque, and sinkage data (shown in Table 4.8).

Table 4.8 Bekker parameter values determined by fitting to DEM results.

Parameter [unit]	Value
c [Pa]	96.240
ϕ [rad]	0.606
K [m]	4.534x10 ⁻³
k [Pa]	2.305x10 ⁴
n [-]	0.418
a_0 [-]	0.09
a_1 [-]	0.90
θ_r [rad]	0

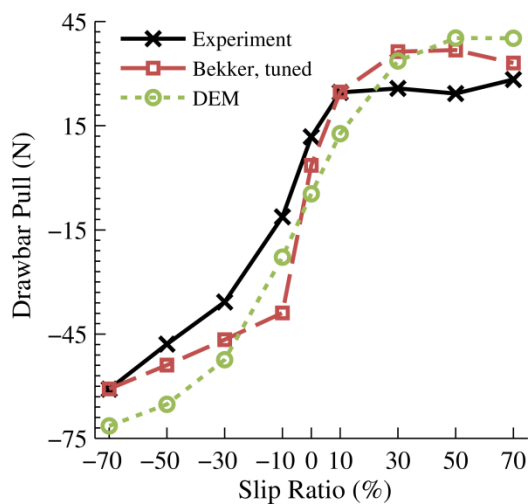


Figure 4.16 Bekker fit of DEM drawbar pull. [106]

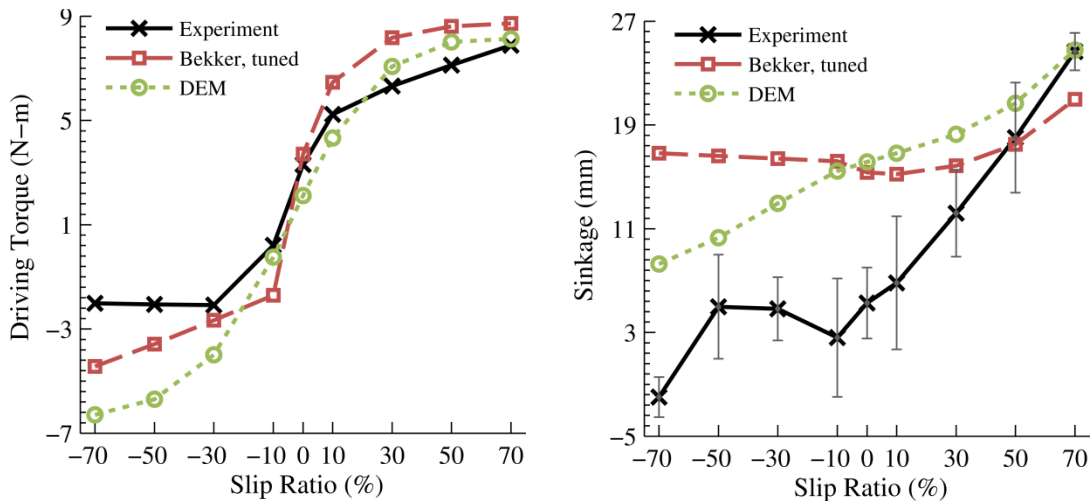


Figure 4.17 Bekker fit of DEM driving torque and sinkage. [106]

The resulting drawbar, driving torque, and sinkage curves using the DEM-tuned Bekker parameters are shown in Figure 4.16 and Figure 4.17. The figures show close agreement with the DEM results, thereby reducing the Bekker method error. Agreement is worse for negative slip values, especially regarding sinkage.

4.4 Conclusions

Three common terramechanics modeling methods were evaluated by selecting parameter values from soil tests and comparing steady state wheel performance with experimental data. Time series experimental results were also compared to the two dynamic terramechanics methods. The results from this chapter give better insight into the advantages and disadvantages of each method, while providing a direct comparison of prediction accuracy.

The Bekker method results showed why it continues to be used and developed by researchers. Parameter selection from both soil tests provided a simple, efficient method for parameter selection. With only a few additional parameters that could not be derived from the soil tests, the Bekker method generated wheel test results with reasonable qualitative agreement. If wheel data is available then many of the parameter values can be chosen to greatly reduce quantitative error. However if wheel data is already available then the need for a terramechanics model is greatly reduced.

The discrete element method produced more accurate wheel performance, both quantitatively and qualitatively, compared to both Bekker methods. This accuracy came with a large penalty in computation effort and efficiency. Significant time and effort was required to fit both direct shear and pressure-sinkage results using a single set of DEM parameters. Once parameter values were determined, each wheel simulation required 68 cpu hours per one simulation second. It should be noted that DEM has significantly greater simulation capabilities than either Bekker method. It is possible, for example, to model a more complex wheel shape digging into the soil [58]. In addition to average value steady-state agreement, DEM also showed similar time-series results. The periodic nature of the wheel-soil interaction can be useful in areas such as full vehicle multibody analysis and selection of electronic powertrain components. Further study is required to determine methods of improving the accuracy of the periodic signal.

While the Bekker method can be tuned to match DEM results for single wheel locomotion on flat, level ground, it is still uncertain how well the dynamic Bekker method can model multibody vehicle simulations and rough terrain. Comparison of DEM and the dynamic Bekker method for these conditions remains an area of future study.

CHAPTER 5

Surrogate DEM

Two terramechanics methods were described and improved upon in the previous chapters, the Bekker method and the discrete element method. Both methods have drawbacks which limit their applicability to vehicle design and control. The Bekker method, while computationally inexpensive, was considerably more inaccurate at predicting wheel performance and is not well suited to model vehicle dynamics or rough terrain locomotion. DEM is limited by its high computational resource requirements, however it provides considerable flexibility in modeling various soil types, wheel shapes, and terrain topography. The Bekker method has been refined for more than 60 years; techniques to overcome its inherent limitations are unlikely to be achieved. However, DEM continues to evolve, with the chief limitation being computation power. Recent advances have shown DEM techniques to model both saturated soil, rock fracturing, concrete, powder compaction, and more [126] [127] [128] [129] [130].

Many engineering fields rely on accurate, high-fidelity, computationally expensive simulations which hinder system design and control. A common technique is to develop a surrogate model, which can represent the expensive model but at a significantly reduced computation cost. Surrogate models have been used in a wide range of fields, such as circuit design, aerodynamic shape optimization, structural health monitoring of bridges, structural dynamic responses, multi-objective energy system optimization, air quality modeling, and lithium-ion battery modeling [131] [132] [133] [134] [135]. In this chapter a surrogate model for the discrete element method (S-DEM) is developed, which reproduces much of the capability of the original DEM model but at a significantly reduced computation cost. The goal is to develop a surrogate model that is suitable for use in vehicle design, and may also be efficient enough for use in control applications.

5.1 Literature and Inspiration

Inspiration for the development of a surrogate model for DEM was largely the result of three techniques from the literature: non-physics based computer graphics simulators, an experimental data model used to simulate legged locomotion, and a mixed empirical-FEM model. In computer graphics simulators there is a need to quickly model granular soil interactions that appear realistic. Several researchers have developed techniques to model these interactions at interactive frame rates by including only limited physics modeling [136] [137] [138]. While these models cannot be expected to accurately model the physics of wheel-terrain interaction, their realistic images and extremely fast computation speeds were an inspiration.

Most terramechanics methods only consider wheel or track locomotion, however a recent work developed a method for modeling curved legged locomotion [139]. The researchers assumed the interactions along the leg could be discretized and approximated as small flat plates. Experiments were conducted to determine the plate-soil interaction force as a function of plate heading, angle, and depth. The resulting plate force tables were used to model the locomotion of a 6-legged vehicle on granular soil. The idea that the running gear-soil interaction could be stored in a table as a function of only a few variables was inspirational.

FEM has many of the benefits of DEM, such as the ability to model soil dynamics and sub-surface soil stresses. While FEM has a lower computation cost than DEM, it is still expensive for vehicle design and prohibitive for most control applications. Recent works have shown that by assuming soil velocity (strain) of the FEM nodes at and away from the wheel-soil interface, the resulting soil stresses can be calculated extremely quickly [140] [141]. This technique was used to reproduce Bekker method results for rover wheel-soil locomotion with fast computation speeds. The idea to assume, or approximate, soil velocities as a means for reducing computation cost was inspirational.

In the literature only one example of a surrogate model for the discrete element method could be found [142]. The researchers proposed a combination of principal component analysis and surrogate-model mapping, and evaluated their technique using a case study that identified the optimal design and operating conditions of a powder mixing process. The surrogate model presented in this chapter was developed before the

discovery of this paper in the literature. The techniques for surrogate model development and application shown in this chapter and in the literature are quite different, and only bolster the argument for future surrogate DEM model development.

5.2 Surrogate DEM Overview

The Surrogate DEM (S-DEM) model must perform two functions in order to be useful: reproduce many of the key characteristics and capability of DEM, and be significantly more computationally efficient. S-DEM must be capable of performing vehicle dynamics simulations over rough soil with numerical performance similar to DEM in order to remain advantageous compared to the Bekker method. The high computation cost for DEM is largely the result of needing to perform collision detection for each soil particle, and needing a small time step to keep the simulation stable. Rather than using particle-particle interactions, such as DEM, or a nodal mesh, such as mesh-based FEM, S-DEM defines the soil using a point cloud (similar in some respects to meshless FEM). Each point simply represents the location of soil; it does not represent a free body. S-DEM can reduce computation cost by not performing particle-particle interaction computations, thus eliminating the need for collision detection while increasing the minimum time step. At this stage S-DEM is implemented for 2-dimensions only, however in concept the method can be expanded to 3D. The decision to use 2D was made to allow for faster DEM simulations and to decrease the complexity of S-DEM during development.

In order for S-DEM to retain the desired simulation capabilities, it must be able to predict the wheel-soil interaction forces/torques and predict the resulting soil dynamics. It was hypothesized that the wheel-soil interaction forces and the soil velocities could be determined independently, reducing the model complexity. Furthermore, both the wheel-soil interaction forces and the soil dynamics are assumed to be dependent upon a few key variables: position relative to the wheel, wheel state (linear and angular velocities), and soil profile height. In broad terms, S-DEM consists of two lookup tables, one for the wheel-soil interaction forces and the other for soil velocities surrounding the wheel. In order to populate the lookup tables, DEM simulations are needed which can provide

information for all conditions (wheel velocities, relative soil positions, soil profile heights) and for a given wheel and soil type.

Figure 5.1 shows an overview of the stages involved in building, implementing, and validating S-DEM. Stage (a) displays an example DEM simulation used to build the S-DEM lookup tables. The wheel moves at a constant linear and angular velocity for a long enough period of time that a wide range of soil profile data points are generated. Stage (b) illustrates post-processing of the DEM simulation data produced in the previous stage, creating both the wheel-soil interaction table and the soil velocity table. Stage (c) shows an example implementation of the S-DEM tables. The tables are used to simulate wheel locomotion, unlike the simulations used to generate the lookup tables which were at constant velocity. Stage (d) displays an example DEM simulation of wheel locomotion used to validate S-DEM. Stages (a) through (c) are described in further detail in the following subsections.

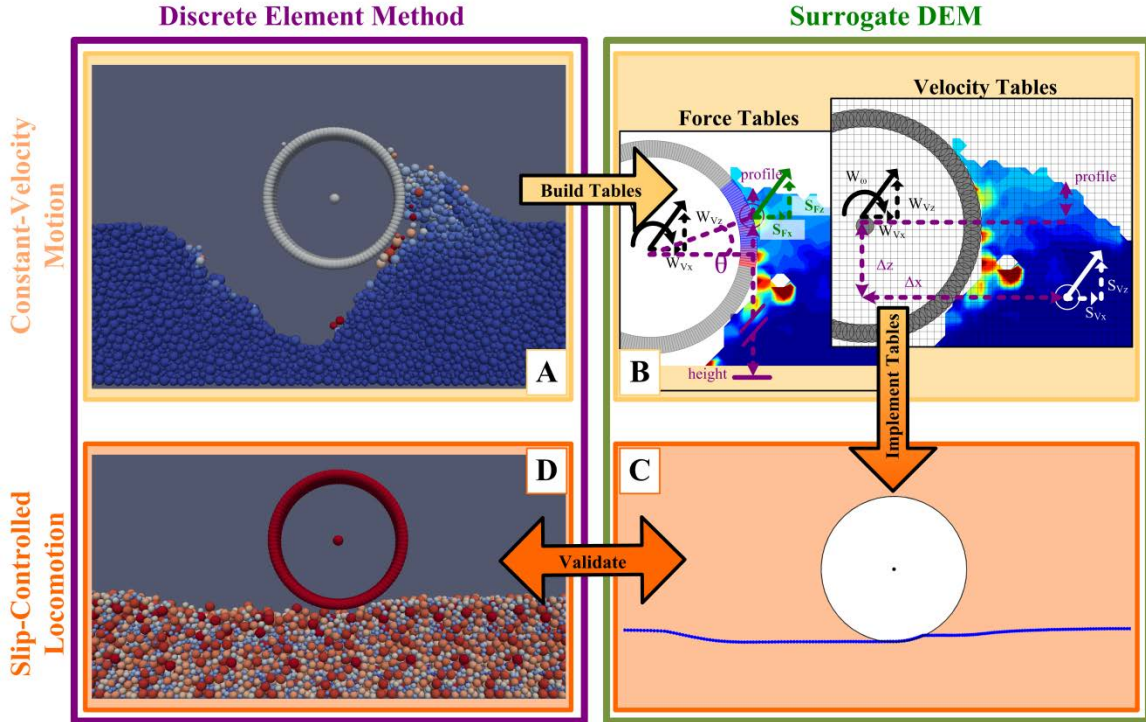


Figure 5.1 Outline of the Surrogate DEM procedure. (a) constant-velocity motion DEM simulations used to build the S-DEM tables. (b) post-processing the DEM simulations to build the wheel and soil tables. (c) implementation of the tables to run a S-DEM simulation. (d) DEM locomotion simulation used to for validation.

5.2.1 Constant-Velocity Motion Simulations

S-DEM relies upon lookup tables with several dimensions including wheel state (linear and angular velocities) and soil state (position relative to wheel, profile height). DEM simulations are required to generate the data necessary to build these lookup tables. Given a specific wheel and soil combination, DEM simulations can be run with constant wheel velocity (vertical, longitudinal, and angular). Because wheel-soil interaction forces and soil motion depend in part on the relative soil profile height, the DEM simulations must run long enough to produce a wide range of soil profiles. This means the DEM simulations must include the minimum and maximum soil profile heights, which can result in simulations where the wheel is significantly above or below the soil surface, respectively. In addition to restrictions placed on wheel position due to soil profile heights, it is necessary to simulate the wheel at its minimum distance from the soil floor. This value depends on the expected maximum sinkage during locomotion for a given soil profile.

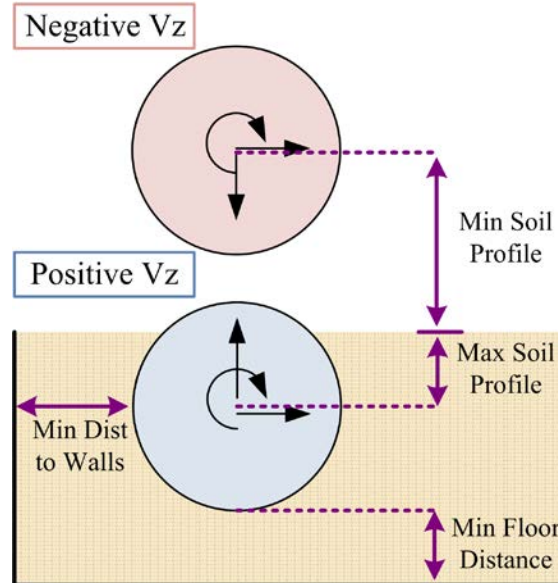


Figure 5.2 Initial wheel positioning for the constant-velocity motion DEM simulations. Initial positions for simulations with positive and negative vertical velocity are shown.

Figure 5.2 shows the initial wheel position for both positive and negative vertical velocity DEM simulations. The wheel must start at its lowest expected position for positive V_z simulations. By the end of the simulation the soil profile height surrounding the wheel will have gone from its maximum to its minimum. It is also important to keep

the wheel far enough from the simulation boundary walls to limit edge effects. A distance of 0.39 m, equal to 6 times the wheel radius, was chosen for the boundary distance as a compromise between simulation time (larger distances increases the number of soil particles) and reduction of edge effects. Table 5.1 lists the various constant-velocity simulation settings. Simulation length is a function of the vertical velocity, thus the simulations length ranges from 14.5 to 58 seconds. Soil box length is a function of the longitudinal velocity, thus the soil box length varies from 0.88 to 2.91 m. Wheel velocity values were chosen for use in S-DEM simulations corresponding to locomotion at 17 deg/s and slip ranges from -70 to 70%. All combinations of wheel velocities were simulated, resulting in a total of 108 DEM simulations. It should be noted that it is not possible using the current simulation method to perform a simulation at zero vertical velocity.

Table 5.1 Constant-velocity DEM simulation settings

Parameter	Value
longitudinal velocity [m/s]	0.0, 0.007, 0.014, 0.021, 0.028, 0.035
vertical velocity [m/s]	-0.01, -0.00625, -0.0025, 0.0025, 0.00625, 0.01
angular velocity [deg/s]	0, 15, 20
soil box height [m]	0.155
minimum floor distance [m]	0.03
minimum soil profile [m]	0.02
minimum distance to walls [m]	0.39
soil box length [m]	0.88 - 2.91
soil box width [m]	0.03
simulation length [sec]	14.5 - 58
wheel radius [m]	0.065

All DEM simulations, both constant-velocity motion and locomotion validation, are performed in quasi-2D as illustrated in Figure 5.3. As mentioned before, performing simulations in quasi-2D allows for shorter DEM computation times while reducing the complexity of S-DEM during development. Quasi-2D was achieved by performing a 3-dimensional simulation where one dimension is very narrow. This effect was created by using fixed boundary walls in the y-axis with zero friction. Simulations were performed in quasi-2D rather than 2D to minimize the effect on macro soil properties relative to 3D (e.g. void ratio, pressure-sinkage relationships).

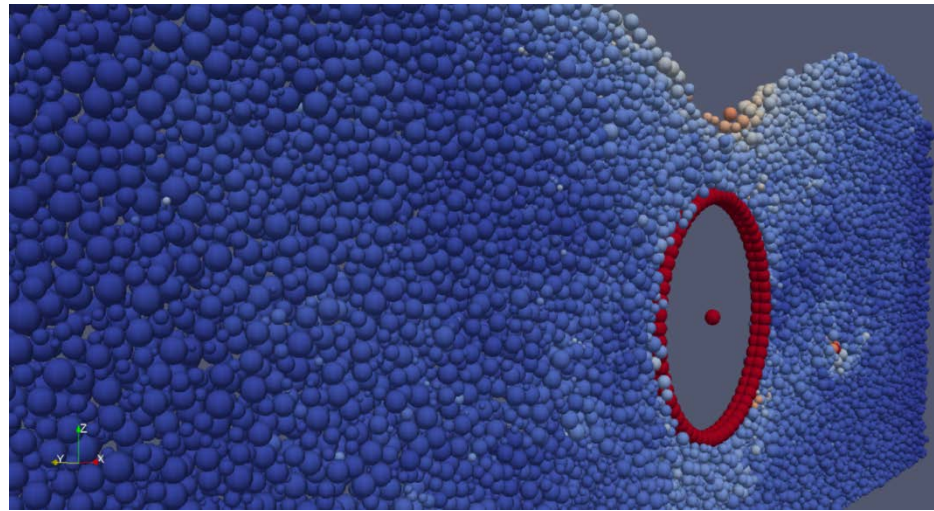


Figure 5.3 Illustration of a constant-velocity motion DEM simulation. The camera angle highlights the quasi-2d nature of the simulation.

Figure 5.4 shows example constant-velocity simulations at their beginning and end, for both positive and negative vertical velocities. These simulations were performed at a longitudinal velocity of 14 mm/s, zero angular velocity, and a vertical velocity of +/- 10 mm/s. It should be noted that the wheel does not move above the soil crest at the end of the positive vertical velocity simulation, as was intended. This behavior creates incomplete lookup table values which, like all incomplete values, were interpolated before implementation. The figure also shows possible longitudinal edge effects, e.g. the simulation wall inhibits particle motion. The constant-velocity simulations were not modified because the edge effect may also influence the wheel locomotion validation simulations, which were run using the same length as in the previous chapter. Edge

effects appear to be more pronounced for the quasi-2D simulations performed in this chapter compared to the 3D simulations performed in the previous chapters.

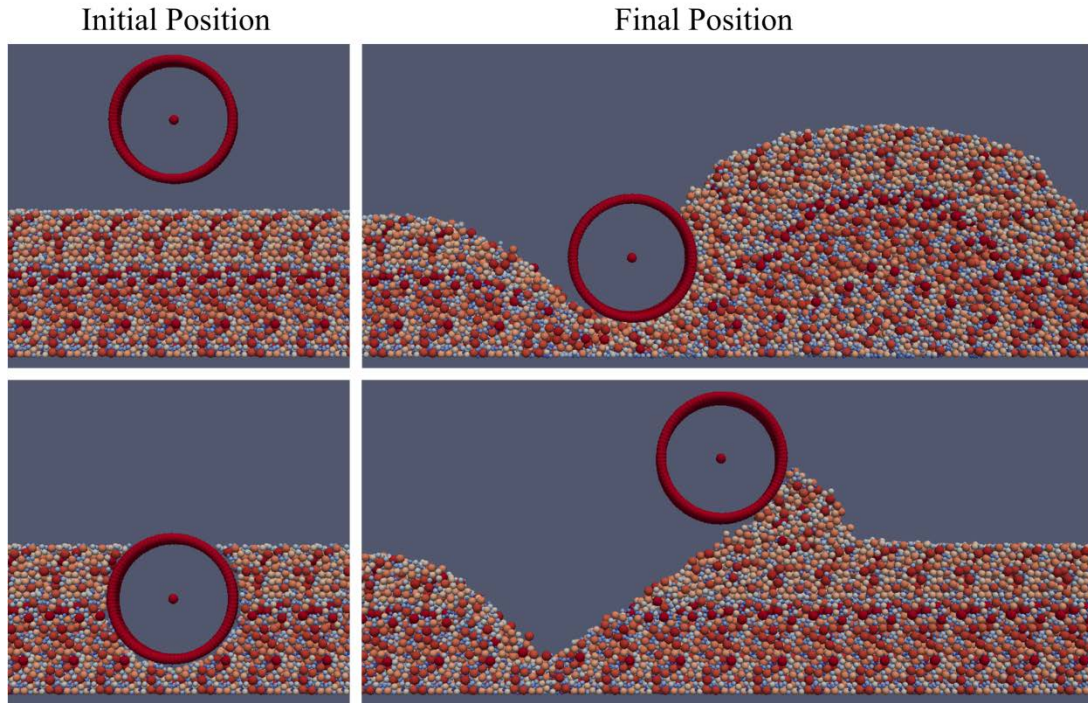


Figure 5.4 Example constant-velocity simulations with negative (top) and positive (bottom) wheel vertical velocity.

5.2.2 Soil Velocity Table Creation

Once the constant-velocity motion DEM simulations have been performed, they must be post-processed to build the necessary S-DEM tables. The process of converting from DEM simulation to soil velocity table is outlined in Figure 5.5. Stage (a) shows the original DEM simulation, where particle colors reflect the soil velocity magnitude. DEM uses a very short time step, on the order of $1e^{-6}$, while particle-particle contact can occur at a high frequency. As a result the particle forces and velocities at any one time step may not well represent the interaction behavior over time. One technique to accurately represent the behavior would be to output DEM information frequently, however this would lead to large and unmanageable data sets. Instead, particle states (soil particle positions and velocities, wheel particle positions and forces) are averaged over several time steps and output at regular intervals.

Particle states were averaged over a period corresponding to wheel travel of 0.25 mm, thus states were averaged over a greater number of time steps for slow velocity simulations. It was necessary to average over a short travel distance so that wheel forces corresponded closely to wheel-soil contact. If averaged over too long a period the input-output relationship would be lost. Outputting particle position and velocity every 0.25 mm would create extremely large data files that would require long post-processing times. Instead, averaged particle state values were output at intervals corresponding to wheel travel of 2.5 mm. While stage (a) illustrates the original DEM simulation, stage (b) illustrates averaged soil particle positions and velocities output from the DEM simulation.

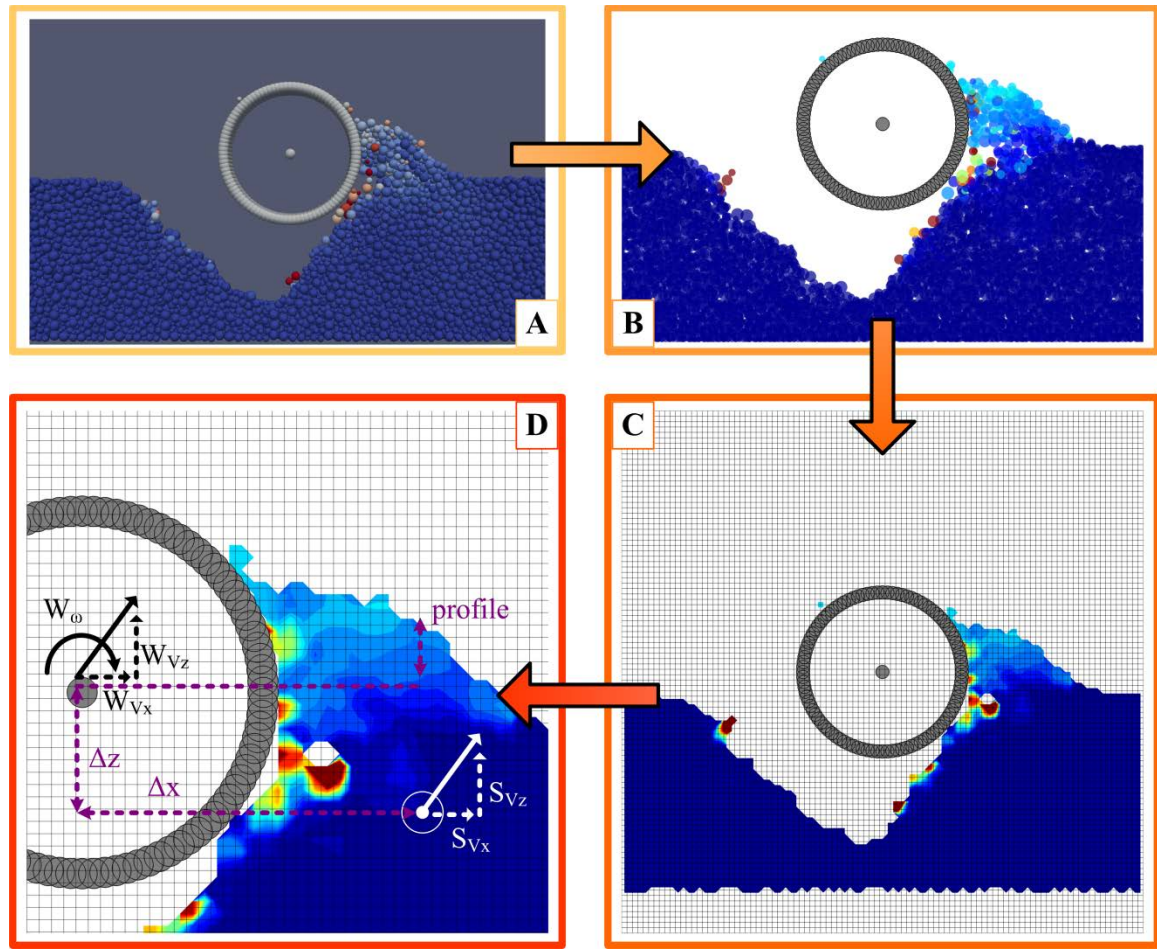


Figure 5.5 Outline of velocity mapping method. (a) constant-velocity motion DEM simulation. (b) output from DEM consists of time-averaged particle states. Particles are colored based on velocity magnitude. (c) conversion from particles to grids. (d) table velocity values (S_{Vx} , S_{Vz}) are created by determining the input values ($W\omega$, W_{Vx} , W_{Vz} , Δx , Δz , *profile*) for each table dimension.

The soil velocity lookup tables store the soil velocity (one table for x -axis velocity S_{Vx} , one table for z -axis velocity S_{Vz}) as a function of several states: wheel x -velocity W_{Vx} , wheel z -velocity W_{Vz} , wheel angular velocity $W\omega$, position relative to the center of the wheel (Δx and Δz), and the soil profile height relative to the wheel center (*profile*). In determining the key independent variables for soil velocity, relative position and wheel velocity are essential (i.e. the velocity of soil particles at locations along the wheel depends on the wheel velocity). Soil profile was chosen as an independent variable to try to capture the change in soil profile resulting from wheel motion. As a surrogate model it is important to limit the number of independent variables, and it was hypothesized that these six variables would capture the most important soil dynamics. The soil velocity tables are described analytically below:

$$\text{Soil Tables: } S_{Vx, Vz} = f(W_\omega, W_{Vx}, W_{Vz}, \Delta x, \Delta z, \text{profile}) \quad (3.23)$$

In the process of building the soil velocity lookup tables, soil velocity locations were converted from discrete particle values to regularly spaced grid values. Stage (c) of Figure 5.5 shows an overlay of the regularly spaced grid which corresponds to the Δx and Δz locations in the lookup table, where each grid is shaded according to the average velocity of the soil particles contained within its boundaries. The grid has a width and height of 0.39 m, equal to 6 times the wheel radius, with 4 mm cell spacing. While a finer cell spacing may produce greater lookup table fidelity, there is a tradeoff in computer memory. Soil profile was estimated by rounding to the largest non-empty Δz cell for each Δx . Stage (d) shows an example soil velocity data point with its input dimensions highlighted ($W\omega, W_{Vx}, W_{Vz}, \Delta x, \Delta z, \text{profile}$).

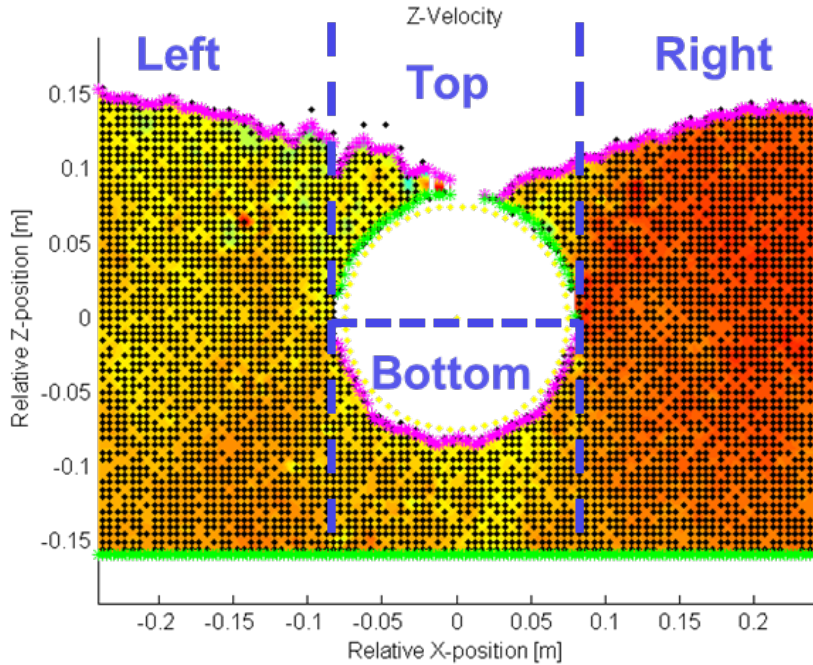


Figure 5.6 Sectioning of the soil table into regions to account for the discontinuity created by the wheel.

When the wheel sinks far enough that soil is on the top of the wheel, this creates a discontinuity in soil profile (there are two soil profiles, one above the wheel and one below). To account for this discontinuity the soil tables are segmented into four regions: Bottom, Top, Left, and Right, as illustrated in Figure 5.6. The relative position boundaries of each region are given in Table 5.2. The four regions were the minimum number required to account for the soil profile discontinuity.

Table 5.2 Relative position boundaries of the four soil table regions

Region	Δx range	Δz range
Bottom	[- radius, radius]	[- maximum, zero]
Top	[- radius, radius]	[zero, maximum]
Left	[- maximum, - radius]	[- maximum, maximum]
Right	[radius, maximum]	[- maximum, maximum]

Output from the DEM simulations does not provide data at all table locations for a variety of reasons. As an example, for positive vertical velocity simulations the initial soil profile does not reach the maximum Δz value. Given the 4 mm Δz spacing, it is also

possible that the soil profile would change rapidly enough between consecutive DEM outputs that a Δz location could be skipped. After post-processing all constant-velocity DEM simulations the soil velocity tables may be sparse. In order to allow for efficient implementation, table values were smoothed and empty data points were estimated.

5.2.3 Wheel Force Table Creation

S-DEM relies on two types of tables: soil velocity and wheel-soil force tables, both of which are generated by extracting information from constant-velocity motion DEM simulations. An overview of the process of creating wheel-soil force tables is shown in Figure 5.7, which has many similarities to the soil table creation process. The first step in the process involves performing the constant-velocity motion DEM simulations. Stage (a) displays the wheel during a simulation, rotated to highlight the quasi-2D nature of the DEM simulations used in the development of S-DEM and to show the discrete nature of particle contact during DEM simulations. Particle colors reflect the wheel-soil particle force magnitude. As was done for soil velocity output, wheel particle states (position and wheel-soil force) were averaged over several time steps and output at regular intervals. Averaging particle states over a period of wheel travel corresponding to 0.25 mm helped provide a more representative snapshot of the wheel-soil interaction forces. While stage (a) illustrates the original DEM simulation, stage (b) illustrates the averaged wheel particle positions and forces output from the DEM simulation.

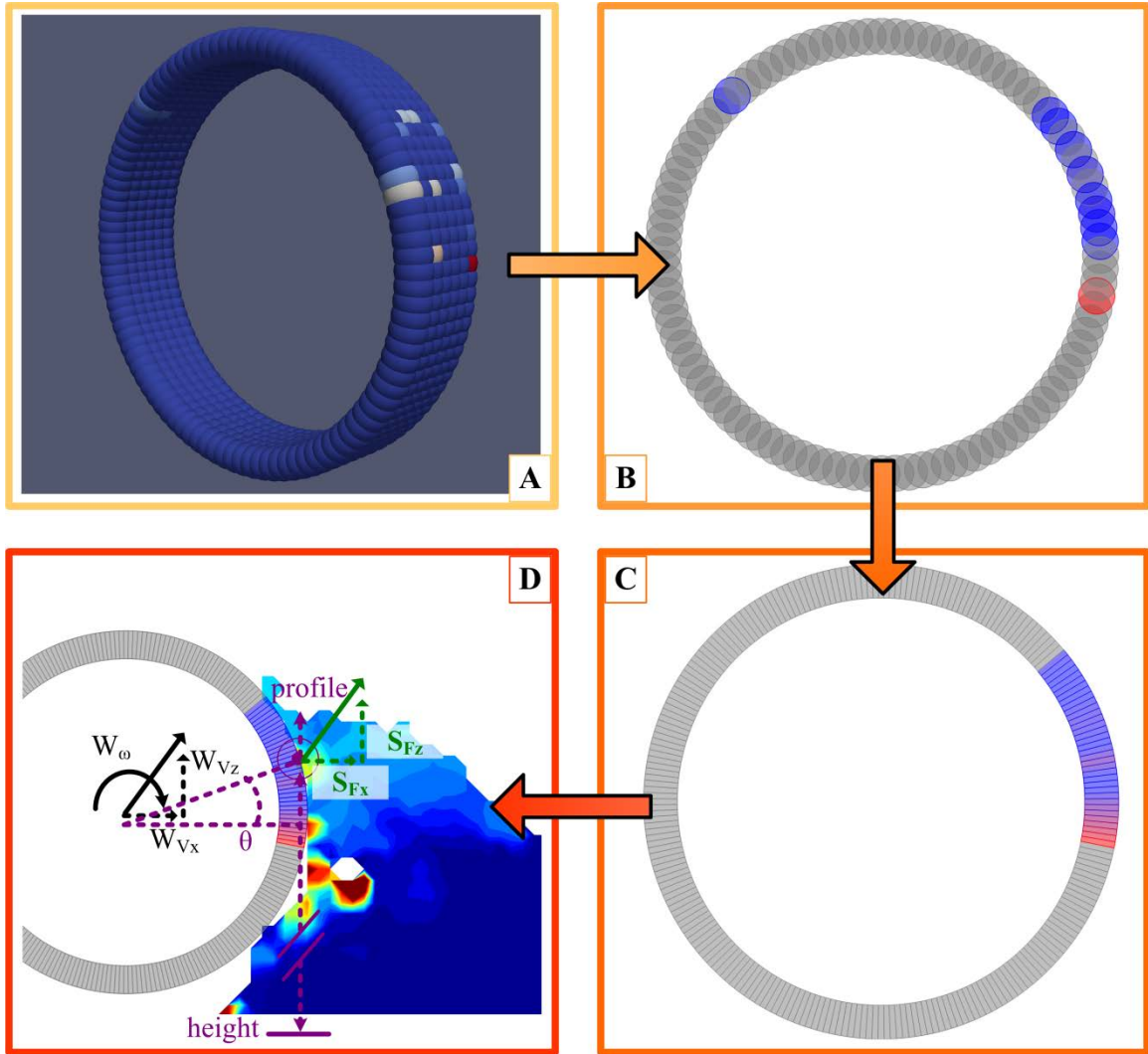


Figure 5.7 Outline of force mapping method. (a) constant-velocity motion DEM simulation. (b) output from DEM consists of time-averaged particle states. Particles are colored based on wheel-soil force magnitude. (c) conversion from particle force values to angle-based grid pressure values. (d) table force values (S_{Fx} , S_{Fz}) are created by determining the input values ($W\omega$, W_{Vx} , W_{Vz} , θ , *profile* or *height*) for each table dimension.

The wheel force lookup tables store the wheel-soil interaction force (one table for x -axis force S_{Fx} , one table for z -axis force S_{Fz}) as a function of several states: wheel x -velocity W_{Vx} , wheel z -velocity W_{Vz} , wheel angular velocity $W\omega$, angular position along the wheel θ , and either the soil profile height relative to the wheel center (*profile*) or the wheel center height relative to the soil floor (*height*). In determining the key independent variables for wheel-soil force, angular position and wheel velocity are essential (it is expected that the wheel-soil interaction has some rate dependence, especially

corresponding to angular velocity). Due to the vertical discontinuity caused by the wheel (described in the previous section), the wheel tables are segmented into two regions: Bottom and Top. These two regions are sufficient to cover the entire range of angular positions along the wheel, and do not require the Left and Right regions from before. For the Bottom region it was hypothesized that the reaction force developed by the soil would be strongly influenced by the relative distance to the floor (shown as “height” in the figure). For the Top region it was hypothesized that the reaction force developed by the soil would be strongly influenced by the wheel depth relative to the soil surface (shown as “profile” in the figure). Therefore, the final independent variable for the Bottom and Top region was the wheel height and soil profile, respectively. It was hypothesized that these five variables would capture the most important wheel-soil interaction dynamics. The wheel-soil interaction force tables are described analytically below:

$$\text{Wheel Tables: } S_{F_x, F_z} = f(W_\omega, W_{V_x}, W_{V_z}, \theta, \text{profile/height}) \quad (3.24)$$

In order to populate the wheel tables, information is extracted from each constant-velocity (fixed W_{V_x} , W_{V_z} , and $W\omega$) DEM simulation at regular intervals. DEM outputs the wheel-soil interaction force for each particle, however for use in S-DEM this must be smoothed and converted to pressure (in two-dimensions this corresponds to force per unit arc length). The first step in this process is to average the wheel particle force values along the y -axis, in order to convert from the quasi-2D DEM output to true 2D. Determining the corresponding arc length for a given contact force was approximated by assuming continuous contact for wheel particles that overlapped. Stage (c) shows the pressure magnitude after conversion from the discrete wheel-soil interaction forces. It should be noted that the single wheel particle with a non-zero force did not result in a pressure value since it was too far removed from another non-zero force. At each discretized angular position θ along the wheel all of the input dimensions of the soil table are known except for the soil profile, which is interpolated. Finally, the wheel table is populated at all non-empty θ locations where soil contact occurs. Stage (d) shows an example data point with its input dimensions highlighted.

As with the soil tables, output from the DEM simulations does not provide data for all table locations for a variety of reasons. For example, not all soil profiles values may exist for a given simulation (e.g. for positive vertical velocity simulations the initial

soil profile was high enough to populate the largest profile table value). Additionally, there is no promise that soil will be in contact with every wheel location at all times during the simulation (e.g. when the wheel moves forward, the rearward side of the wheel may not be touching soil). After post-processing all constant-velocity DEM simulation the wheel force tables may be sparse. In order to allow for efficient implementation, table values were smoothed and empty data points were estimated.

A few important details in the development of the wheel tables should be noted. The use of wheel height above the soil floor assumes that the wheel tables will not be applied to soil with a soil bin height greater than was used in the constant-velocity DEM simulations. In addition, this technique does not necessarily capture the relationship between wheel sinkage and soil reaction force for soil profile heights different from that used in the constant-velocity simulations. Wheel height was chosen as an independent variable, rather than wheel sinkage, due to the difficulty in determining the correct value for sinkage during a wheel locomotion simulation over rough terrain. Not incorporating wheel sinkage may have negatively influenced S-DEM simulation results, and is a possible area of future development. It should also be noted that the wheel tables include only the wheel-soil interaction force; they are not influenced by the mass of the wheel. This property is essential for S-DEM multibody dynamics simulations where the normal load acting on the wheel will vary.

5.2.4 Table Implementation

S-DEM simulations can be performed after the wheel and soil tables have been created using information from the constant-velocity motion DEM simulation output. First, the simulation environment is populated with a grid of soil points (soil points simply represent the location of soil, they do not represent a free body, and they do not have size). When simulating wheel locomotion it is only necessary to build points along the profile since wheel-soil interaction forces only occur on the wheel surface. Next, the wheel is placed in the simulation environment. For wheel locomotion simulations the wheel is treated as a free body, so it is necessary to have soil points below the wheel. Figure 5.8 shows a screenshot of an S-DEM wheel locomotion simulation. The velocity of each soil point is interpolated using the soil velocity tables. Wheel forces are

interpolated at discrete θ locations where soil particles contact the wheel. Stage (b) highlights the input values necessary for wheel force and soil velocity interpolation.

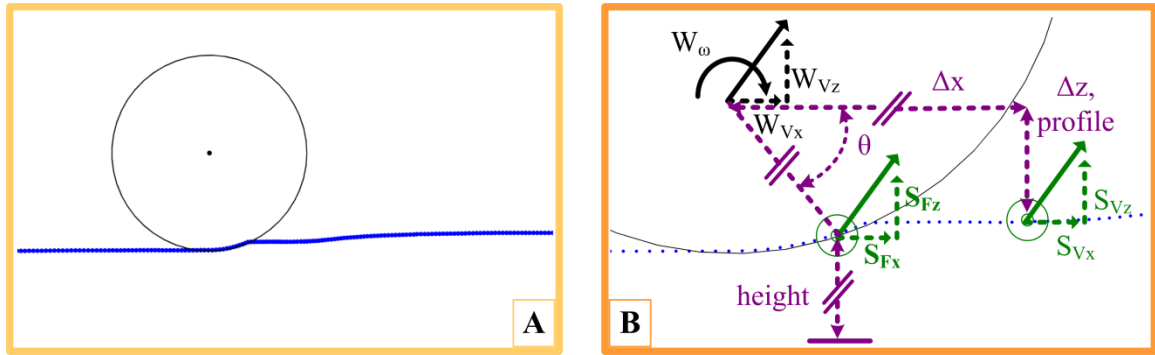


Figure 5.8 Screenshot of S-DEM with implementation details. (a) S-DEM simulation of wheel locomotion. (b) magnification shows inputs to wheel force and soil velocity tables.

Figure 5.9 provides a flow chart of the general S-DEM computation procedure for a given time step. While the figure covers the general computation outline, particularly the use of the wheel and soil lookup tables, there are some additional details. Wheel locomotion simulations, for both DEM and S-DEM, are run at constant longitudinal and angular velocities. DEM simulations use a short enough time step that the longitudinal velocity can be maintained by applying a longitudinal force using a proportional controller with a large gain, while the angular velocity can be maintained by applying a torque using a proportional controller with a large gain. In the interest of computational efficiency, S-DEM simulations use a much larger time step, necessitating an integral controller to maintain longitudinal velocity. S-DEM simulations use a fixed angular velocity, rather than maintain it using a controller torque. The wheel-soil reaction torque that occurs during S-DEM simulations is assumed to equal the driving torque required to maintain the desired angular velocity.

One of the major assumptions in developing S-DEM is that constant-velocity DEM simulations can be used to extract soil velocity as a function of wheel state. During the DEM simulations soil motion is almost entirely a result of wheel-soil interaction (soil remains in contact with the wheel until the wheel moves above the soil profile, and the soil exhibits negligible inertia). A modification is necessary with S-DEM however to prevent soil motion without sufficient wheel-soil interaction. Soil positions are not updated unless the z -axis soil reaction force is equal to or greater than the wheel weight.

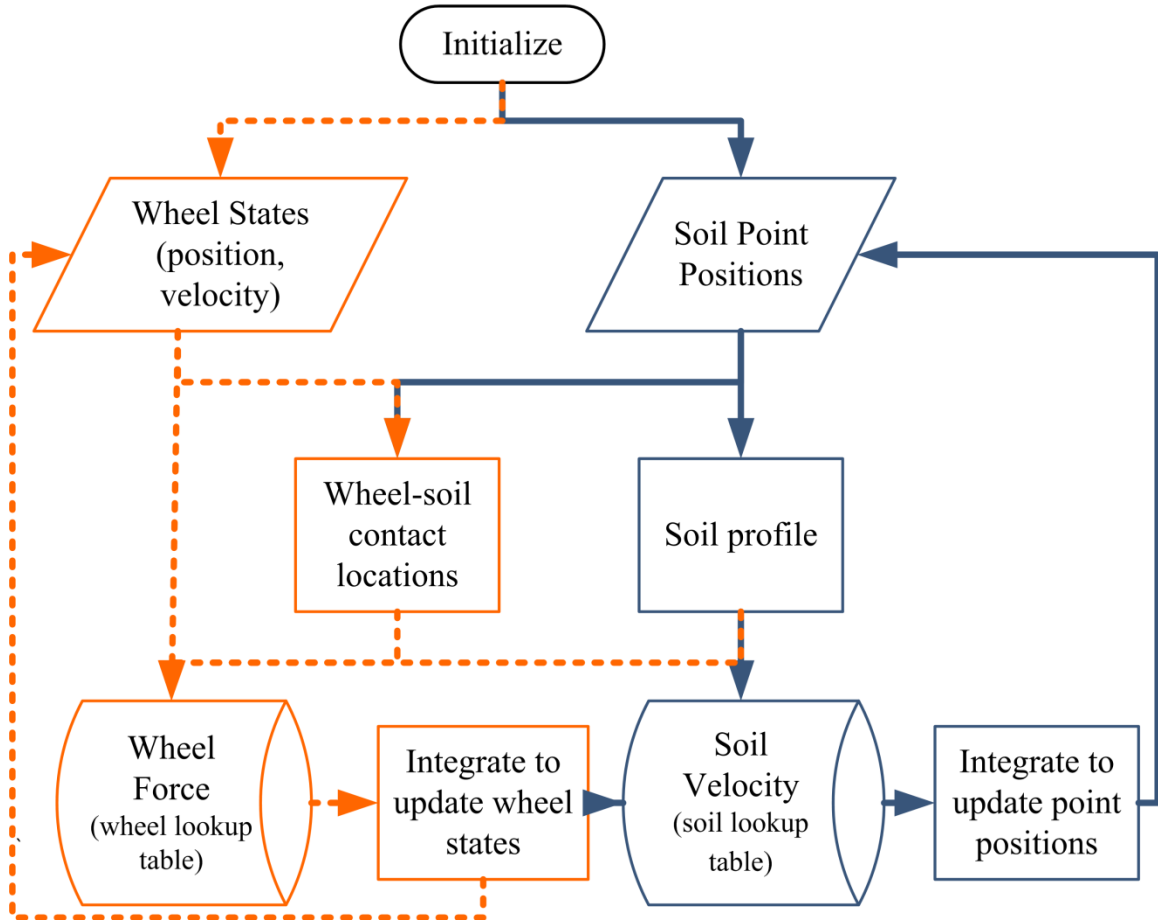


Figure 5.9 Flowchart of S-DEM computation procedure.

New soil point positions, after being updated using the soil velocity tables, are generally outside the wheel. Since the soil velocity tables do not guarantee that soil points will remain outside the wheel, occasionally it is necessary to modify the point locations. After velocity integration, soil points within the wheel were moved radially away from the wheel center, allowing no more than 0.5mm penetration.

The final modification necessary is the result of a limitation in the simulation method used to create the lookup table data. Using the current method, it is not possible to simulate zero vertical velocity because the soil profile for the constant-velocity simulations is flat, and it is necessary for the wheel to be simulated above and below the soil surface. The need to interpolate the wheel-soil interaction force and soil velocity S-DEM tables becomes problematic when simulating wheel locomotion. Small differences between the force and velocity values stored in S-DEM lookup tables and the true DEM values can produce errors that become large when integrated over a long enough period

of time. When simulating wheel locomotion the wheel’s vertical velocity was rounded to zero for values within 5% of the longitudinal velocity, as a way to avoid near-zero interpolation errors. Modifications to the S-DEM method, particularly in the setup of the constant-velocity simulations, will be investigated in the future to avoid the need to round.

5.3 Simulation Specifications

Mojave Martian Simulant was chosen as the test soil. A smooth cylindrical wheel was chosen to simplify S-DEM development, avoiding three-dimensional shape effects and the influence of grousers. The wheel was scaled down to reduce DEM simulation time, while its mass was proportionally reduced. Details for both DEM and S-DEM simulations are provided below.

5.3.1 DEM

As was performed in the previous chapter, large soil bodies were created by packing a small rectangular prism, which was duplicated along the x -axis. Because the DEM simulations were intended to be pseudo two-dimensional, the y dimension was reduced to 30 mm and restricted using fixed boundary walls. The DEM soil parameters, shown in Table 5.3, are slightly modified from those of the last chapter. It was determined through trial and error that simulating in quasi-2D (as opposed to 3D) required a reduction in coefficient of restitution to prevent large stress concentrations away from the wheel, which can result in brief “particle explosions.” As a result of the restricted y -axis motion, soil particles could not move to reduce stress until the stress reached extremely large values. These large stresses resulted in brief periods of large displacement or projectiles away from the wheel. It was found that reducing the coefficient of restitution prevented these explosions while displaying reasonable soil macro behavior. Simulation time step remained at 2.2e^{-6} seconds.

Table 5.3 DEM soil parameters

Parameter	Value
particle diameter [mm]	2.5 - 10
particle density [g/cm ³]	3.182 - 3.340
bulk density [g/cm ³]	1.6
Y [Pa]	7.0x10 ⁷
ν [-]	0.35
μ_c [-] (particle, wall)	0.86, 0.0
μ_r [-](particle, wall)	6.75x10 ⁸ , 0.0
e [-](particle, wall)	0.06, 0.06

The wheel used for these simulations is essentially a scaled-down 2D version of the wheel from the previous chapter. The wheel width was reduced to 30 mm for use in the quasi-2D environment. The wheel radius was reduced to 65 mm to limit the distance of travel required in the constant-velocity DEM simulations, thereby reducing the simulation time and output data size. The wheel mass was proportionally scaled to 0.55 kg.

5.3.2 S-DEM

S-DEM has remarkably few parameters or settings; it primarily consists of the lookup tables. The integral controller gain used to regulate longitudinal velocity has a gain of 300, which was found through trial and error to keep velocity errors low while keeping the applied longitudinal force smooth. The simulation time step was 7e⁻⁴ seconds. Shorter time steps produced nearly identical results.

5.4 S-DEM Validation

To determine the effectiveness of S-DEM at capturing the desired DEM simulation characteristics and its computation efficiency, wheel-locomotion simulations

were performed using DEM and S-DEM over smooth, flat terrain and over rough terrain. Simulations were performed using the same wheel specifications as used for the constant-velocity simulations. Simulation parameters for both DEM and S-DEM are listed in Table 5.4. DEM simulations were run on 8 cores, using 4 Intel Xeon 5160 processors on a single server blade. S-DEM simulations were run on 1 core of an Intel i7-2820QM processor.

Table 5.4 Validation simulation parameters

Field	Parameter	Value
General		
	angular velocity [deg/s]	17
	slip ratios [-]	-0.7, -0.5, -0.3, -0.1, 0.0, 0.1, 0.3, 0.5, 0.7
	wheel width [m]	0.03
	wheel radius [m]	0.065
	wheel mass [kg]	0.55
DEM		
	soil bed dimensions [m]	0.03 x 1.22 (W x L)
	time step [sec]	$2.2e^{-6}$
	number of soil particles [-]	~11,500
	number of wheel particles [-]	600
S-DEM		
	soil point spacing [m]	0.0025
	number of soil points	~1,100
	integral gain [-]	300
	time step [sec]	$7e^{-4}$

5.4.1 Smooth Soil Validation

Wheel locomotion was simulated on smooth, flat, level soil to determine how well S-DEM matched DEM performance in steady-state. Example time series plots of

drawbar pull, driving torque, and wheel sinkage at -50% and 50% slip ratio are shown in Figure 5.10 for both DEM and S-DEM simulations. During S-DEM simulations the wheel reaches near-zero vertical velocity, at which point the vertical velocity is rounded to zero. Operating at near constant velocity, the lookup tables used in S-DEM produce a near constant value for wheel-soil force interactions. As a result the S-DEM values for drawbar pull, driving torque, and sinkage do not exhibit similar time-series behavior compared with DEM. Wheel sinkage at large negative slip showed unexpected behavior during the DEM simulations; the wheel begins to rise after initial sinkage to the point it is above the initial soil profile at the end of the simulation. This behavior suggests edge-effects in the simulations, similar to those observed during the constant-velocity simulations shown in Figure 5.4, and are believed to be a result in part due to the modification from 3D to quasi-2D.

Figure 5.11 shows mean and standard deviation of drawbar pull, driving torque, and wheel sinkage results at all slip ratios for both DEM and S-DEM simulations. S-DEM mean values for drawbar pull and driving torque match DEM results well, but show near-zero standard deviation due to constant velocity operation. An exception was the simulation at 30% slip where the wheel vertical velocity was too large to be rounded to zero, producing large variations in vertical force acting on the wheel and leading to a large standard deviation in driving torque. Wheel sinkage results produced by S-DEM do not match DEM results well. Possible edge effects during DEM simulations may contribute to the sinkage error at large negative slip ratios. The accuracy of the drawbar pull and driving torque results suggests that S-DEM is reproducing the wheel-soil interaction contact area. It appears S-DEM is not as accurate at determining soil velocity ahead of the wheel (e.g. the soil profile ahead of the wheel is decreasing faster than during the DEM simulations).

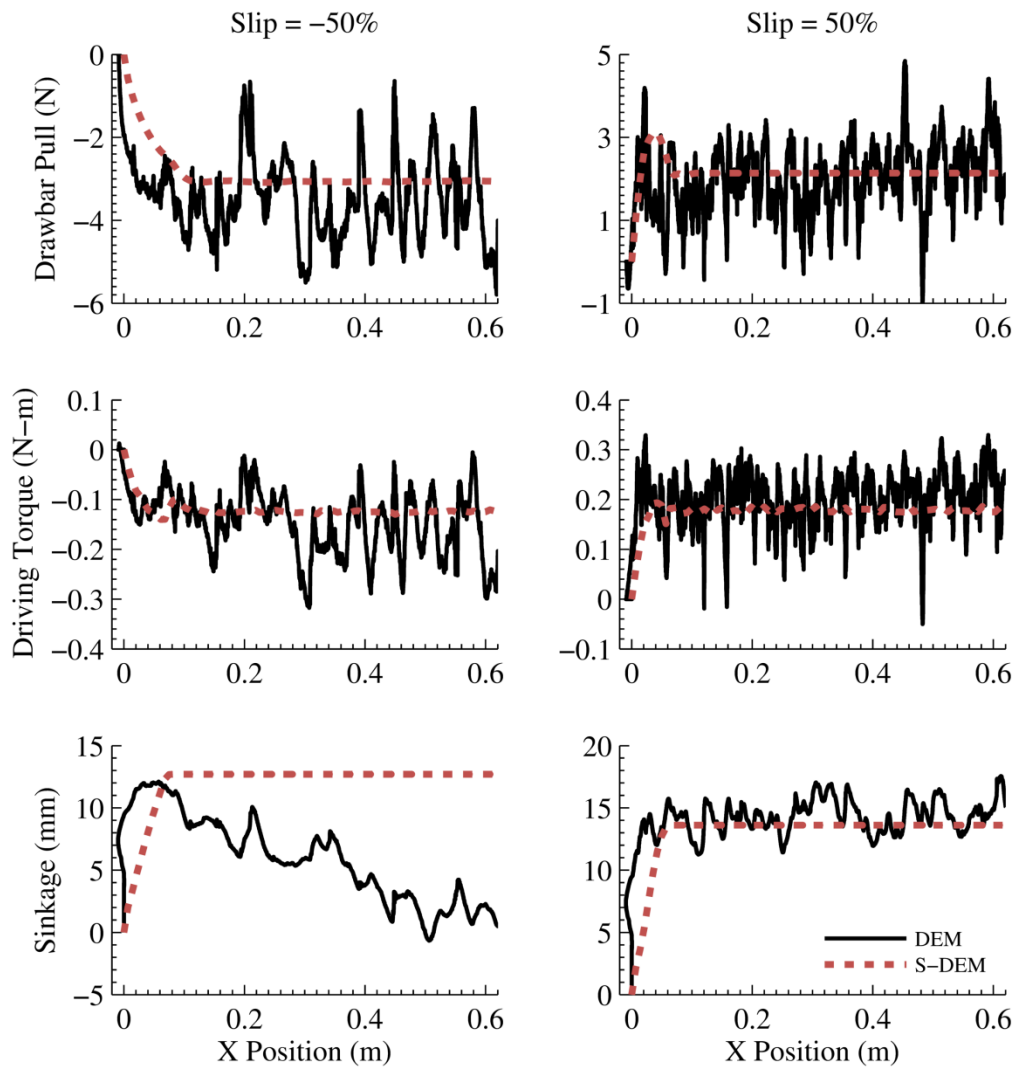


Figure 5.10 Time series plots of flat terrain wheel performance at -50% and 50% slip ratio.

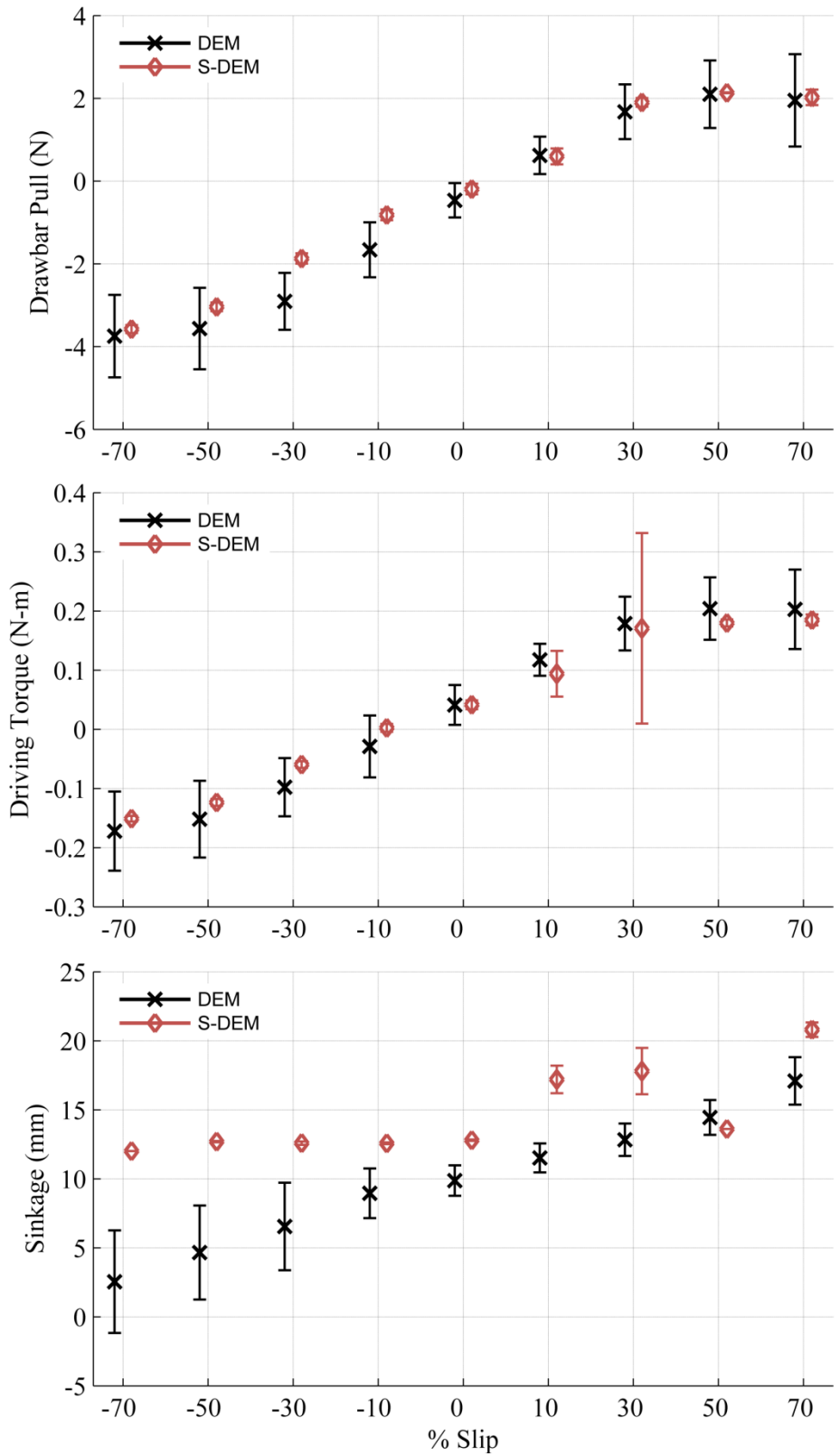


Figure 5.11 Mean and standard deviation results for flat terrain simulations.

Table 5.5 lists the simulation times and clock times at each slip ratio required for DEM and S-DEM. DEM simulations were run for an additional 1.5 seconds (0.5 seconds for initialization and 1 second for velocity ramp-up) which was unnecessary for S-DEM. The clock time results correspond to an average of 7,893 cpu seconds per simulation second for DEM and 3.6 cpu seconds per simulations second for S-DEM. This corresponds to a computation speedup of 2,223 for S-DEM vs. DEM.

Table 5.5 Steady-state computation times

Slip Ratio (%)	DEM		S-DEM	
	simulation time [sec]	clock time (8 cores) [sec]	simulation time [sec]	clock time (1 core) [sec]
-70	22.4	21,480	20.9	74.4
-50	25.2	24,660	23.7	86.8
-30	28.9	28,180	27.4	99.4
-10	34.0	32,940	32.5	117.0
0	37.3	37,860	35.8	127.6
10	41.5	40,920	40.0	142.4
30	52.9	52,020	51.4	180.8
50	73.6	73,680	72.1	250.5
70	122.0	123,660	120.5	410.7

Table 5.6 Steady-state computation comparison

Parameter	DEM	S-DEM
computation ratio [-]	7,893	3.6
cpu time per time step [sec]	0.0174	0.0025
speedup vs. DEM	-	2,223

5.4.2 Rough Terrain Validation

Wheel locomotion was simulated on rough terrain to determine how well S-DEM matched DEM performance in transient operation. Rough terrain was modeled as a sinusoidal wave with amplitude 9.75 mm and frequency 32.2 cycles per meter. Example

time series plots of drawbar pull, driving torque, and wheel sinkage at -50% and 50% slip ratio are shown in Figure 5.12 for both DEM and S-DEM simulations.

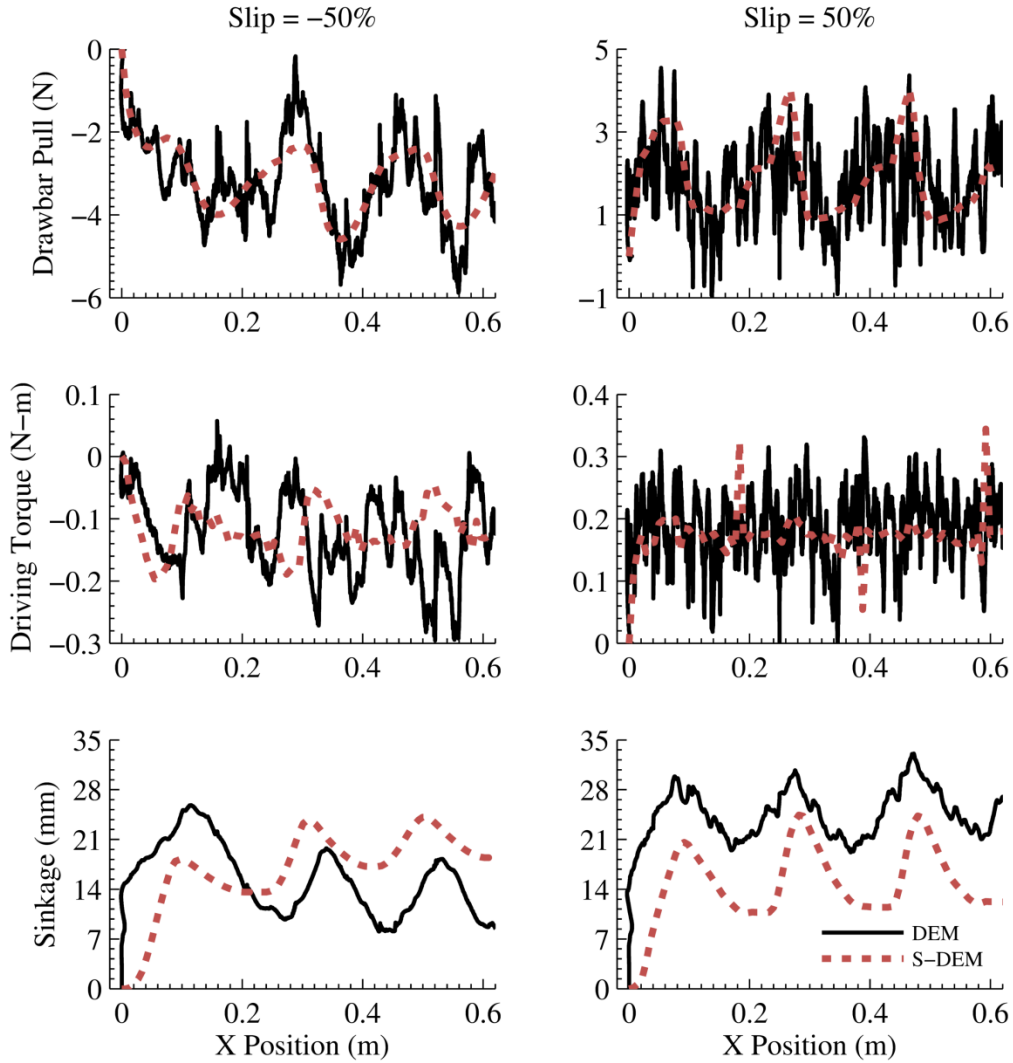


Figure 5.12 Time series plots of rough terrain wheel performance at -50% and 50% slip ratio.

During S-DEM simulations the wheel no longer remains at near-zero vertical velocity, so the rounding technique does not influence the results significantly. S-DEM drawbar pull results show excellent agreement with DEM performance, even in time-series. Wheel sinkage, however, does not match DEM results very well. As a result, driving torque values reproduce DEM results on average, but not in time-series. Edge effects again appear to influence DEM simulation results at large negative slip. At large positive slip ratios it can be seen that S-DEM simulations produced significantly less

wheel sinkage compared to DEM. Overall S-DEM was not able to fully capture the soil dynamics, however it appears the wheel-soil interaction area was once again similar. This further suggests that S-DEM is not as accurate at determining soil velocity ahead of the wheel. Figure 5.13 illustrates the S-DEM sinkage and soil dynamics errors which occur away from the wheel. The wheel-soil interaction surface for S-DEM closely matches DEM, and so do the wheel-soil interaction forces. Figure 5.14 displays example DEM and S-DEM rough terrain simulations at completion. From the figure differences in the profile trailing the wheel can be seen between the two simulations.

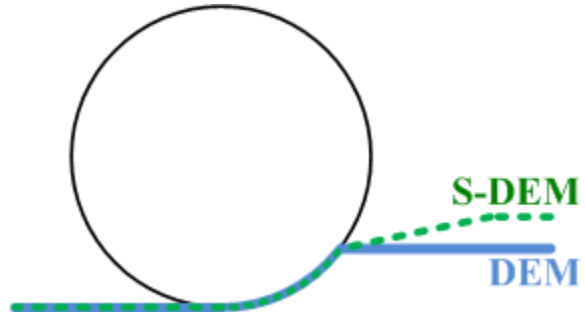


Figure 5.13 Illustration of sinkage and soil dynamics errors for S-DEM.

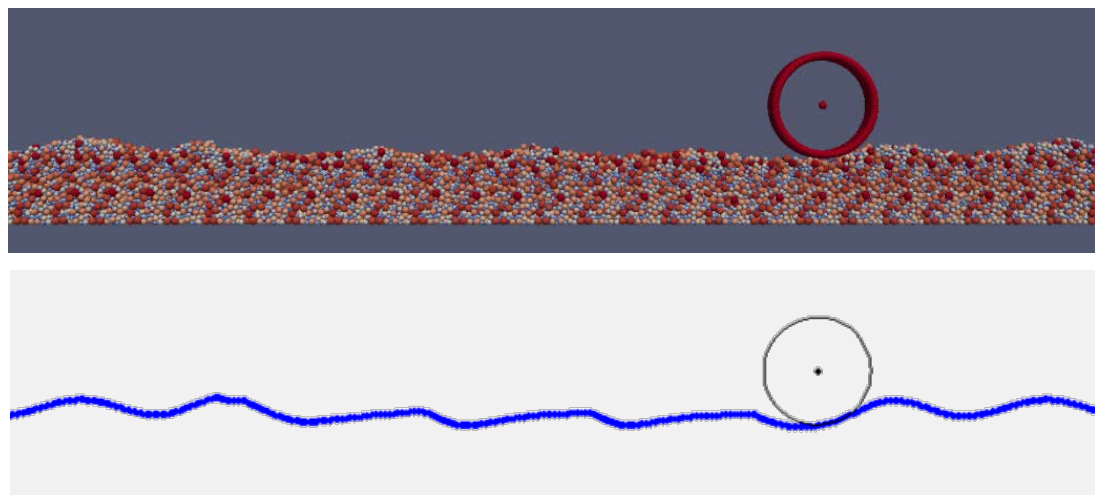


Figure 5.14 Simulation screenshots of rough terrain wheel locomotion for DEM (above) and S-DEM (below).

Figure 5.15 shows mean and standard deviation of drawbar pull, driving torque, and wheel sinkage results at all slip ratios for both DEM and S-DEM simulations. S-DEM matches DEM mean and standard deviation results well for both drawbar pull and driving torque. Again, wheel sinkage results produced by S-DEM do not match DEM results well. S-DEM produces similar sinkage results regardless of the slip ratio.

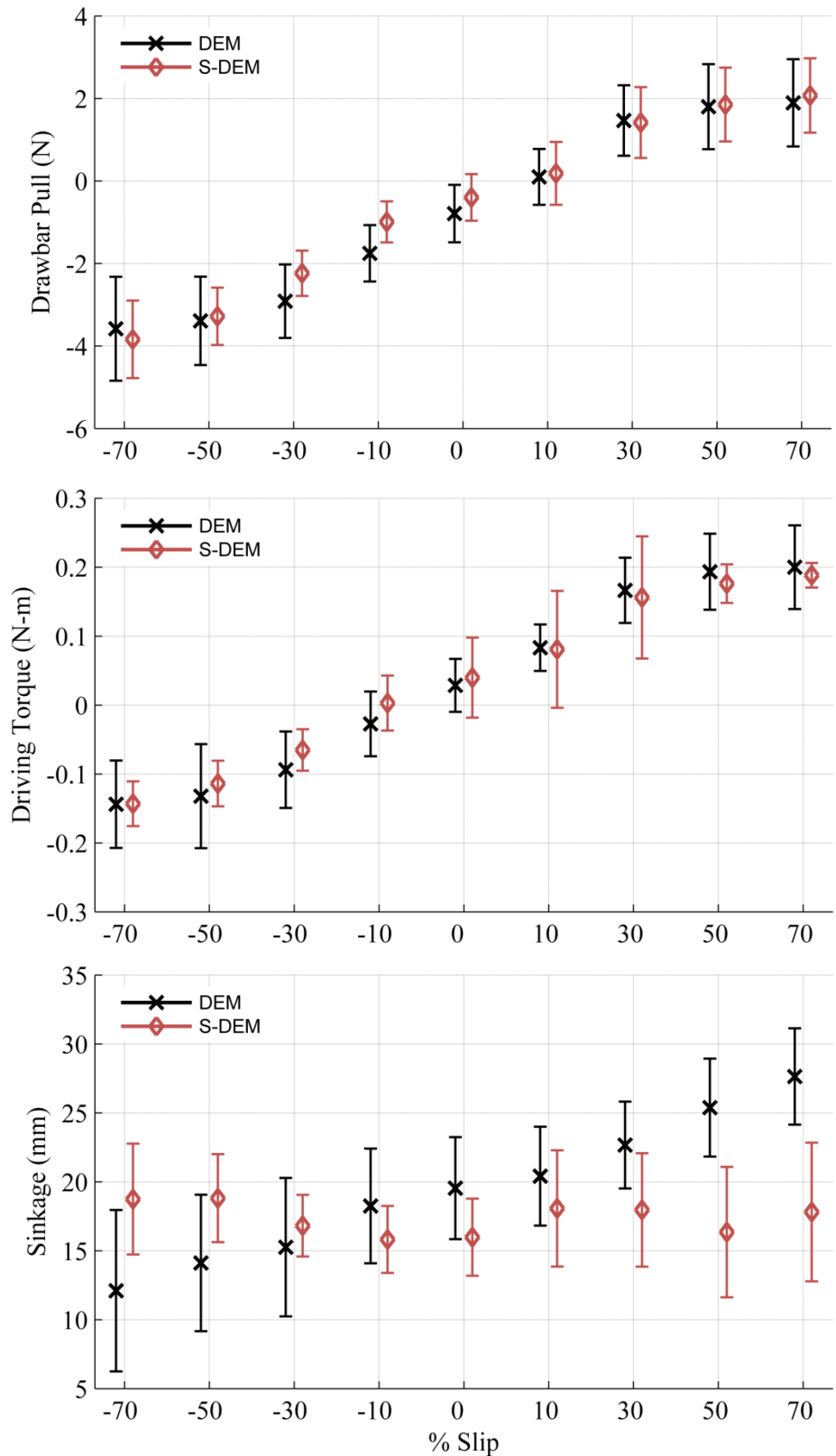


Figure 5.15 Mean and standard deviation results for rough terrain simulations.

Table 5.7 lists the simulation times and clock times at each slip ratio required for DEM and S-DEM. As was done for smooth terrain, DEM simulations included an initial 0.5 second initialization and 1.0 second velocity ramp-up. The clock time results correspond to an average of 7,933 cpu seconds per simulation second for DEM and 2.6 cpu seconds per simulation second for S-DEM. This corresponds to a computation speedup of 3,041 for S-DEM vs. DEM.

Table 5.7 Rough terrain computation times

Slip Ratio (%)	DEM		S-DEM	
	simulation time [sec]	clock time (8 cores) [sec]	simulation time [sec]	clock time (1 core) [sec]
-70	22.4	21,600	20.9	54.1
-50	25.2	24,720	23.7	63.7
-30	28.9	27,900	27.4	72.9
-10	34.0	32,820	32.5	85.5
0	37.3	38,460	35.8	93.6
10	41.5	41,040	40.0	104.0
30	52.9	52,740	51.4	133.1
50	73.6	74,100	72.1	185.4
70	122.0	124,260	120.5	305.4

Table 5.8 Rough terrain computation comparison

Parameter	DEM	S-DEM
computation ratio [-]	7,933	2.6
cpu time per time step [sec]	0.0175	0.0018
speedup vs. DEM	-	3,041

5.5 Conclusions

A surrogate discrete element method (S-DEM) was developed using constant-velocity DEM simulation results and evaluated against constant-slip wheel locomotion DEM simulation results. This work represents one of the first surrogate models developed for DEM, and the first time it is applied to terramechanics. S-DEM requires

post-processing of the constant-velocity DEM simulations to generate wheel force and soil velocity lookup tables, though implementation is roughly 2,000 to 3,000 times faster than DEM while requiring roughly 2.5 to 3.5 times real-time. This computation speed is an order of magnitude faster than the dynamic Bekker implementation described in 4.1.2. S-DEM reduced computation costs primarily through the ability to increase time step, which was roughly 300 times greater than the time step for DEM simulations. Eliminating the need for soil particle collision detection also reduced computation costs. S-DEM computation speed can be further improved by converting from *MATLAB* code to C++ (as was used for DEM simulations). S-DEM is advantageous compared to the Bekker method because it models the wheel dynamics and extracts information from DEM simulations to reproduce soil dynamics. S-DEM benefits from the prediction accuracy and discrete nature of DEM while significantly reducing computation costs. These properties make S-DEM a promising choice for use in vehicle design and control.

During validation, S-DEM was able to reproduce drawbar pull and driving torque results well, however wheel sinkage was not accurately reproduced. It appears S-DEM and DEM simulations had similar wheel-soil contact areas, but simulation of soil motion away from the wheel needs to be improved. Complicating the analysis and evaluation of S-DEM were the edge effects at the minimum and maximum x -axis dimensions that occurred during DEM simulations. It is believed the edge effects are primarily the result of the method used to produce quasi-2D simulations. It is currently unclear how best to eliminate this behavior, though possible steps include expanding the y -axis and modifying the DEM soil parameters.

Another benefit of S-DEM is the lack of tuning required. The chief parameter required for wheel locomotion is the integral gain used to control longitudinal velocity. S-DEM can be used to perform multibody dynamics simulations since the lookup tables are wheel-mass (wheel normal load) independent. Given the short computation times of S-DEM simulations, this is a significant benefit for vehicle design and control compared to DEM. S-DEM's primary disadvantage is the computation cost of simulating and post-processing the constant-velocity simulations, which must be performed for all wheel-soil combinations.

5.6 Future Work

Many research opportunities exist for improving and expanding S-DEM. The current method can be improved by correcting the edge effects encountered, likely as a result of the quasi-2D technique. Additionally, development of a constant-velocity simulation technique that allows for zero vertical velocity may eliminate the need to round the vertical velocity to zero. Further improvements to S-DEM should address the accuracy of the soil dynamics (and resulting wheel sinkage). One possibility is to make soil velocity dependent upon wheel-soil interaction. Another possibility is to increase the number of independent variables for soil velocity, such as soil profile slope. Expanding S-DEM to 3D interactions would increase the method's benefit and future applications while avoiding the issues encountered as a result of the quasi-2D technique.

Beyond the current method, S-DEM can be expanded to model more than just wheel locomotion. S-DEM could be expanded to model the stresses within the soil by further post-processing the constant-velocity results. S-DEM could be modified to model tool-soil interaction beyond wheels, such as drilling, and plowing.

CHAPTER 6

Conclusions and Future Work

6.1 Conclusions

This dissertation presented several techniques to improve the computation speed and modeling capability of terramechanics methods for small unmanned ground vehicles. Computation speed for the Bekker method, a commonly used semi-empirical terramechanics model, was improved by developing a lookup table method and a quadratic approximation method. The lookup table method is particularly well suited for use in vehicle design, as information such as maximum thrust is stored for a range of normal loads. The quadratic approximation method reduced computation times by three orders of magnitude to an average of 77 microseconds, making it possible for use in real time applications. These techniques however do not address the primary limitations of the Bekker method: its empirical nature, and its assumption of steady-state operation.

The discrete element method (DEM) is a numerical modeling method which avoids many of the limitations of the Bekker method, though at the cost of computational efficiency. Initially, experimental data from the literature of wheel locomotion and wheel digging results were used to validate DEM. The DEM results showed good qualitative agreement, but lacked numerical accuracy. DEM simulations of wheel locomotion on rough sandy terrain showed that surface roughness can potentially have a significant impact on SUGV mobility, influencing thrust production and efficiency. Later, DEM parameters were tuned to match direct shear and pressure-sinkage soil tests. Simulation accuracy was improved through the development of a velocity-dependent rolling friction term. The tuning process showed that DEM can model two important soil behaviors using a single set of parameters, even when using entirely spherical particles. DEM was shown to better predict steady-state wheel performance compared to the Bekker method. The benefits of DEM come with a high computation cost, such as an average ratio of 68

cpu hours per simulation second, limiting the applicability of DEM for vehicle design and control.

A surrogate DEM model (S-DEM) was developed to maintain the simulation capabilities of DEM at a significantly reduced computation cost. This marks one of the first surrogate models developed for DEM, and the first known model developed for terramechanics. S-DEM uses lookup tables for wheel-soil interaction forces and soil velocities, eliminating the need for costly soil particle collision detection and allowing significant increases in simulation time step. After post-processing the DEM simulations necessary to build the lookup tables, S-DEM was shown to improve computation performance by a factor of about 2,500. The current implementation required roughly 3 cpu seconds per simulation second, though many of the calculations are readily parallelizable. S-DEM reproduced drawbar pull and driving torque results well, but struggled to correctly reproduce wheel sinkage. S-DEM provides a computationally efficient alternative to the Bekker method with many of the simulation capabilities of DEM.

6.2 Future Work

This dissertation has investigated and developed several terramechanics methods for modeling transient SUGV operation, however there are more aspects to explore. Additionally, the surrogate model developed for the discrete element method shows great promise that requires further investigation. The following are several potential directions for future study:

S-DEM should be further developed to improve soil dynamics accuracy. The technique for modeling wheel-soil interaction forces produced accurate drawbar pull and driving torque results, however wheel sinkage results had significant error. Modifications to the soil velocity modeling technique are necessary. Two possible sources of error are the decoupling of wheel-soil forces and soil motion, and the limited number of independent variables used for the soil velocity tables. Another possible source of error is the constant-velocity simulation procedure which cannot be used to

simulate zero vertical velocity, and produces sparse lookup tables that require estimation. In addition, S-DEM should be expanded to model 3D interactions.

The performance effects of rough terrain on full vehicle operation should be explored. At this point all investigations into the effect of rough terrain were performed for single wheels, however vehicle dynamics are known to influence off-road performance. While the Bekker method can be adapted for use in dynamic simulations, it is unclear how well the method works when its underlying assumptions are disregarded. Roughness should be examined by performing vehicle dynamic simulations coupled with S-DEM due to its accuracy and computational efficiency. Evaluation against S-DEM results may determine what modifications to the dynamic Bekker method are necessary. Use of S-DEM should also allow for evaluation of the influence of vehicle design parameters on vehicle performance.

The surrogate model technique should be expanded for use in other DEM areas. The techniques used to develop S-DEM can be applied to other common DEM areas, such as soil drilling, excavating, and plowing. While soil velocity was the primary concern for wheel locomotion, the surrogate model can easily be adapted to model other soil properties such as internal stress state.

APPENDICES

APPENDIX A

Bekker Method Notation

Symbol	Description	Units
A_u	Soil parameter characterizing terrain response to repetitive loading	[N/m ⁴]
$a_{0,1}$	Soil coefficients for θ_m	[-]
b	Wheel width	[m]
$b_{0,1}$	Soil coefficients for θ_r	[-]
c	Soil cohesion	[N/m ²]
d_{ij}	Distance between center of particles i and j	[m]
$F_{x,y,z}$	Force in x/y/z direction	[N]
$\tilde{F}_{x,y,z}$	Force in x/y/z direction using quadratic approx.	[N]
h_f	Wheel sinkage relative to undisturbed soil	[m]
h_g	Wheel lug height	[m]
h_r	Soil rut recovery	[m]
j	Shear deformation magnitude	[m]
$j_{t,l}$	Shear deformation in tangential/lateral direction	[m]
K	Soil shear deformation parameter	[m]
k_c	Soil cohesive modulus	[N/m ⁿ⁺¹]
k_ϕ	Soil friction modulus	[N/m ⁿ⁺²]
k_o	Soil parameter characterizing terrain response to repetitive loading	[N/m ³]
K_r	Soil ratio of residual shear stress to maximum shear stress	[-]
K_w	Soil shear displacement where the shear stress peaks	[m]
$M_{x,y,z}$	Moment in x/y/z direction	[Nm]

Symbol	Description	Units
$\tilde{M}_{x,y,z}$	Moment in x/y/z direction using quadratic approx.	[Nm]
n	Soil sinkage exponent	[-]
r	Wheel radius (not including lug height)	[m]
r_s	Wheel radius including lug height	[m]
s	Slip ratio	[-]
$v_{jt,jl,jn}$	Shear rate in tangential/lateral/normal direction	[m/s]
$v_{x,y,z}$	Wheel velocity in x/y/z direction	[m/s]
z	Wheel sinkage	[m]
z_u	Wheel sinkage at unloading	[m]
β	Slip angle	[rad]
θ	Angular position along wheel-soil interface	[rad]
θ_e	Equivalent front-region contact angle for points in the rear-region of the wheel-soil interface	[rad]
θ_f	Wheel-soil entry angle	[rad]
θ_{fca}	Wheel-soil entry angle of grouser tip	[rad]
θ_{fm}	Front medium angle used in quadratic approximation	[rad]
θ_{ft}	Wheel-soil entry angle of concave portion	[rad]
θ_m	Angular position of maximum normal stress	[rad]
θ_r	Wheel-soil exit angle	[rad]
θ_{rm}	Rear medium angle used in quadratic approximation	[rad]
μ	Area ratio of grouser tip and concave region	[-]
σ	Normal stress	[N/m ²]
σ_{ca}	Normal stress in concave portion of lugged wheel	[N/m ²]
σ_e	Equivalent normal stress for lugged wheel	[N/m ²]
σ_t	Normal stress in lug tip portion of lugged wheel	[N/m ²]
τ	Shear stress magnitude	[N/m ²]
τ_e	Equivalent shear stress for lugged wheel	[N/m ²]
$\tau_{t,l}$	Shear stress in tangential/lateral direction	[N/m ²]
ϕ	Soil internal friction angle	[rad]

Symbol	Description	Units
ω	Wheel angular velocity	[rad/s]

APPENDIX B

Discrete Element Method Notation

Symbol	Description	Units
A	Contact area of two particles	[m ²]
e	Coefficient of restitution	[-]
$\mathbf{F}_{\text{cohesion}}$	Cohesive forces	[N]
$\mathbf{F}_{\text{Hertz}}$	Hertzian friction forces	[N]
G	Shear modulus	[Pa]
G_{eff}	Effective shear modulus	[Pa]
I_{eff}	Effective moment of inertia	[kg·m ²]
k_c	Cohesion energy density	[J/m ³]
$k_{\text{n/t}}$	Normal/tangential elastic spring constant	[N/m ²] or [N/m]
k_r	Rolling elastic spring coefficient	[N·m]
m_{eff}	Effective mass of two particles	[kg]
$M_{i/j}$	Mass of particle i/j	[kg]
\mathbf{n}_{ij}	Unit vector connecting the centers of two overlapping particles	[-]
proj_{ij}	Projection into the shear plane	[-]
$R_{i/j}$	Radius of particle i/j	[m]
r	Wheel radius (without grousers)	[m]
s	Wheel slip ratio	[-]
$\mathbf{T}_{\text{rolling}}$	Rolling resistance torques	[N·m]
$\mathbf{T}_r^{k/\gamma}$	Rolling resistance stiffness/damping torques	[N·m]
$\mathbf{v}_{\text{n/t}}$	Normal/tangential component of the relative velocity of the two particles	[m/s]

Symbol	Description	Units
v_x	Wheel longitudinal velocity in x -axis	[m/s]
$z_{\text{profile}}(x)$	Soil profile as a function of wheel x -axis position	[m]
$x_{\text{wheel_ctr}}$	Position of wheel center in x axis	[m]
Y_{eff}	Effective Young's modulus	[Pa]
$Y_{i/j}$	Young's modulus of particle i/j	[Pa]
$z_{\text{wheel_ctr}}$	Position of wheel center in z axis	[m]
β	Coefficient used to relate damping ratio to collision time of particles	[-]
$\gamma_{n/t}$	Normal/tangential viscoelastic damping constant	[1/m-s] or [N-s/m]
γ_r	Rolling viscoelastic damping coefficient	[N-m/s]
Δs_t	Tangential displacement vector for the two particles for contact duration	[m]
ΔT_r^k	Change in rolling resistance stiffness torque	[N-m]
$\Delta \theta_r$	Relative rotation vector	[rad]
$\Delta \omega_r$	Relative angular velocity vector	[rad/s]
Δz	Wheel sinkage	[m]
δ	Overlap length of two particles	[m]
μ_c	Coulomb static yield coefficient	[-]
μ_r	Rolling resistance coefficient	[-]
$\mu_{r,\text{eff}}$	Effective rolling resistance coefficient	[-]
$\nu_{(i,j)}$	Poisson ratio	[-]
$\omega_{i/j}$	Angular velocity of particle i/j	[rad/s]
ω_y	Wheel angular velocity in the y -axis	[rad/s]

BIBLIOGRAPHY

BIBLIOGRAPHY

- [1] R. Padbury and X. Zhang, “Lithium–oxygen batteries—Limiting factors that affect performance,” *Journal of Power Sources*, vol. 196, no. 10, pp. 4436–4444, May 2011.
- [2] “Unmanned Systems Integrated Roadmap FY2011-2036,” Department of Defense, Reference Number: 11-S-3613.
- [3] G. Meirion-Griffith and M. Spenko, “A modified pressure–sinkage model for small, rigid wheels on deformable terrains,” *Journal of Terramechanics*, vol. 48, pp. 149–155, Apr. 2011.
- [4] G. Meirion-Griffith and M. Spenko, “A pressure-sinkage model for small-diameter wheels on compactive, deformable terrain,” *Journal of Terramechanics*, Jul. 2012.
- [5] P. Richmond, G. Mason, B. Coutermash, J. Pusey, and V. Moore, “Mobility Performance Algorithms for Small Unmanned Ground Vehicles,” US Army Corps of Engineers, Engineer Research and Development Center, ERDC TR-09-6, May 2009.
- [6] C. Goodin, B. Q. Gates, C. L. Cummins, T. R. George, P. J. Durst, and J. D. Priddy, “High-fidelity physics-based simulation of a UGV reconnaissance mission in a complex urban environment,” in *Proceedings of SPIE*, 2011, vol. 8045, p. 80450X–80450X–10.
- [7] M. G. Bekker, *Theory of land locomotion: the mechanics of vehicle mobility*. University of Michigan Press, 1956.
- [8] J. Wong, *Terramechanics and off-road vehicle engineering : terrain behaviour, off-road vehicle performance and design*, 2nd ed. Amsterdam, The Netherlands: Butterworth-Heinemann, 2010.
- [9] M. G. Bekker, *Off-the-road locomotion: research and development in terramechanics*. University of Michigan Press, 1960.
- [10] M. G. Bekker, *Introduction to terrain-vehicle systems*. Ann Arbor: University of Michigan Press, 1969.
- [11] D. Gee-Clough, M. McAllister, G. Pearson, and D. W. Evernden, “The empirical prediction of tractor-implement field performance,” *Journal of Terramechanics*, vol. 15, no. 2, pp. 81–94, Jun. 1978.

- [12] J. R. Kane, P. Ayers, H. Howard, A. Anderson, and D. Koch, “Multipass coefficients for terrain impacts based on military vehicle type, size and dynamic operating properties,” *Journal of Terramechanics*, vol. 50, no. 3, pp. 175–183, Jun. 2013.
- [13] M. Gobbi, M. Aiolfi, M. Pennati, G. Previati, F. Levi, M. Ribaldone, and G. Mastinu, “Measurement of the forces and moments acting on farm tractor pneumatic tyres,” *Vehicle System Dynamics*, vol. 43, pp. 412–433, Jan. 2005.
- [14] G. Dagan and M. Tulin, “A study of the steady flow of a rigid-plastic clay beneath a driven wheel,” *Journal of Terramechanics*, vol. 6, pp. 9–27, 1969.
- [15] J. A. Pytka, “Semiempirical model of a wheel-soil system,” *International Journal of Automotive Technology*, vol. 11, pp. 681–690, Sep. 2010.
- [16] M. Faragalli, D. Pasini, and P. Radziszewski, “A Parametric study and experimental testing of lunar-wheel suspension on dynamic terrainability,” *Can. Aeronaut. Space J.*, vol. 57, no. 1, pp. 65–74, 2011.
- [17] V. Asnani, D. Delap, and C. Creager, “The development of wheels for the Lunar Roving Vehicle,” *Journal of Terramechanics*, vol. 46, no. 3, pp. 89–103, Jun. 2009.
- [18] L. Ding, H. Gao, Z. Deng, K. Yoshida, and K. Nagatani, “Slip ratio for lugged wheel of planetary rover in deformable soil: definition and estimation,” in *Proceedings of the International Conference on Intelligent Robots and Systems*, 2009, pp. 3343–3348.
- [19] B. Trease, R. Arvidson, R. Lindemann, K. Bennett, F. Zhou, K. Iagnemma, C. Senatore, and L. Van Dyke, “Dynamic modeling and soil mechanics for path planning of the Mars exploration rovers,” in *IDETC/CIE*, Washington, D.C., 2011.
- [20] R. A. Irani, R. J. Bauer, and A. Warkentin, “A dynamic terramechanic model for small lightweight vehicles with rigid wheels and grousers operating in sandy soil,” *Journal of Terramechanics*, vol. 48, pp. 307–318, Aug. 2011.
- [21] G. Ishigami, A. Miwa, K. Nagatani, and K. Yoshida, “Terramechanics-based model for steering maneuver of planetary exploration rovers on loose soil,” *J. Field Robotics*, vol. 24, no. 3, pp. 233–250, Mar. 2007.
- [22] Y. Favaedi, A. Pechev, M. Scharringhausen, and L. Richter, “Prediction of tractive response for flexible wheels with application to planetary rovers,” *Journal of Terramechanics*, vol. 48, pp. 199–213, Jun. 2011.
- [23] C. Harnisch, B. Lach, R. Jakobs, M. Troulis, and O. Nehls, “A new tyre-soil interaction model for vehicle simulation on deformable ground,” *Vehicle System Dynamics*, vol. 43, pp. 384–394, 2005.

- [24] B. Schäfer, A. Gibbesch, R. Krenn, and B. Rebele, “Planetary rover mobility simulation on soft and uneven terrain,” *Vehicle System Dynamics*, vol. 48, no. 1, pp. 149–169, Jan. 2010.
- [25] C. Senatore and C. Sandu, “Off-road tire modeling and the multi-pass effect for vehicle dynamics simulation,” *Journal of Terramechanics*, vol. 48, pp. 265–276, Aug. 2011.
- [26] M. Sargana, D. Geeclough, and C. Gupta, “A dynamic equation for the pressure-sinkage relationship in saturated clay soils,” *Journal of Terramechanics*, vol. 22, pp. 111–120, 1985.
- [27] A. Gibbesch and B. Schäfer, “Multibody system modelling and simulation of planetary rover mobility on soft terrain,” in *Proc. of the 8th International Symposium on Artificial Intelligence, Robotics and Automation in Space - iSAIRAS*, Munich, Germany, 2005.
- [28] Liang Ding, K. Nagatani, K. Sato, A. Mora, K. Yoshida, Haibo Gao, and Zongquan Deng, “Terramechanics-based high-fidelity dynamics simulation for wheeled mobile robot on deformable rough terrain,” in *Proceedings of the International Conference on Robotics and Automation (ICRA)*, 2010, pp. 4922–4927.
- [29] W. Li, L. Ding, H. Gao, Z. Deng, and N. Li, “ROSTDyn: Rover simulation based on terramechanics and dynamics,” *Journal of Terramechanics*, vol. 50, no. 3, pp. 199–210, Jun. 2013.
- [30] N. Patel, R. Slade, and J. Clemmet, “The ExoMars rover locomotion subsystem,” *Journal of Terramechanics*, vol. 47, pp. 227–242, Aug. 2010.
- [31] D. Apostolopoulos, “Analytical configuration of wheeled robotic locomotion.” The Robotics Institute of Carnegie Mellon University Technical Report CMU-RI-TR-01-08, Apr-2001.
- [32] S. Michaud, L. Richter, T. Thueer, A. Gibbesch, N. Patel, T. Huelsing, L. Joudrier, R. Siegwart, and B. Schaefer, “Rover chassis evaluation and design optimisation using the RCET,” in *The 9th ESA Workshop on Advanced Space Technologies for Robotics and Automation (ASTRA '06)*, Nordwijk, The Netherlands, 2006.
- [33] N. Patel, A. Ellery, E. Allouis, M. Sweeting, and L. Richter, “Rover mobility performance evaluation tool (RMPET): A systematic tool for rover chassis evaluation via application of Bekker theory,” in *Proceedings of the 8th ESA Workshop on Advanced Space Technologies for Robotics and Automation “ASTRA 2004” ESTEC*, Nov. 2004.
- [34] L. Ding, K. Yoshida, K. Nagatani, H. Gao, and Z. Deng, “Parameter identification for planetary soil based on a decoupled analytical wheel-soil interaction

terramechanics model,” in *Proceedings of the International Conference on Intelligent Robots and Systems*, 2009, pp. 4122–4127.

- [35] K. Iagnemma, S. Kang, C. Brooks, and S. Dubowsky, “Multi-Sensor Terrain Estimation for Planetary Rovers,” in *Proceedings of the 7th International Symposium on Artificial Intelligence, Robotics and Automation in Space (iSAIRAS)*, 2003.
- [36] K. Iagnemma, S. Kang, H. Shibly, and S. Dubowsky, “Online Terrain Parameter Estimation for Wheeled Mobile Robots With Application to Planetary Rovers,” *IEEE Transactions on Robotics*, vol. 20, pp. 921–927, Oct. 2004.
- [37] H. Shibly, K. Iagnemma, and S. Dubowsky, “An equivalent soil mechanics formulation for rigid wheels in deformable terrain, with application to planetary exploration rovers,” *Journal of Terramechanics*, vol. 42, no. 1, pp. 1–13, Jan. 2005.
- [38] K. Iagnemma and S. Dubowsky, “Traction Control of Wheeled Robotic Vehicles in Rough Terrain with Application to Planetary Rovers,” *The International Journal of Robotics Research*, vol. 23, pp. 1029–1040, Oct. 2004.
- [39] A. Angelova, L. Matthies, D. Helmick, and P. Perona, “Fast Terrain Classification Using Variable-Length Representation for Autonomous Navigation,” 2007, pp. 1–8.
- [40] I. Halatci, C. A. Brooks, and K. Iagnemma, “A study of visual and tactile terrain classification and classifier fusion for planetary exploration rovers,” *Robotica*, vol. 26, p. 767, Apr. 2008.
- [41] D. M. Helmick, Yang Cheng, D. S. Clouse, L. H. Matthies, and S. I. Roumeliotis, “Path following using visual odometry for a Mars rover in high-slip environments,” in *Aerospace Conference, 2004. Proceedings. 2004 IEEE*, 2004, vol. 2, pp. 772–789 Vol.2.
- [42] D. Helmick, A. Angelova, and L. Matthies, “Terrain Adaptive Navigation for planetary rovers,” *Journal of Field Robotics*, vol. 26, pp. 391–410, Apr. 2009.
- [43] S. Shimoda, Y. Kuroda, and K. Iagnemma, “High-speed navigation of unmanned ground vehicles on uneven terrain using potential fields,” *Robotica*, vol. 25, p. 409, Jan. 2007.
- [44] T. R. Way, “Three Single Wheel Machines for Traction and Soil Compaction Research,” *Agricultural Engineering International: CIGR Journal*, vol. XI, 2009.
- [45] V. Salokhe, Tranthihong, and D. Geeclough, “Effects of low-to-medium slip, lug spacing and moisture content on lug forces,” *Journal of Terramechanics*, vol. 31, pp. 385–394, Nov. 1994.
- [46] H. Shinone, H. Nakashima, Y. Takatsu, T. Kasetani, H. Matsukawa, H. Shimizu, J. Miyasaka, and K. Ohdoi, “Experimental Analysis of Tread Pattern Effects on Tire Tractive Performance on Sand using an Indoor Traction Measurement System with

- Forced-slip Mechanism,” *Engineering in Agriculture, Environment and Food*, vol. 3, no. 2, pp. 61–66, 2010.
- [47] H. Taghavifar and A. Mardani, “Investigating the effect of velocity, inflation pressure, and vertical load on rolling resistance of a radial ply tire,” *Journal of Terramechanics*, vol. 50, no. 2, pp. 99–106, Apr. 2013.
- [48] D. Wulfsohn and S. K. Upadhyaya, “Prediction of traction and soil compaction using three-dimensional soil-tyre contact profile,” *Journal of Terramechanics*, vol. 29, no. 6, pp. 541–564, Nov. 1992.
- [49] C. W. Fervers, “Improved FEM simulation model for tire–soil interaction,” *Journal of Terramechanics*, vol. 41, no. 2–3, pp. 87–100, Jul. 2004.
- [50] C. Kolsch, “Vertical vehicle dynamics on soft ground - investigations with FEM,” *7th Conference FISITA, Seoul, Korea*, 2000.
- [51] J. H. Lee, “Finite element modeling of interfacial forces and contact stresses of pneumatic tire on fresh snow for combined longitudinal and lateral slips,” *Journal of Terramechanics*, vol. 48, pp. 171–197, Jun. 2011.
- [52] S. Shoop, K. Kestler, and R. Haehnel, “Finite Element Modeling of Tires on Snow,” *Tire Science and Technology, TSTCA*, vol. 34, no. 1, pp. 2–37, Mar. 2006.
- [53] K. Xia, “Finite element modeling of tire/terrain interaction: Application to predicting soil compaction and tire mobility,” *Journal of Terramechanics*, vol. 48, pp. 113–123, Apr. 2011.
- [54] R. N. Yong and E. A. Fattah, “Prediction of wheel-soil interaction and performance using the finite element method,” *Journal of Terramechanics*, vol. 13, no. 4, pp. 227–240, Dec. 1976.
- [55] A. G. Varghese, J. L. Turner, T. R. Way, C. E. Johnson, and H. R. Dorfi, “Traction Prediction of a Smooth Rigid Wheel in Soil using Coupled Eulerian-Lagrangian Analysis,” presented at the SIMULIA Community Conference, 2012.
- [56] J. P. Pruiksma, G. A. M. Kruse, J. A. M. Teunissen, and M. F. P. van Winnendael, “Tractive performance modelling of the ExoMars rover wheel design on loosely packed soil using coupled Eulerian Lagrangian finite element techniques,” *11th Symposium on Advanced Space Technologies in Robotics and Automation*, Apr. 2011.
- [57] L. Uthus, M. A. Hopkins, and I. Horvli, “Discrete element modelling of the resilient behaviour of unbound granular aggregates,” *International Journal of Pavement Engineering*, vol. 9, no. 6, pp. 387–395, Dec. 2008.

- [58] M. A. Knuth, J. B. Johnson, M. A. Hopkins, R. J. Sullivan, and J. M. Moore, “Discrete element modeling of a Mars Exploration Rover wheel in granular material,” *Journal of Terramechanics*, Oct. 2011.
- [59] R. Yang, M. Xu, X. Liang, S. Zhang, Y. Cheng, H. Xu, and J. Yang, “Experimental study and DEM analysis on rigid driving wheel’s performance for off-road vehicles moving on loose soil,” 2011, pp. 142–147.
- [60] T. Tsuji, Y. Nakagawa, N. Matsumoto, Y. Kadono, T. Takayama, and T. Tanaka, “3-D DEM simulation of cohesive soil-pushing behavior by bulldozer blade,” *Journal of Terramechanics*, vol. 49, no. 1, pp. 37–47, Feb. 2012.
- [61] R. M. Mukherjee and R. Houlihan, “Massively parallel granular media modeling of robot-terrain interactions,” presented at the Proceedings of the ASME 2012 International Design Engineering Technical Conferences & Computers and Information in Engineering Conference IDETC/CIE 2012, Chicago, IL, 2012.
- [62] H. Nakashima, H. Fujii, A. Oida, M. Momozu, Y. Kawase, H. Kanamori, S. Aoki, and T. Yokoyama, “Parametric analysis of lugged wheel performance for a lunar microrover by means of DEM,” *Journal of Terramechanics*, vol. 44, no. 2, pp. 153–162, Apr. 2007.
- [63] H. Nakashima, H. Fujii, A. Oida, M. Momozu, H. Kanamori, S. Aoki, T. Yokoyama, H. Shimizu, J. Miyasaka, and K. Ohdoi, “Discrete element method analysis of single wheel performance for a small lunar rover on sloped terrain,” *Journal of Terramechanics*, vol. 47, no. 5, pp. 307–321, Oct. 2010.
- [64] T. R. Canfield and M. J. Murray, “The use of finite elements to model soil/track interactions in coupled multi-body dynamic simulations: Is real time simulation feasible?,” presented at the 1992 Summer Computer Simulation Conference, Reno, NV, 1992.
- [65] H. Nakashima and A. Oida, “Algorithm and implementation of soil–tire contact analysis code based on dynamic FE–DE method,” *Journal of Terramechanics*, vol. 41, no. 2–3, pp. 127–137, Jul. 2004.
- [66] H. Nakashima, Y. Takatsu, H. Shinone, H. Matsukawa, and T. Kasetani, “FE-DEM Analysis of the Effect of Tread Pattern on the Tractive Performance of Tires Operating on Sand,” *Journal of Mechanical Systems for Transportation and Logistics*, vol. 2, no. 1, pp. 55–65, 2009.
- [67] R. Zhang, B. Chen, and J. Li, “Research on the continuum/discontinuum multiscale analytical system of the interaction between rigid wheel and lunar soil,” 2009, pp. 765–768.
- [68] J. Wong, “The effect of vibrations on the performance of terrain-vehicle systems,” *Journal of Terramechanics*, vol. 7, pp. 11–21, 1970.

- [69] J. Wong, “Effect of vibration on the performance of off-road vehicles,” *Journal of Terramechanics*, vol. 8, pp. 25–42, 1972.
- [70] L. Laib, “On the mobility of cross-country vehicles, with emphasis on modeling their dynamic motion,” *Vehicle System Dynamics*, vol. 29, no. sup1, pp. 682–703, Jan. 1998.
- [71] L. Laib, P. Kiss, and G. Antos, “The effects of off-road vehicle on the soil cohesion and internal friction,” *Jarmuvek es Mobilgepek*, vol. 2, pp. 132–152, 2008.
- [72] S. Park, A. A. Popov, and D. J. Cole, “Influence of soil deformation on off-road heavy vehicle suspension vibration,” *Journal of Terramechanics*, vol. 41, no. 1, pp. 41–68, Jan. 2004.
- [73] R. Hildebrand, E. Keskinen, and J. Navarrete, “Vehicle vibrating on a soft compacting soil half-space: Ground vibrations, terrain damage, and vehicle vibrations,” *Journal of Terramechanics*, vol. 45, pp. 121–136, Aug. 2008.
- [74] S. Al-Milli, L. D. Seneviratne, and K. Althoefer, “Track–terrain modelling and traversability prediction for tracked vehicles on soft terrain,” *Journal of Terramechanics*, vol. 47, pp. 151–160, Jun. 2010.
- [75] J. Solis and R. Longoria, “Modeling track–terrain interaction for transient robotic vehicle maneuvers,” *Journal of Terramechanics*, vol. 45, pp. 65–78, Jun. 2008.
- [76] Z. Jia, W. Smith, and H. Peng, “Terramechanics-based wheel–terrain interaction model and its applications to off-road wheeled mobile robots,” *Robotica*, pp. 1–13, Jul. 2011.
- [77] Z. Jia, W. Smith, and H. Peng, “Fast analytical models of wheeled locomotion in deformable terrain for mobile robots,” *Robotica*, pp. 1–19, Mar. 2012.
- [78] K. Iagnemma, C. Senatore, B. Trease, R. Arvidson, K. Bennett, A. Shaw, F. Zhou, L. Van Dyke, and R. Lindemann, “Terramechanics modeling of Mars surface exploration rovers for simulation and parameter estimation,” in *IDETC/CIE*, Washington, D.C., 2011.
- [79] J. Madsen, P. Ayers, A. Reid, A. Seidl, G. Bozdech, J. O’Kins, and D. Negru, “A physics-based terrain model for off-road vehicle simulations,” presented at the Proceedings of the ASME 2012 International Design Engineering Technical Conferences & Computers and Information in Engineering Conference IDETC/CIE 2012, Chicago, IL, 2012.
- [80] A. P. Grima and P. W. Wypych, “Discrete element simulations of granular pile formation: Method for calibrating discrete element models,” *Engineering Computations*, vol. 28, no. 3, pp. 314–339, 2011.

- [81] Z. Jia, W. Smith, and H. Peng, “Fast computation of wheel-soil interactions for safe and efficient operation of mobile robots,” presented at the 2011 IEEE/RSJ International Conference on Intelligent Robots and Systems (IROS), 2011, pp. 3004–3010.
- [82] J. Wong and A. Reece, “Prediction of rigid wheel performance based on the analysis of soil-wheel stresses part I. Performance of driven rigid wheels,” *Journal of Terramechanics*, vol. 4, pp. 81–98, 1967.
- [83] Z. Janosi and B. Hanamoto, “The analytical determination of drawbar pull as a function of slip for tracked vehicles in deformable soils,” in *Proceedings of the 1st International Conference of the Mechanics of Soil-Vehicle Systems*, Torino, Italy: Edizioni Minerva Tecnica, 1961.
- [84] J. Y. Wong, M. Garber, J. R. Radforth, and J. T. Dowell, “Characterization of the mechanical properties of muskeg with special reference to vehicle mobility,” *Journal of Terramechanics*, vol. 16, no. 4, pp. 163–180, Dec. 1979.
- [85] J. Y. Wong, “Evaluation of soil strength measurements,” National Research Council of Canada, NRCC Report No. 22881, 1983.
- [86] J. Y. Wong and C. F. Chiang, “A general theory for skid steering of tracked vehicles on firm ground,” *Proceedings of the Institution of Mechanical Engineers, Part D: Journal of Automobile Engineering*, vol. 215, no. 3, pp. 343–355, Jan. 2001.
- [87] W. Smith, H. Peng, Z. Filipi, D. Kramer, and M. Pozolo, “Development of a Design Tool for Small Off-Road Unmanned Wheeled Ground Vehicles: A Case Study,” presented at the AUVSI’s Unmanned Systems 2011, 2011.
- [88] L. Ding, H. Gao, Z. Deng, K. Nagatani, and K. Yoshida, “Experimental study and analysis on driving wheels’ performance for planetary exploration rovers moving in deformable soil,” *Journal of Terramechanics*, vol. 48, pp. 27–45, Feb. 2011.
- [89] M. Sutoh, J. Yusa, T. Ito, K. Nagatani, and K. Yoshida, “Traveling performance evaluation of planetary rovers on loose soil,” *Journal of Field Robotics*, 2012.
- [90] L. R. Khot, V. M. Salokhe, H. P. W. Jayasuriya, and H. Nakashima, “Experimental validation of distinct element simulation for dynamic wheel–soil interaction,” *Journal of Terramechanics*, vol. 44, no. 6, pp. 429–437, Dec. 2007.
- [91] W. Li, Y. Huang, Y. Cui, S. Dong, and J. Wang, “Trafficability analysis of lunar mare terrain by means of the discrete element method for wheeled rover locomotion,” *Journal of Terramechanics*, vol. 47, no. 3, pp. 161–172, Jun. 2010.
- [92] H. Nakashima and T. Kobayashi, “Effects of gravity on rigid rover wheel sinkage and motion resistance assessed using two-dimensional discrete element method,” *Journal of Terramechanics*, vol. 53, pp. 37–45, Jun. 2014.

- [93] M. A. Hopkins, J. B. Johnson, and R. Sullivan, “Discrete Element Modeling of a Rover Wheel in Granular Material Under the Influence of Earth, Mars, and Lunar Gravity,” 2008, pp. 17–17.
- [94] C. Kloss and C. Goniva, “LIGGGHTS: A new open source discrete element simulation software,” in *5th International Conference on Discrete Element Methods*, London, UK, 2010.
- [95] H. Zhang and H. Makse, “Jamming transition in emulsions and granular materials,” *Physical Review E*, vol. 72, no. 1, Jul. 2005.
- [96] N. Brilliantov, F. Spahn, J.-M. Hertzsch, and T. Pöschel, “Model for collisions in granular gases,” *Physical Review E*, vol. 53, no. 5, pp. 5382–5392, May 1996.
- [97] L. Silbert, D. Ertaş, G. Grest, T. Halsey, D. Levine, and S. Plimpton, “Granular flow down an inclined plane: Bagnold scaling and rheology,” *Physical Review E*, vol. 64, no. 5, Oct. 2001.
- [98] K. L. Johnson, K. Kendall, and A. D. Roberts, “Surface Energy and the Contact of Elastic Solids,” *Proceedings of the Royal Society A: Mathematical, Physical and Engineering Sciences*, vol. 324, no. 1558, pp. 301–313, Sep. 1971.
- [99] W. Smith and H. Peng, “Modeling of Transient Wheel-Soil Interaction Using the Discrete Element Method,” presented at the 12th European Regional Conference of the International Society for Terrain-Vehicle Systems, South Africa, 2012.
- [100] K. Iwashita and M. Oda, “Rolling Resistance at Contacts in Simulation of Shear Band Development by DEM,” *Journal of Engineering Mechanics*, vol. 124, no. 3, pp. 285–292, 1998.
- [101] J. Ai, J.-F. Chen, J. M. Rotter, and J. Y. Ooi, “Assessment of rolling resistance models in discrete element simulations,” *Powder Technology*, vol. 206, no. 3, pp. 269–282, Jan. 2011.
- [102] H. P. Zhu, Z. Y. Zhou, R. Y. Yang, and A. B. Yu, “Discrete particle simulation of particulate systems: A review of major applications and findings,” *Chemical Engineering Science*, vol. 63, no. 23, pp. 5728–5770, Dec. 2008.
- [103] R. Sullivan, R. Anderson, J. Biesiadecki, T. Bond, and H. Stewart, “Cohesions, friction angles, and other physical properties of Martian regolith from Mars Exploration Rover wheel trenches and wheel scuffs,” *Journal of Geophysical Research*, vol. 116, no. E2, Feb. 2011.
- [104] V. Gromov, “Physical and Mechanical Properties of Lunar and Planetary Soils,” *Earth, Moon, and Planets*, vol. 80, no. 1, pp. 51–72, Dec. 1998.

- [105] M. Sutoh, K. Nagaoka, K. Nagatani, and K. Yoshida, “Design of wheels with grousers for planetary rovers traveling over loose soil,” *Journal of Terramechanics*, Jul. 2013.
- [106] W. Smith, D. Melanz, C. Senatore, K. Iagnemma, and H. Peng, “Comparison of DEM and Traditional Modeling Methods for Simulating Steady-State Wheel-Terrain Interaction for Small Vehicles,” presented at the 7th Americas Regional Conference of the ISTVS, Tampa, Florida, 2013.
- [107] M. Anitescu and A. Tasora, “An iterative approach for cone complementarity problems for nonsmooth dynamics,” *Computational Optimization and Applications*, vol. 47, no. 2, pp. 207–235, Oct. 2010.
- [108] C. Salot, P. Gotteland, and P. Villard, “Influence of relative density on granular materials behavior: DEM simulations of triaxial tests,” *Granular Matter*, vol. 11, no. 4, pp. 221–236, Apr. 2009.
- [109] T. Matsushima, J. Katagiri, K. Uesugi, A. Tsuchiyama, and T. Nakano, “3D Shape Characterization and Image-Based DEM Simulation of the Lunar Soil Simulant FJS-1,” *Journal of Aerospace Engineering*, vol. 22, no. 1, p. 15, 2009.
- [110] J.-P. Plassiard, N. Belheine, and F.-V. Donzé, “A spherical discrete element model: calibration procedure and incremental response,” *Granular Matter*, vol. 11, no. 5, pp. 293–306, Mar. 2009.
- [111] C. M. Wensrich and A. Katterfeld, “Rolling friction as a technique for modelling particle shape in DEM,” *Powder Technology*, vol. 217, pp. 409–417, Feb. 2012.
- [112] B. Yeomans, C. M. Saaj, and M. Van Winnendael, “Walking planetary rovers – Experimental analysis and modelling of leg thrust in loose granular soils,” *Journal of Terramechanics*, vol. 50, no. 2, pp. 107–120, Apr. 2013.
- [113] G. H. Peters, W. Abbey, G. H. Bearman, G. S. Mungas, J. A. Smith, R. C. Anderson, S. Douglas, and L. W. Beegle, “Mojave Mars simulant—Characterization of a new geologic Mars analog,” *Icarus*, vol. 197, no. 2, pp. 470–479, Oct. 2008.
- [114] M. Apfelbeck, S. Kuß, B. Rebele, and B. Schäfer, “A systematic approach to reliably characterize soils based on Bevameter testing,” *Journal of Terramechanics*, vol. 48, pp. 360–371, Oct. 2011.
- [115] I. Shmulevich, “State of the art modeling of soil–tillage interaction using discrete element method,” *Soil and Tillage Research*, vol. 111, no. 1, pp. 41–53, Dec. 2010.
- [116] V. Vedachalam, “Discrete Element Modelling of Granular Snow Particles Using LIGGGHTS,” M.Sc., University of Edinburgh, 2011.

- [117] Z. Asaf, D. Rubinstein, and I. Shmulevich, “Determination of discrete element model parameters required for soil tillage,” *Soil and Tillage Research*, vol. 92, no. 1–2, pp. 227–242, Jan. 2007.
- [118] Y. C. Chung and J. Y. Ooi, “Influence of Discrete Element Model Parameters on Bulk Behavior of a Granular Solid under Confined Compression,” *Particulate Science and Technology*, vol. 26, no. 1, pp. 83–96, Dec. 2007.
- [119] R. Briand, P. Radziszewski, and D. Pasini, “Virtual soil calibration for wheel–soil interaction simulations using the discrete-element method,” *Canadian Aeronautics and Space Journal*, vol. 57, no. 1, pp. 59–64, Apr. 2011.
- [120] Y. Fu, “Experimental Quantification and DEM Simulation of Micro-Macro Behaviors of Granular Materials Using X-Ray Tomography Imaging,” Doctor of Philosophy, Department of Civil and Environmental Engineering, Louisiana State University and Agricultural and Mechanical College, 2005.
- [121] J. Liu, B. Yun, and C. Zhao, “Identification and Validation of Rolling Friction Models by Dynamic Simulation of Sandpile Formation,” *International Journal of Geomechanics*, vol. 12, no. 4, pp. 484–493, Aug. 2012.
- [122] N. Belheine, J.-P. Plassiard, F.-V. Donzé, F. Darve, and A. Seridi, “Numerical simulation of drained triaxial test using 3D discrete element modeling,” *Computers and Geotechnics*, vol. 36, no. 1–2, pp. 320–331, Jan. 2009.
- [123] C. Senatore, M. Wulfmeier, I. Vlahinić, J. Andrade, and K. Iagnemma, “Design and implementation of a particle image velocimetry method for analysis of running gear–soil interaction,” *Journal of Terramechanics*, vol. 50, no. 5–6, pp. 311–326, Oct. 2013.
- [124] C. Senatore and K. Iagnemma, “Direct shear behaviour of dry, granular soils for low normal stress with application to lightweight robotic vehicle modelling,” in *Proceedings of the 17th ISTVS International Conference*, Blacksburg, Virginia, 2011.
- [125] C. Senatore, M. Wulfmeier, J. MacLennan, P. Jayakumar, and K. Iagnemma, “Investigation of stress and failure in granular soils for lightweight robotic vehicle applications,” in *Modeling & Simulation, Testing and Validation (MSTV) Mini-Symposium*, Michigan, 2012.
- [126] J. Brugada, Y. P. Cheng, K. Soga, and J. C. Santamarina, “Discrete element modelling of geomechanical behaviour of methane hydrate soils with pore-filling hydrate distribution,” *Granular Matter*, vol. 12, no. 5, pp. 517–525, Oct. 2010.
- [127] L. Hedjazi, C. L. Martin, S. Guessasma, G. Della Valle, and R. Dendievel, “Application of the Discrete Element Method to crack propagation and crack branching in a vitreous dense biopolymer material,” *International Journal of Solids and Structures*, vol. 49, no. 13, pp. 1893–1899, Jun. 2012.

- [128] J. Rojek, E. Oñate, C. Labra, and H. Kargl, “Discrete element simulation of rock cutting,” *International Journal of Rock Mechanics and Mining Sciences*, vol. 48, no. 6, pp. 996–1010, Sep. 2011.
- [129] F. Donze, V. Richefeu, and S.-A. Magnier, “Advances in discrete element method applied to soil, rock and concrete mechanics,” *Electronic Journal of Geotechnical Engineering (EJGE)*, vol. 8, pp. 1–44, 2009.
- [130] J.-F. Jerier, B. Hathong, V. Richefeu, B. Chareyre, D. Imbault, F.-V. Donze, and P. Doremus, “Study of cold powder compaction by using the discrete element method,” *Powder Technology*, vol. 208, no. 2, pp. 537–541, Mar. 2011.
- [131] S. Koziel and L. Leifsson, *Surrogate-based modeling and optimization applications in engineering*. New York, NY: Springer, 2013.
- [132] M. Mazzucco, “A reduced-order matrices fitting scheme with Log-Euclidean metrics for fast approximation of dynamic response of parametric structural systems,” *Computer Methods in Applied Mechanics and Engineering*, vol. 269, pp. 1–19, Feb. 2014.
- [133] R. Bornatico, J. Hüssy, A. Witzig, and L. Guzzella, “Surrogate modeling for the fast optimization of energy systems,” *Energy*, vol. 57, pp. 653–662, Aug. 2013.
- [134] A. Ashok, I. H. Lee, S. Arunachalam, I. A. Waitz, S. H. L. Yim, and S. R. H. Barrett, “Development of a response surface model of aviation’s air quality impacts in the United States,” *Atmospheric Environment*, vol. 77, pp. 445–452, Oct. 2013.
- [135] W. Du, A. Gupta, X. Zhang, A. M. Sastry, and W. Shyy, “Effect of cycling rate, particle size and transport properties on lithium-ion cathode performance,” *International Journal of Heat and Mass Transfer*, vol. 53, no. 17–18, pp. 3552–3561, Aug. 2010.
- [136] Y.-L. Zeng, C. I. Tan, W.-K. Tai, M.-T. Yang, C.-C. Chiang, and C.-C. Chang, “A momentum-based deformation system for granular material,” *Computer Animation and Virtual Worlds*, vol. 18, no. 4–5, pp. 289–300, Sep. 2007.
- [137] R. W. Sumner, J. F. O’Brien, and J. K. Hodgins, “Animating Sand, Mud, and Snow,” *Computer Graphics Forum*, vol. 18, no. 1, pp. 17–26, Mar. 1999.
- [138] K. Onoue and T. Nishita, “An Interactive Deformation System for Granular Material,” *Computer Graphics Forum*, vol. 24, no. 1, pp. 51–60, Mar. 2005.
- [139] C. Li, T. Zhang, and D. I. Goldman, “A Terradynamics of Legged Locomotion on Granular Media,” *Science*, vol. 339, no. 6126, pp. 1408–1412, Mar. 2013.
- [140] A. Azimi, J. Kovacs, and J. Angeles, “Wheel-soil interaction model for rover simulation based on plasticity theory,” 2011, pp. 280–285.

- [141] A. Azimi, J. Kovecses, and J. Angeles, “Wheel-Soil Interaction Model for Rover Simulation and Analysis Using Elastoplasticity Theory,” *IEEE Transactions on Robotics*, vol. 29, no. 5, pp. 1271–1288, Oct. 2013.
- [142] F. Boukouvala, Y. Gao, F. Muzzio, and M. G. Ierapetritou, “Reduced-order discrete element method modeling,” *Chemical Engineering Science*, vol. 95, pp. 12–26, May 2013.